1993

Computed Tomography Scanner For Dynamic Vascular Imaging In Vitro

Maria Drangova

COMPUTED TOMOGRAPHY SCANNER FOR DYNAMIC VASCULAR IMAGING *IN VITRO*

by

Maria Drangova
Department of Medical Biophysics

Submitted in partial fulfilment
of the requirements for the degree of
Doctor of Philosophy

Faculty of Graduate Studies
The University of Western Ontario
London, Ontario
July, 1993

ISBN 0-315-83995-3

Canada

ABSTRACT

A dynamic computed-tomography (CT) scanner has been developed for imaging objects undergoing periodic motion. The scanner has high spatial resolution and sufficiently high temporal resolution to produce quantitative tomographic images of objects, such as excised arterial samples perfused under physiological pressure conditions.

The dynamic CT scanner is comprised of a modified x-ray image intensifier (XRII) coupled to a 1024-element linear photo-diode-array detector. The XRII was modified to allow continuous electro-optical magnification of the field-of-view, thereby increasing the system's limiting resolution. High-resolution gated projection radiographs of a single slice are acquired at the rate of 60 Hz, as the object undergoes periodic motion. If the moving object is rotated through 180°, and projections are obtained at many view angles, tomographic images at different phases of the object's motion cycle can be reconstructed. Performance evaluation of the scanner showed that tomographic images can be obtained with resolution as high as 3.2 mm^{-1}, with only a 9% decrease in the resolution limit for objects moving at 1 cm s^{-1}. Quantitative measurements of attenuation coefficient are obtained with an accuracy of ± 0.02 cm^{-1}, and the accuracy in geometrical measurements of perimeter is ± 0.3 mm.

To evaluate the application of the system for imaging of intact excised vascular specimens under simulated physiological conditions, a computer-controlled flow simulator was built and used in the measurement of dynamic arterial distensibility. The flow simulator can reproduce physiological flow waveforms (including waveforms with reverse components) with a precision of ± 0.1 ml s^{-1}.

Existing techniques for the measurement of the static and dynamic elastic properties of excised vessels were adapted to take advantage of the additional data from the CT images and were used to demonstrate the utility of the CT scanner for applications in vascular research. Using these techniques, the local static and dynamic circumferential modulus of elasticity can be measured in intact arterial samples. Since the imaging technique is non-destructive, the mechanical properties of these vessels can be correlated directly with the composition of the vascular wall. This new system, together with the described techniques, offers a unique opportunity for studying dynamic events *in vitro*.

ACKNOWLEDGEMENTS

Many individuals have supported and assisted me during my tenure as a Ph.D. candidate and I am grateful to all. I would like to express sincere gratitude toward my supervisor Dr. Aaron Fenster for his guidance and encouragement throughout my years as a graduate student.

Special thanks are also extended to Dr. David Holdsworth whose help throughout my research has been invaluable. Without his reassurance and enthusiasm this work may not have been completed. I also thank Brian K. Reid, who would not let me quit graduate school many years ago. His confidence in my abilities inspired me to persevere and finish this research.

Furthermore, I am grateful to my parents for their patience and encouragement throughout the many years I spent in school.

I would also like to acknowledge my colleagues for their continual scientific collaboration and advice. I express many thanks to P.A. Picot (who knows everything), D.W. Rickey, R. Frayne, M.R. Roach, I.A. Cunningham, S. Napel, B.K. Rutt, L. Lauzon, and K. Chu for helpful discussions. Excellent technical assistance was provided by D.J.M. Miller, P.J. Dunmore, C. Boyd, J. Larsen, W. Dabrowski and K. Schulenburg. I am thankful to A. Ganguli, J. Verhagen and J.R. Mitchell for computer-related assistance.

Financial assistance for this research was provided by the Medical Research Council of Canada and partial personal support was granted by the Ontario Graduate Scholarship Program. I thank both agencies for their financial help.

TABLE OF CONTENTS

LIST OF FIGURES

1. INTRODUCTION

1.1 Computed Tomography Imaging

Since the discovery of x rays in the late 1800's, the projection radiograph has been one of the most commonly used clinical diagnostic tools. Projection radiography refers to the use of x rays to produce a radiographic "shadow" of a patient and recording it with an x-ray sensitive detector. Although projection radiography is an invaluable diagnostic tool, it suffers from two significant limitations: (1) limited soft-tissue contrast, and (2) superposition of overlying structures. Contrast between tissues with small density differences is limited, since the intensities in a projection image are proportional to the radiographic attenuation through the entire patient, rather than within a localized region. Overlap of complex structures within the body (including air cavities and bone) compounds the difficulties of diagnosis from a two-dimensional projection.

These limitations were alleviated with the introduction of computed tomography (CT) in 1973.[1,2] CT enabled radiologists to obtain cross-sectional images of patients, in which the signal level is proportional to the mean attenuation coefficient of the imaged tissue. Since its inception, computed tomography has been used extensively in the clinic as a diagnostic tool, particularly in areas where differentiation between soft tissues is required. Although the basic principles employed in the reconstruction of transverse images from projections have not changed over the past decade, improved detector design and technology has led to improvements in image resolution, and reduced scanning times. Furthermore, although the primary application of CT scanners is in imaging stationary regions of the body, such as the brain and abdomen, specialized scanners have been built to image moving organs, such as the beating heart.[3,4,5] Notable examples are: the "dynamic spatial reconstructor,"[3,6] which is based on 28 detectors and x-ray tubes used for the

simultaneous acquisition of projection data; and the high-speed CT scanner developed by Boyd et al.,[4,7] which rapidly sweeps an electron beam over a ring-shaped target to irradiate a slice in 50 ms.

1.2 Image Quality and CT Imaging

Computed-tomographic images are "maps" of mean linear attenuation coefficient within a section of the imaged object. As in all images, the ability to visualize structures in an image depends on: (1) the contrast of the structure with respect to its surroundings, (2) the noise level in the image, and (3) the resolving capabilities of the scanner relative to the size of the structures of interest. The contrast between two objects is dependent on the difference in attenuation coefficient. Since soft tissues have similar attenuation coefficients (varying by less than 1 %), relatively low contrast exists between many different structures in the body. Therefore, the noise level in the images must be low in order to discern subtle changes in attenuation coefficient. Image noise sources include quantum noise (due to the statistical nature of the detection of x-ray photons) and detector noise. In clinical applications of CT, quantum noise is the dominant noise source, due to dose-related limitations in x-ray fluence. Previous investigations[8,9] have shown the following relationship between ionizing-radiation dose, resolution, and image noise:

$$D \propto \frac{1}{h w^3 \sigma_\mu^2},$$

where D is the radiation dose, h is the slice thickness, w is the effective pixel dimension, and σ_μ is the image noise (represented by the standard deviation of the attenuation coefficient within a pixel). Thus, the dose delivered to the patient is inversely proportional to the square of the image noise and inversely proportional to the fourth power of the effective pixel size (assuming a fixed ratio between the slice

thickness and the pixel dimension). For example, if the pixel dimension must be reduced by a factor of two (*i.e.*, the volume of the pixel is reduced by a factor of eight), the delivered dose must increase by a factor of 16 to maintain a fixed σ_μ. Conversely, if the dose is kept constant, the noise would be four times greater in the high-resolution image. This increase in noise would reduce the contrast-to-noise ratio (and hence detectibility) by a factor of four. This fundamental relationship explains the unavoidable compromise between noise reduction and resolution in clinical CT imaging.

1.3 Application of CT in Basic Research

Many research applications would benefit from computed tomography. Unlike clinical imaging, most research applications have no dose constraints and no compromise between noise reduction and high resolution is necessary. Since a higher fluence can be used, CT scanners applied in basic research can provide lower-noise images using high-resolution detectors (provided that detector noise is small). Higher resolution is of particular importance for imaging small animals and pathological samples. Furthermore, for many research applications image contrast can be controlled. High contrast can be achieved by using radio-opaque dyes, such as those commonly used in angiography, and by controlling the spectrum of the incident x-ray beam. Since longer imaging times are possible, more filtration can be added to a polyenergetic x-ray beam in order to select the optimum spectrum for a specific application.

A major benefit of the application of clinical CT techniques in basic research is the acquisition of quantitative information about an object's composition and geometry. However, the major limitation of clinical CT scanners is their relatively low spatial resolution and large image slice thickness (typically 1 cm). Newer CT scanners with improved resolution, and the capability for volume acquisition by helical

scanning, are available, but the obtainable slice thickness (2 mm) still limits resolution in the axial direction.[10] Furthermore, clinical scanners are not commonly available for *in vitro* studies, due to high patient loads. Recently, a number of groups have developed specialized laboratory CT scanners for *in vitro* imaging of pathological specimens and small-animal imaging.[11,12,13,14] Dedicated CT scanners, such as these, can be designed to provide the best images in specific research applications, and are routinely available for *in vitro* studies.

1.4 Atherosclerosis Research and Quantitative CT

Basic research focusing on vascular diseases is one area of investigation that would benefit from the availability of dedicated high-resolution CT scanners. The information provided by these scanners could be used in the study of the geometry, composition and mechanical properties of atherosclerotic human vessels.

1.4.1 Manifestations of atherosclerosis

Atherosclerosis, a disease of the vasculature, is the primary cause of heart attacks and strokes.[15] Atherosclerosis is characterized by: (1) an increase in stiffness of the vascular wall; (2) changes in the composition of the wall (elastin reduction, calcification, fibrosis);[16] (3) enlargement of some vessels, such as the aorta; (4) stenosis of other vessels, such as the carotid, coronary and iliac arteries, due to fibrous plaques which develop on the intimal surface; and (5) an increase in blood pressure, possibly due to decreased baroreceptor sensitivity.[17] The patchy nature of the distribution of atherosclerotic lesions suggests that local factors must play an important role in disease development.[18] These local factors include haemodynamic effects (such as shear rate), and mechanical stresses due to the distribution of forces within the arterial wall.

Since atherosclerosis is responsible for a large fraction of the mortality in the western world[15] it has been the subject of many investigations in the past. These

investigations have focused on the understanding of mechanical and haemodynamic factors involved in the initiation and progression of the disease,[19,20] as well as the involvement of different cell types and molecules in atherogenesis.[15] Although the transition between early "fatty streaks" to more advanced atherosclerotic lesions is well documented,[15,21] the role of mechanical factors is still not completely resolved. Since the rate of exchange of macromolecules between the lumen and the arterial wall depends on both haemodynamic factors (such as shear rate) and mechanical factors (such as circumferential stretch),[22] analyzing the mechanical properties of excised human or animal vessels and correlating these to disease sites is essential in understanding the processes involved in the initiation of atherosclerosis. Furthermore, the mechanical properties of the arterial wall play an important role in the relationship between arterial pressure and flow. Alterations in the mechanical properties, associated with aging and disease progression, would thus correspond to changes in haemodynamic parameters such as pulse-wave velocity.[23,24] Techniques to infer the elastic properties from *in vivo* measurements of pulse-wave velocity are being developed[25,26] for diagnostic purposes, and would benefit from a thorough understanding of the relationship between mechanical properties and disease state, measured *in vitro*.

1.4.2 Measurement of vascular-wall composition and mechanical properties

The arterial wall exhibits viscoelastic behaviour and, thus, both static and dynamic mechanical properties of excised vessels must be studied. *In vitro* studies of the mechanical properties have been performed using intact specimens or strips of arteries which have been stressed under controlled conditions. Studies of the circumferential elastic properties, which have been performed using intact specimens,[27,28,29,30,31] typically involve the measurement of the external diameter, or changes in luminal volume, while monitoring the transmural pressure.

Unfortunately, none of these investigators has had the capability to measure the arterial wall thickness directly and consequently have inferred the wall thickness from measurements of wall volume and specimen length (assuming that the wall is incompressible). Although this approach is valid, one cannot account for local variations in wall thickness using this technique. In previous studies performed on strips[32,33,23] wall thickness was determined from measurements at only one strain, or from the volume of the wall.

Recently, a number of *in vivo* techniques have also been developed to characterise arterial compliance using ultrasound or magnetic resonance imaging. The ultrasound techniques[34,35,36] use "echo-tracking" devices to monitor wall movement of the peripheral arteries and photo plethysmographs to measure the pressure. Although, with these techniques, changes in diameter can be measured with high precision (2-10 μm), the accuracy of the diameter measurements is only about 0.5 mm. The measurements are also susceptible to transducer-positioning errors, and the wall thickness cannot be measured. These techniques are important since they are non-invasive, but are limited by the fact that they can be used only on peripheral vessels. An *in vitro* ultrasound technique for measuring the elasticity of arteries, currently being developed at the University of Toronto, uses a high-resolution intravascular probe to image the arterial wall while the vessel is distended.[37]

Techniques for measuring arterial elasticity using magnetic resonance (MR) imaging are also being developed.[38,39] Behling *et al.*[38] obtained MR images of rat carotid arteries *in vivo* and correlated the changes of lumen area to the changes in measured pressure, but had to use *ex vivo* measurements of the wall thickness to calculate the circumferential modulus of elasticity. Chu *et al.*,[40] in our laboratory, are developing a promising *in vitro* MR technique which can be used to measure the viscoelastic properties of excised arteries. This technique provides measurements

of the circumference and wall thickness, and since they apply "tags" to the arterial wall, they may also detect differences in distensibility associated with diseased areas of the wall. This technique can potentially be applied *in vivo* in the future.

To the best of my knowledge there are no *in vitro* techniques, other than the ones currently being developed by Chu[40] and Ryan,[37] which allow nondestructive measurement of the local circumferential elastic properties of excised arteries. In addition, even these techniques would not provide adequate identification of the location of calcified plaques within the wall (the ultrasound technique would actually fail if calcified plaques are present). Thus, only a high-resolution x-ray technique would be able to evaluate the local mechanical properties of excised arteries with lesions at all stages of atherosclerosis. Coupling such measurements to histological analysis of the composition at the same locations of the vessel wall could provide new insight into the processes involved in vascular diseases.

1.5 Research Goal

The goal of my research was to develop a laboratory dynamic CT scanner with high spatial resolution and sufficiently high temporal resolution to be able to produce high-quality tomographic images of objects undergoing periodic motion. Such a scanner must be able to provide quantitative information about the composition and geometry of the object and must be effective for the measurement of the mechanical properties of excised arterial specimens. Furthermore, for the study of the dynamic elastic properties of arteries, the scanner must be able to image intact excised arterial specimens under simulated physiological pressure conditions. Thus, a technique to simulate highly-reproducible physiological flow and pressure waveforms is required, along with a technique for the analysis of dynamic arterial distensibility from the CT images.

To fulfil the objectives outlined above, I have developed a dynamic CT scanner based on a modified x-ray image intensifier (XRII) coupled to a linear photodiode array (PDA) detector. The XRII was modified to allow continuous zooming of the image by electro-optical means, thereby increasing the resolution. A complete characterization of the scanner, including spatial resolution, temporal response, accuracy and precision, is essential before the system can be used as a research tool. To evaluate the application of the system to imaging intact excised vascular specimens under simulated physiological conditions, a computer-controlled flow simulator was built and used in the measurement of dynamic arterial distensibility. Existing techniques for the measurement of the static and dynamic elastic properties of vessels have also been adapted to take advantage of the additional data from the CT images, thus demonstrating the utility of the CT scanner for applications in vascular research.

1.6 Thesis Outline

1.6.1 Modified x-ray image intensifier

The first step in developing a high-resolution CT scanner is to find an x-ray detector with appropriate resolution. Chapter two describes the modification made to a conventional x-ray image intensifier to enable the field-of-view (FOV) to be varied continuously, by adjusting the potentials at the focusing electrodes. The improvement in system resolution, achieved by decreasing the FOV, is characterised by measuring the modulation transfer function of the XRII, coupled to a high-resolution PDA, at a number of different FOV's. For comparison, the resolution is also characterized at the same FOV's, but using optical zooming to achieve the desired magnification. I show that electronic zooming always yields a greater gain in resolution than optical zooming. (Note however, that this gain may not be significant if the optical detector coupled to the XRII and the XRII contribute equally to resolution degradation.)

Chapter two is the basis of a paper entitled "A modified x-ray image intensifier with continuously variable field of view: resolution considerations" by Drangova, Holdsworth, Picot, Schulenburg, and Fenster, which has been accepted for publication to Medical Physics. The modification to the XRII was implemented by K. Schulenburg. P.A. Picot and D.W. Holdsworth were involved in the design of the modification and assisted with some of the characterization experiments.

1.6.2 High-resolution laboratory CT scanner for dynamic imaging

Chapter three is a description and characterization of the high-resolution laboratory CT scanner that I developed for imaging objects undergoing periodic motion. The scanner is comprised of the modified x-ray image intensifier, optically coupled to a linear photo-diode array. With this scanner, gated projections of a single slice of the moving object are acquired from different views. These data are then reformatted and reconstructed into a series of CT images which show the object at different phases of its motion cycle.

The scanner has an adjustable range of fields-of-view (*FOV*) and the resolution can be as high as 3.2 mm^{-1}. In chapter three, I show theoretically and demonstrate experimentally that the temporal response depends on the inherent resolution of the scanner and the object's velocity. For objects moving at 1 cm s^{-1} the resolution is reduced by 15% in the direction of motion. I also show that the scanner's response is linear for materials with attenuation coefficients as high as 1.5 cm^{-1}, with an average accuracy of ± 0.02 cm^{-1}. The average accuracy of circumference measurements made from the CT images is shown to be ± 0.3 mm.

Chapter three constitutes the body of a paper entitled "A laboratory CT scanner for dynamic imaging" by Drangova and Fenster, which has been submitted for publication in Medical Physics.

1.6.3 Measuring the static elastic properties of vascular specimens

In chapter four I describe a technique developed for non-destructive investigation of the static elastic properties of intact vascular specimens. Although the ultimate goal was to develop a method for measuring the dynamic elastic properties of excised vessels, it is essential to first verify the feasibility of using a high-resolution CT scanner for static measurements, without adding the additional complication of motion. For the static studies described in this chapter we used a high-resolution volume CT scanner, similar to the one described in chapter three but optimized for static, multi-slice imaging. With this scanner the complete vascular geometry of the vessel can be characterized, as well as the static elastic properties of selected slices. Images were obtained through an intact abdominal aortic aneurysm at five pressures. The incremental circumferential Young's modulus was calculated from the internal and external circumferences, and at physiological pressures the aneurysm was found to be 275 times stiffer than the normal aorta proximal to it. Subsequent histological analysis of the image sections revealed a sixfold decrease in elastin content in the aneurysm, compared to the normal aorta.

Chapter four forms the basis of a paper entitled "Elasticity and geometry measurements of vascular specimens using a high-resolution laboratory CT scanner" by Drangova, Holdsworth, Boyd, Dunmore, Roach, and Fenster, which has been published in Physiological Measurement (14, 1993). D.W. Holdsworth was involved in the data acquisition and reconstruction. C.J. Boyd assisted with the data acquisition and the analysis of the errors in the elastic modulus. P.J. Dunmore and Dr. M.R. Roach assisted with the sample preparation and histological studies.

1.6.4 Pump for physiological flow simulation

In chapter five I describe a computer-controlled flow simulator, designed to mimic physiological flow waveforms. This device has made the measurement of

dynamic elasticity in excised vascular specimens possible. The pump is a positive-displacement device, which incorporates two rack-mounted pistons, driven into opposing cylinders by a micro-stepping motor. The dual-cylinder approach allows nearly uninterrupted steady flow, as well as various pulsatile waveforms to be produced. Waveforms with reverse flow components are also possible. The accuracy and precision of the pump were measured and are presented. Of particular importance to the study of dynamic elasticity, with the CT scanner described in chapter three, is the cycle-to-cycle reproducibility. The results from a study of this reproducibility show an average variation of 0.1 ml s^{-1} over thousands of cycles.

The material presented in chapter five is a portion of a paper entitled "Computer-controlled positive displacement pump for physiological flow simulation" by Holdsworth, Rickey, Drangova, Miller, and Fenster, which has been published in Medical and Biological Engineering and Computing (**29**, 565-570, 1991). D.W. Holdsworth invented the pump. D.W. Rickey wrote the software which controls the pump. Assistance in building the device was supplied by D.J.M. Miller. I was involved in the design of the device and the characterisation of its performance.

1.6.5 Measuring the dynamic elastic properties of vascular samples

Chapter six describes a technique for measuring the dynamic elastic properties of excised vascular specimens *in vitro*, using the dynamic CT scanner described in chapter three and the physiological flow simulator described in chapter five. This novel technique allows us to measure the dynamic modulus of elasticity not only as a function of frequency, but also as a function of radial position around the vessel. The distinction between different segments around the vessel is achieved by inserting highly-attenuating thin copper wires within the adventitial surface of the artery. CT images of a single slice through the artery are acquired at different phases of the cardiac cycle, while the pressure in the artery is monitored. The

dynamic modulus of elasticity is obtained as a function of frequency from the recorded pressure waveform and the measured circumference and segment-length waveforms. A porcine abdominal aorta was used to demonstrate the technique. This technique can be combined with that described in chapter four to provide a complete characterization of the three-dimensional geometry of a vessel and the static and dynamic elastic properties of selected sections. Since both imaging techniques are non-destructive, the mechanical properties can be correlated directly to the histological measurements of the composition of the arterial wall.

The material presented in this chapter forms a portion of a manuscript, entitled "Technique for measuring the local dynamic elastic properties of arteries with a high-resolution high-speed CT scanner." This manuscript is being prepared for submission to the Journal of Biomechanics.

1.6.6 Summary and future applications

Chapter seven summarizes the work described in this thesis and presents some future applications of the dynamic CT scanner. In particular, the application of the device for measuring velocity and shear rate in excised vascular specimens is discussed. The principles described in chapter three, for the acquisition of dynamic images undergoing periodic motion, can also be applied to clinical imaging. This application is discussed in chapter seven as well.

REFERENCES

1. A.M. Cormack, "Representation of a function by line integrals, with some radiological applications," J. Appl. Phys. **34**, 2722-2727 (1963).

2. G.N. Houndsfield, "Computerized transverse axial scanning (tomography): Part 1: Description of system," Br. J. Radiol. **46**, 1016-22 (1973).

3. R.A. Robb, J.F. Greenleaf, E.L. Ritman, S.A. Johnson, J.D. Sjostrand, G.T. Herman and E.H. Wood, "Three-dimensional visualization of the intact thorax and contents: A technique for cross-sectional reconstruction from multiplanar x-ray views," Comp. Biomed. Res. **7**, 395-419 (1974).

4. D.P. Boyd, R.G. Gould, J.R. Quinn, R. Sparka, J.H. Stanley, and W.B. Herrmannsfeldt, "A proposed dynamic cardiac 3-D densitometer for early detection and evaluation of heart disease," IEEE Trans. Nuc. Sci. **NS-26**, 2724-2727 (1979).

5. B. Lantz, B. Lindberg, and J. Huebel, "Three-dimensional video reconstruction in fluoroscopy by means of a television system with high temporal resolution," in *Reconstruction Tomography in Diagnostic Radiology and Nuclear Medicine*, M.M. Ter-pogossian *et al.* eds., (University Park Press, Baltimore, 1977, pp. 483-499).

6. E.H. Wood, J.H. Kinsey, R.A. Robb, B.K. Gilbert, L.D. Harris, and E.L. Ritman, "Applications of high temporal resolution computerized tomography to physiology and nuclear medicine," in *Image Reconstruction from Projections*, G.T. Herman ed., (Springer-Verlag, New York, 1979, pp. 247-279).

7. K.R. Peschmann, S. Napel, J.L. Couch, R.E. Rand, R.A. Alei, S.M. Ackelsberg, R. Gould, and D.P. Boyd, "High-speed computed tomography: systems and performance," Appl. Optics **24**, 4053-4060 (1985).

8. R.A. Brooks and G. DiChiro, "Statistical limitations in x-ray reconstructive tomography," Med. Phys. **3**, 237-240 (1976).

9. H.H. Barrett, S.K. Gordon, and R.S. Hershiel, "Statistical limitations in transaxial tomography," Comput. Biol. Med. **6**, 307-323 (1976).

10. W.A. Kalender and A. Polacin, "Physical performance characteristics of spiral CT scanning," Med. Phys. **18**, 910-915 (1991).

11. J.M. Boone, G.M. Alexander, and J.A. Seibert, "Personal computer fluoroscopy CT system for small animal and specimen research," Radiology 177, 136 (1990).

12. F.H. Sequin, P. Burstein, P.J. Bjorkholm, F. Homburger, and R.A. Adams, "X-ray computed tomography with 50-μm resolution," Applied Optics **24**, 4117-4123 (1985).

13. L.E. Feldcamp, S.A. Goldstrein, A.M. Parfitt, G. Jesion, and M. Kleerkoper, "The direct examination of three-dimensional bone architecture *in vitro* by computed tomography," J. of Bone and Min. Res. **4**, 3-11 (1989).

14. E.J. Morton, S. Webb, J.E. Bateman, L.J. Clarke, and C.G. Shelton, "Three-dimensional x-ray mictrotomography for medical and biological applications," Phys. Med. Biol. **35**, 805-820 (1990).

15. R. Ross, "The pathogenesis of atherosclerosis: a perspective for the 1990's," Nature **362**, 801-809 (1993).

16. D.L. Newman, R.G. Gosling, and N.L.R. Bowden, "Changes in aortic distensibility and area ratio with the development of atherosclerosis," Atherosclerosis **14**, 231-240 (1971).

17. A.C. Simon, M.E. Safar, Y.A. Weiss, G.M. London, and P.L. Milliez, "Baroreflex sensitivity and cardiopulmonary blood volume in normotensive and hypertensive patients," Br. Heart. J. **39** 799-805 (1977).

18. C.G. Caro, M.J. Lever, K.H. Parker, and P.J. Fish, "Effect of cigarette smoking on the pattern of arterial blood flow: possible insight into mechanisms underlying the development of atherosclerosis," Lancet July 4, 11-13 (1987).

19. W.R. Milnor, *Hemodynamics*, Williams and Wilkins, Baltimore 1989.

20. D.H. Bergel, ed., *Cardiovascular fluid dynamics*, Academic Press, London 1972.

21. PDAY Research Group, "Relationship of atherosclerosis in young men to serum lipoprotein cholesterol concentrations and smoking," JAMA **264**, 3018-3024 (1990).

22. D.L. Fry, R.W. Mahley, and S.Y. Oh, "Effect of arterial stretch on transmural albumin and Evan's blue dye transport," Am. J. Physiol. **9**, H645-649 (1981).

23. F.C.P Yin, H.A. Spurgeon, and C.H. Kallman, "Age-associated alterations in viscoelastic properties of canine aortic strips," Circ. Res. **53**, 464-472 (1983).

24. D.J. Farrar, H.D. Green, W.D. Wanger, and M.G. Bond, "Reduction in pulse-wave velocity and improvement of aortic distensibility accompanying a regression of atherosclerosis in the Rhesus monkey," Circ. Res. **47**, 425-432 (1980).

25. E.D. Lehmann, R.G. Gosling, J.R. Parker, T. deSilva, and M.G. Taylor, "A blood pressure independent index of aortic distensibility," Br. J. Radiol. **66**, 126-131 (1993).

26. C.L. Dumoulin, D.J. Doorly, and C.G. Caro, "Quantitative measurement of velocity at multiple positions using excitation and fourier velocity encoding," Magn. Resn. Med. **29**, 44-52 (1993).

27. M.R. Roach and A.C. Burton, "The reason for the shape of the distensibility curves of arteries," Can. J. Biochem. Physiol. **35**, 681-690 (1957).

28. D.H. Bergel, "The static elastic properties of the arterial wall," J. Physiol. **156**, 445-457 (1961).

29. B.S. Gow, D. Schonfeld, and D.J. Patel, "The dynamic elastic properties of the left circumflex artery," Circ. Res. **18**, 278-291 (1974).

30. R.H. Cox, "Three-dimensional mechanics of arterial segments *in vitro*: methods," J. Appl. Physiol. **36**, 381-384 (1974).

31. A.M. Brant, S.S. Shah, V.G.J. Rogers, J. Hoffmeister, I.M. Herman, R.M. Kormos, and H. Borovetz, "Biomechanics of the arterial wall under simulated flow conditions," J. Biomechanics **21**, 107-113 (1988).

32. R.W. Lawton, "Measurements on the elasticity and damping of isolated aortic strips of the dog," Circ. Res. **3**, 403-408 (1955).

33. J. Cleave and M.R. Roach, "Comparison of longitudinal elastic properties of proximal and distal strips of aorta-branch junctions from the abdominal aorta of sheep," Can. J. Physiol. and Pharmacol. **61**, 614-618 (1983).

34. Y. Tardy, J.J. Meister, F. Perret, H.R. Brunner, and M. Arditi, "Non-invasive estimate of the mechanical properties of peripheral arteries from ultrasonic and photoplethismographic measurements," Clyn. Phys. Physiol. Meas. **12**, 39-54, (1991).

35. A.P.G. Hoeks, P.J. Brands, F.A.M. Smeets, and R.S. Reneman, "Assesment of the distensibility of superficial arteries," Ultrasound in Med. and Biol. **16**, 121-128 (1990).

36. T. Lanne, H. Stale, H. Bengtsson, D. Gustafsson, D. Bergqvist, B. Sonesson, H. Lecerof, and P. Dahl, "Noninvasive measurement of diameter changes in the distal abdominal aorta in man," Ultrasound in Med. and Biol. **18**, 451-457 (1992).

37. L.K. Ryan, G.R. Lockwood, B.G. Starkovski, D.W. Holdsworth, D. Rickey, A. Fenster, and F.S. Foster, "A high frequency intravascular ultrasound imaging system for investigaion of vessel wall properties," Proc. Can. Med. Biol. Eng. Soc. 190 (1992).[abs]

38. R.W. Behling, H.K. Tubbs, M.D. Cockman, and L.W. Jelinski, "Stroboscopic NMR microscopy of the carotid artery," Nature **341**, 321-323 (1989).

39. R.H. Mohiaddin, S.R. Underwood, H.G. Bogren, D.N. Firmin, R.H. Klipstein, R.S.O. Rees, and D.B. Longmore, "Regional aortic compliance studied by magnetic resonance imaging: the effects of age, training, and coronary artery disease," Br. Heart J. **62**, 90-96 (1989).

40. K.C. Chu and B.K. Rutt, "An *in vitro* method of measuring local arterial elasticity under pulsatile motion," Proc. Soc. Mag. Res. Med. 829 (1992).[abs.]

2. MODIFIED X-RAY IMAGE INTENSIFIER

2.1 INTRODUCTION

Recently, a number of techniques have been described, in which x-ray image intensifiers (XRII) have been utilised in vascular research,[1,2,3,4] small animal imaging,[2,4,5] and *in vitro* bone densitometry.[6] Although state-of-the-art XRII's may be used at a number of fixed fields-of-view, none have the capability of continuously varying the size of the input image that is mapped onto the output phosphor. Many research applications and applications in clinical fluoroscopy[7] would benefit from the ability to vary the magnification continuously, and to select any magnification within a given range in order to maximize the resolution for a given field-of-view (FOV). For the application of XRII's to the imaging of vascular specimens they must have sufficiently high resolution to enable accurate measurements of the arterial size.

Varying the magnification of an XRII may be accomplished by optical or electro-optical means. Although the desired magnification may be achieved by either technique, optimal improvement of the system spatial resolution may not always result. To achieve optimal resolution improvement, consideration must be given to the relative contribution of each magnification technique. In a recent paper, Rudin et al.[7] described the performance of a fluoroscopic system incorporating an optical zoom lens, in place of the fixed focal-length video-camera lens. The zoom lens was implemented in order to use optimally the bandwidth of the video cameras commonly used in clinical fluoroscopy units. They reported improvements in the system modulation transfer function (MTF), with increasing magnification factor, but showed negligible difference between optically and electronically achieved magnification. We believe, and show here, that greater improvements in resolution can be achieved by electro-optical zooming, especially in the cases where the XRII is the component which limits system resolution.

The principles of continuous electro-optical zooming of XRII have been described previously,[8,9] and Robbins et al.[10] reported on a prototype intensifier, which allowed zooming between a 22.3-cm and a 11.4-cm field-of-view. In this chapter, I describe an "add-on" modification to conventional multiple-field x-ray image intensifiers to provide continuous electro-optical zooming capabilities by simultaneously varying the voltages of the two focusing electrodes. I describe the modification in detail and provide measurements of the MTF for different FOV's. For comparison, I also present MTF measurements for the same magnifications achieved optically. I also include the results from two optical detectors - a high-resolution linear photo-diode array (PDA), which we use in non-fluoroscopic research applications (such as the CT scanner described in chapter three), and a video camera, which has poorer resolution than the PDA - and compare the MTF's achieved by optical and electronic zooming.

Chapter two is based on a paper, entitled "A modified x-ray image intensifier with continuously variable field-of-view: resolution considerations," which has been accepted for publication to Medical Physics. The modification was implemented by K. Schulenburg. P.A. Picot and D.W. Holdsworth were involved in the design of the modification and assisted with some of the characterization experiments. I designed and performed the experiments to characterize the improvements in resolution, and compared the benefits of electro-optical zooming to those of optical zooming. I also formulated the theoretical validation of the differences observed between optical and electronic zooming for the two types of optical detectors.

2.2 THEORY

The modulation transfer function of an XRII imaging system is given by the product of the MTF's of the XRII and the optical detector coupled to it. The MTF of the XRII, MTF_{XRII} (measured in the plane of the output phosphor), is due to the cascade of the transfer functions of the XRII components: the input phosphor, electron optics, and the output phosphor. The relative contribution of the output phosphor and electron-optics MTF's to MTF_{xrii} depends, in part, on the electronic magnification factor M_e, which is defined as the ratio of the size of the image at the XRII output phosphor to that at the input phosphor. Varying M_e is achieved by changing the electric potential on the electrostatic focusing elements within the XRII, which also may affect the quality of the electron optics. Previous studies[10] have shown that the electro-optical focusing improves the resolution for large values of M_e; *i.e.*, small fields-of-view.

The MTF of the optical-detector system coupled to the XRII, MTF_{det} (measured at the detector plane), is the product of two components: one due to the coupling lenses, and one due to the resolution of the optical detector itself. The optical magnification factor M_o, in analogy to M_e, is defined as the ratio of the size of the image in the optical-detector plane to that in the plane of the XRII output phosphor. The value of M_o may be varied by changing the relative focal lengths of the coupling lenses, often through the use of a conventional zoom lens in front of the detector. The amount of optical abberation caused by this coupling lens also may depend on the value of M_o, typically with increased blurring associated with large M_o. In a conventional fluoroscopic imaging system, the electronic magnification factor M_e is always less than unity, since the XRII demagnifies the image; and M_o is usually near unity, since the size of the optical detector is usually matched to the size of the XRII-output phosphor.

The MTF of a fluoroscopic system can be, thus, separated into components due to the XRII and components due to the optical detector and coupling lenses; *i.e.*,

$$MTF_{sys}(f, M_{tot}) = MTF_{xrii}(\frac{f}{M_e}, M_e) \cdot MTF_{det}(\frac{f}{M_e M_o}, M_o) \ , \qquad (2.1)$$

where f is the spatial frequency in the plane of the XRII input phosphor and $M_{tot} = M_e \cdot M_o$ is the ratio of the size of the image in the optical-detector plane to that in the plane of the XRII input phosphor. The dependencies of MTF_{xrii} and MTF_{det} on M_e and M_o, respectively, are imposed by the properties of the electron optics and coupling lens, as described above.

In practical implementations, a wide range of XRII's, coupling lenses, and optical detectors are available, making it difficult to predict the relative contributions of MTF_{xrii} and MTF_{det} to the total system MTF. This, in turn, makes it difficult to predict the relative effects of electronic and optical zooming on system MTF. However, we can consider three simplified cases which clarify the roles of electronic and optical zooming, with respect to their effect on the limiting resolution of the system:

Case 1: *Optical-detector dominated* MTF_{sys}, *i.e.*, $MTF_{xrii}(\frac{f}{M_e}) > MTF_{det}(\frac{f}{M_e M_o})$ at the limiting spatial frequency of the system. In this situation, improvements in MTF_{sys} can be achieved by varying either M_e or M_o, provided the desired M_{tot} is reached. There is no benefit in choosing one type of magnification over the other.

Case 2: *XRII dominated* MTF_{sys}, *i.e.*, $MTF_{det}(\frac{f}{M_e M_o}) > MTF_{xrii}(\frac{f}{M_e})$ at the limiting spatial frequency of the system. In this case, a given value of M_{tot} should be achieved with the largest value of M_e possible, since this will lead to a direct improvement in MTF_{xrii} and thus to a direct improvement of MTF_{sys}.

Case 3: *Equivalent XRII and detector MTF's, i.e.,* $MTF_{det}(\frac{f}{M_e M_o}) \approx MTF_{xrii}(\frac{f}{M_e})$ for all spatial frequencies of interest. In this case, a given value of M_{tot} should also be achieved with the largest value of M_e possible, since both MTF_{det} and MTF_{xrii} will be affected. However, the improvement in MTF_{sys} for electronic zooming over optical zooming may not be as significant as in case 2.

In this chapter, the last two of the cases described above are investigated, using both high- and low-resolution optical detectors to alter the dominance of the XRII and detector MTF components. In both cases, we have employed various combinations of electronic and optical zooming, in order to determine if the resolution advantages of electronic zooming predicted by this simplified model are realized.

2.3 Modification Description

We have modified a conventional Thompson-CSF 9" multiple-field x-ray image intensifier as illustrated in Fig. 2.1. A variable high-voltage power supply (Bertan Associates Inc., Hicksville, NY, USA, Model 602B 200P, 0-20kV) controls the voltage V_{G3} at electrode G_3, bypassing the direct connection (between points A and B in Fig. 2.1) to the voltage-divider resistor chain. Varying V_{G3} moves the electron crossover point, thus changing the image magnification.[9] The focus of the electron beam is adjusted by a motor-driven 50 MΩ potentiometer, which changes the potential V_{G2} at electrode G_2. The size of the FOV, referenced to the input phosphor, depends on V_{G3}, which we refer to as the "zoom voltage." The voltage V_{G2} must be adjusted appropriately to ensure a sharp image at the output phosphor of the XRII, and we refer to it as the "focus voltage." The output voltage of the power supply and the potentiometer's motor driver are controlled by a PC/AT computer. The potential at electrode G_1 was not altered.

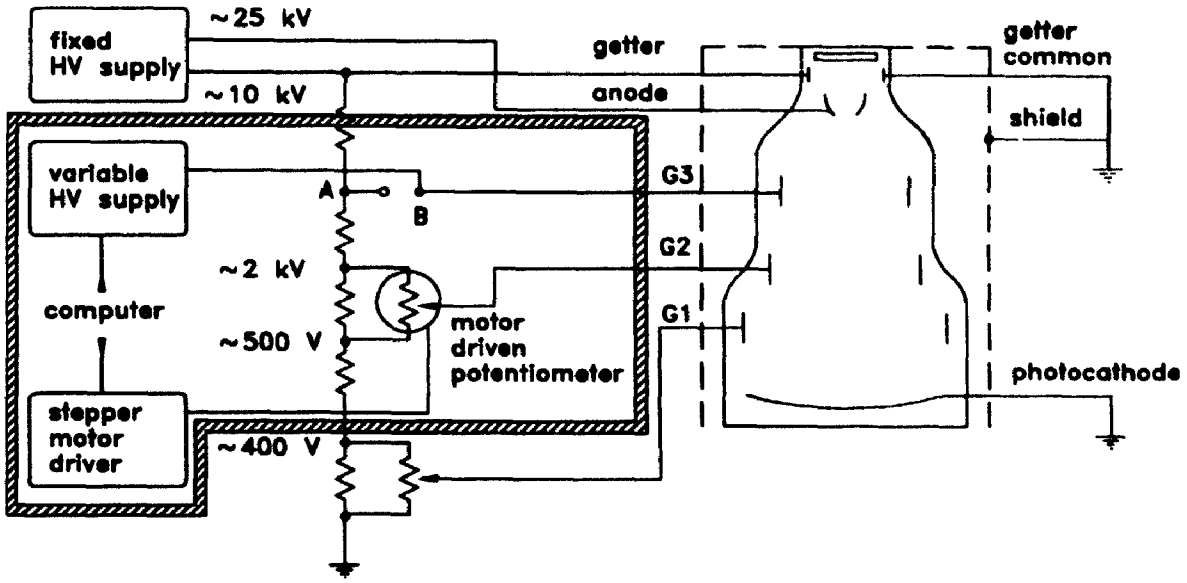

Figure 2.1: Schematic diagram showing the modification of the XRII (within the hatched box), which allows the FOV to be adjusted continuously under computer control.

2.4 Experimental Methods

Figure 2.2 schematically shows the apparatus used for the determination of the zoom and focus voltages and for the MTF measurements of the XRII-optical-detector system. Measurements were performed with two optical detectors: a high-resolution linear photodiode array (PDA) and a video camera. The PDA was a 1024-element Reticon device (EG&G Reticon RL1024S, Sunnyvale,

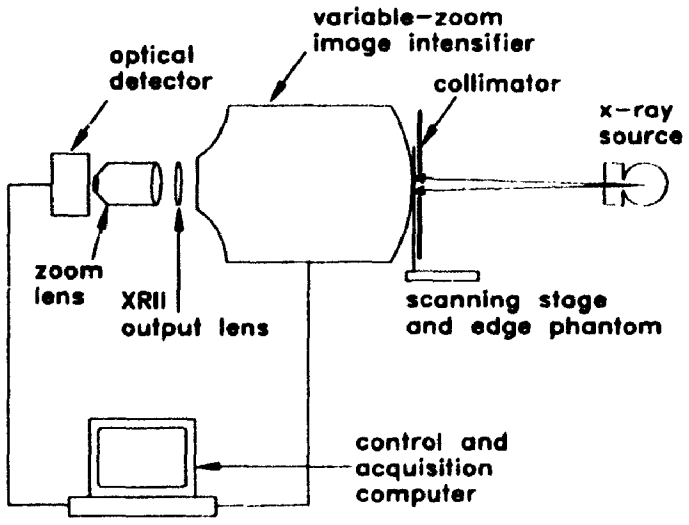

Figure 2.2: Schematic diagram of the experimental configuration used to measure the MTF's of the XRII-optical detector system. The optical detector was either a linear PDA or a video camera.

CA, USA) with element width of 25 μm and element height of 2.5 mm. The signal from the PDA was digitized with a 12-bit analog-to-digital converter. The video camera (Syracuse Scientific SS-800, Clay, New York, USA) was used in the 525-line interlaced mode, with the amplifier set to fixed gain and 12-MHz bandwidth. The video camera was not tuned to yield optimal resolution, in order to allow us to test the hypotheses made in the section 2.2. The effective pixel width of the video camera was 35 μm, with a height of 30 μm. Images acquired by the video camera were digitized with an 8-bit video frame grabber. The optical image of the XRII output phosphor was relayed to the optical detector via the built-in 90-mm *f*/1 XRII output lens and a Nikon NIKKOR 80-200 mm *f*/4 zoom lens.

For all experiments described in this chapter, we have defined the FOV to be the size of the image, referenced to the input of the XRII, that is seen by the 1024 elements of the PDA detector. The size of the FOV was determined from images of a 1-cm copper grid placed at the input of the XRII.

2.4.1 Calibration of V_{G2} and V_{G3}

It is necessary to determine the relationship between the optimal focus voltage V_{G2} and the zoom voltage V_{G3} for each FOV. This was accomplished by measuring the FOV and determining the optimal V_{G2} at 10 different zoom voltages. The optimal value of V_{G2} was determined by irradiating a 400 μm diameter copper wire placed at the input face of the XRII, while observing the signal from the PDA on an oscilloscope. The image of the wire appeared on the oscilloscope as a depression in the trace, which changed in magnitude as V_{G2} was varied. The optimum V_{G2} was the potential at which the magnitude of the depression in the trace was maximized and the width minimized.

2.4.2 System resolution quantification

The MTF's of the XRII-detector system were measured, for both the PDA and video-camera detectors, under conditions of optical and electronic zooming. Electronic zooming was achieved by setting the zoom-lens focal length to 80 mm, and varying V_{G3} and V_{G2} to give the desired FOV. Optical zooming was achieved by setting the electron optics of the XRII to give the largest FOV (24 cm) and using the zoom lens to magnify the image. During the MTF measurements, the zoom-lens aperture was maintained at $f/4$ to avoid changes in resolution due to lens aberrations at different f ratios. The effects of veiling glare were reduced by collimating the x-ray beam. Collimation was accomplished by placing a 1-mm wide slit in front of the XRII for the PDA experiments, and by adjusting the size of the lead collimator to the desired FOV for the video-camera experiments (see Fig. 2.2).

All MTF's were calculated from edge response functions (ERF). In acquiring the ERF's, we used the scanning-edge[11] and the slanted-edge[12,13] techniques with the PDA detector and the video camera, respectively, to avoid aliasing due to detector element spacing. Imaging a thin metal blade placed directly against the front face of the XRII ensured that no additional blurring was introduced due to the finite size of the x-ray tube focal spot.

The scanning-edge MTF measurement technique,[11] which is typically used with one-dimensional detectors, involves the translation of a high-contrast edge along the detector while acquiring an image. In the resulting image, each line represents an ERF, shifted by a known amount with respect to the ERF from the previous line. The shift is determined by the scanning speed and the read-out rate of the one-dimensional detector. The ERF's from each line are then combined into a single ERF which has a sampling interval smaller than the detector pixel spacing. The MTF is calculated by differentiating and Fourier transforming the oversampled ERF. This

process enables the characterization of the system resolution beyond the frequency, determined by the sampling rate of the optical detector, at which aliasing occurs.

The slanted-edge MTF measurement technique[12,13] is analogous to the scanning-edge technique for two-dimensional detectors. A metal blade with a straight edge is placed in front of the detector at a small angle with respect to a line defined by the optical-detector pixel grid. As with the scanning-edge technique, a line in an image of this slanted edge produces an ERF, which is shifted by a known amount with respect to the preceding line. The shift between two adjacent lines is determined by the angle at which the edge was placed with respect to the grid. An oversampled ERF can then be generated as described above.

2.4.2.1 *XRII-PDA resolution*

Measurements of the resolution of the XRII-PDA system were performed by translating a 0.5-mm thick tungsten edge at a constant rate of 0.13 mm s^{-1} across the input of the XRII, while the PDA signal was digitized at a rate of 60 scan lines per second. These images were first corrected for diode-to-diode sensitivity variation by dividing the images by a correction field, and then were processed, as described above, to obtain oversampled ERF curves. Since the PDA is linear in response[14] there was no need for non-linearity correction. For the XRII-PDA system, we obtained MTF measurements for five FOV's achieved electronically (ranging from 24 cm to 8 cm at the input of the XRII) and five FOV's achieved optically (ranging from 24 cm to 10 cm). All images were obtained at diagnostic exposure rates, with kVp settings varying from 60 to 105 kVp, and 3-mm added Al filtration.

2.4.2.2 *XRII-video-camera resolution*

The resolution of the XRII-video-camera system (in the direction parallel to the camera scan lines) was quantified from ERF's obtained from images of a 50-μm-thick copper edge placed at a small angle with respect to the vertical. An edge producing

a low-contrast image, was used to ensure we were operating the video camera in a region of linear response.[15] The contrast (given by $\Delta S/S$, where ΔS is the difference in signal level and S is the mean signal level) in the images of the copper edge varied between 10.4 and 11.7% depending on the x ray spectrum used. A neutral-density filter (OD 0.5) was introduced between the XRII and detector lens to maintain the optical output from the XRII within the detector range, without varying the lens aperture and without compromising photon statistics. The radiographic exposure parameters were 80-100 kVp, 3-mm added Al filtration, and the x-ray tube current was set to values ranging between 3 and 10 mA. We collected 540 images of the edge, each 512 pixels by 120 lines, and 540 images of a mask field. The images of the edge were averaged and corrected for spatial response variation.[16] All image lines were then combined to yield one oversampled ERF. The resolution of the XRII-video-camera system was characterized at FOV's of 24 cm and 10 cm, achieved by both optical and electronic zooming.

In addition to the MTF measurements, images of a bar-pattern test object were acquired at an FOV=10 cm to demonstrate visually the difference between optical and electronic zooming. The images were acquired with the zoom-lens f ratio set to f/5.6.

2.4.2.3 *Effect of x-ray spectrum on MTF measurements*

Since a variety of x-ray spectra are used in XRII-based radiography, we investigated the effects of changing the incident x-ray spectrum on image resolution. The MTF of the XRII-PDA system was measured with incident spectra of 60, 80 and 110 kVp. For these measurements the XRII image was magnified electronically to the smallest achievable FOV (8 cm), and an 85-mm Nikon lens at f/4 was used as the detector lens. The x-ray tube current was adjusted (between 25 and 100 mA depending on the spectrum used) to ensure maximum signal detected at the PDA,

without saturation. The scanning-edge technique described above was used to obtain the MTF's.

2.4.3 Detector resolution quantification

The MTF's of the PDA and the video camera were measured to determine their contribution to the degradation of system resolution. The resolution of both optical devices was measured with the 80-200 mm zoom lens coupled to a Nikon 85-mm lens, in place of the XRII output lens. To simulate the spectral output of the XRII, green light illumination ($\lambda = 565 \mu m$)[17] was used while acquiring images of a razor blade. The razor blade was slanted at an angle of 4° for the video-camera measurements and was scanned at a rate of 0.11 mm s^{-1} for the PDA measurements. The ERF's for the two detectors were measured with the zoom lens set to the two extreme focal lengths (80 and 200 mm), in order to determine if a significant degradation in resolution results when varying the focal length.

2.5 Results

2.5.1 Calibration of V_{G2} and V_{G3}

Figure 2.3 shows the relationship between zoom voltage, optimal focus voltage and the size of the FOV referenced to the input of the XRII. Cubic-spline interpolation of the zoom-voltage-FOV and focus-voltage-FOV relationships was used to generate a look-up table of V_{G3} and V_{G2} as a function of FOV within the range

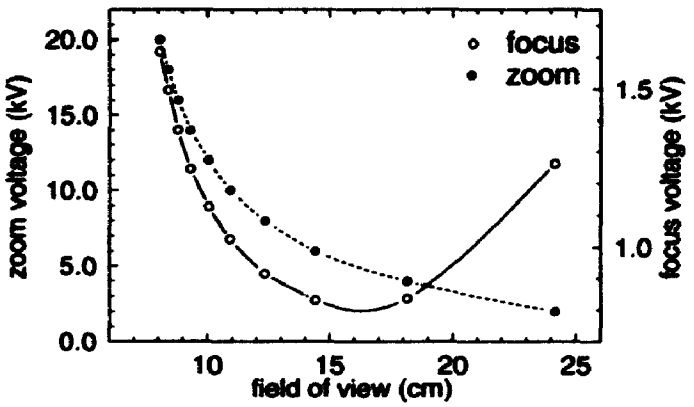

Figure 2.3: Relationship between the zoom voltage, focus voltage and the field of view referenced to the input of the XRII. The lines are cubic-spline interpolations of the experimental measurements.

of 24 cm to 8 cm. From these interpolated voltages, electronic zooming to a desired FOV was achieved using a 12-bit digital-to-analog converter (DAC) controlled by a PC/AT computer. The zoom voltage was controlled directly by the DAC, while the focus voltage was controlled by moving the stepper motor a known number of steps. The potentiometer position required for a certain focus voltage was determined to within one motor step, which is equivalent to 15 V. The zoom voltage and the focus voltage for a given FOV were stable over time, implying that a calibration procedure need only be performed once, when the modification is implemented.

Figure 2.3 also shows that the slope of the zoom-voltage-FOV curve increases as the FOV is reduced. At a zoom voltage of 20 kV the reduction in FOV with increasing V_{G3} occurs at a rate of 0.17 cm/kV, compared to 6.0 cm/kV at the largest FOV. Thus, increasing the zoom voltage past 20 kV would not lead to a significant reduction in the FOV.

2.5.2 X-ray spectrum effects on resolution

Figure 2.4 shows the MTF's of the XRII-PDA system, obtained with maximum electronic zooming (*i.e.*, maximum M_e), at 60 kVp and 110 kVp. A similar result was obtained at 80 kVp. Clearly, for this range of kVp's, system resolution is not a function of the spectrum of the incident x-ray beam. A small difference in resolution has been reported by

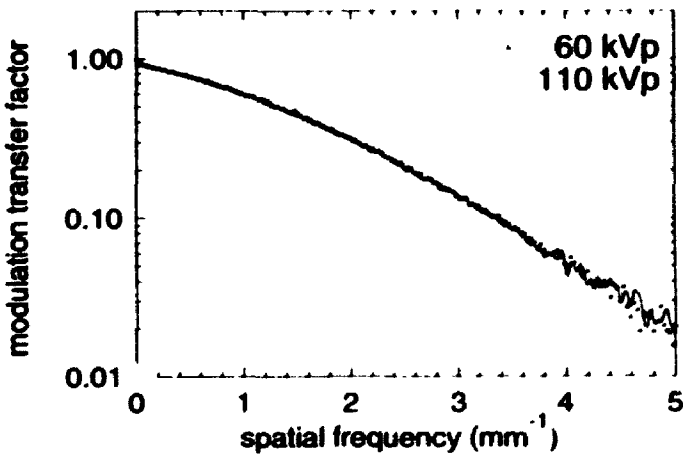

Figure 2.4: XRII-PDA system MTF's measured at 60 kVp and 110 kVp. For these experiments, the FOV was set to 8 cm by electronically zooming the XRII. All frequencies are referenced to the input of the XRII.

Rowlands *et al.*[18] when using monoenergetic x rays at energies just above and below the K-absorption edges of cesium and iodine. For the polyenergetic beams used here the fraction of the spectrum near the K edges is small and therefore these K-edge effects were not observed.

2.5.3 Optical-detector resolution

Figure 2.5 presents the MTF's of the two optical detectors as a function of spatial frequency, referenced to the plane of the detector. MTF's are plotted for each detector with the zoom lens set to 80 and 200-mm focal length. For the video camera, the frequency at which MTF = 0.1 ($f_{0.1}$) is 11.9 mm^{-1} when the lens is at 80 mm, and 11.1 mm^{-1} when the lens is at 200 mm. For the PDA, $f_{0.1}$ reduces from 27.5 mm^{-1} to 22.9 mm^{-1} when the lens focal length is changed from 80 to 200 mm. These results demonstrate that the MTF of the PDA is greater than that of the video camera, and both detector MTF's are degraded when the lens is zoomed.

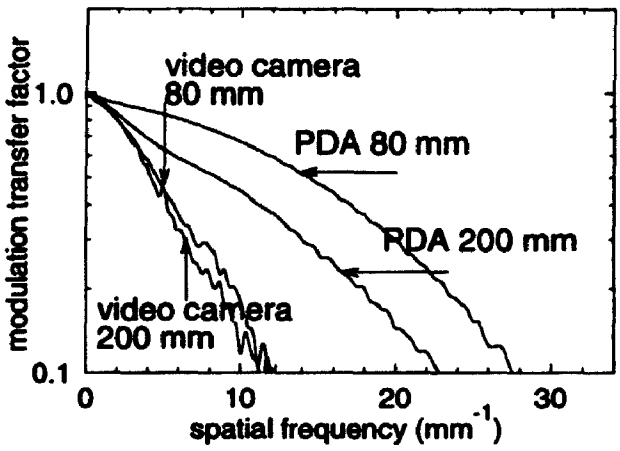

Figure 2.5: Plot of the MTF's of the PDA and the video camera. The optical MTF's of each detector were measured with the zoom-lens focal length adjusted to either 80 mm or 200 mm. All frequencies are referenced to the plane of the detector.

2.5.4. System resolution

2.5.4.1 *XRII-PDA resolution*

Figure 2.6 compares the MTF results obtained with the XRII-PDA system at FOV=24 cm (largest FOV) to those obtained at FOV=10 cm, by optical and electronic zooming. The effects of optical and electronic zooming are summarized in Fig. 2.7, where $f_{0.1}$ is plotted as a function of FOV. Electronic zooming from 24 cm to 10 cm

leads to an increase in $f_{0.1}$ by a factor of 2.2, while optical zooming by the same amount increases $f_{0.1}$ only by a factor of 1.3.

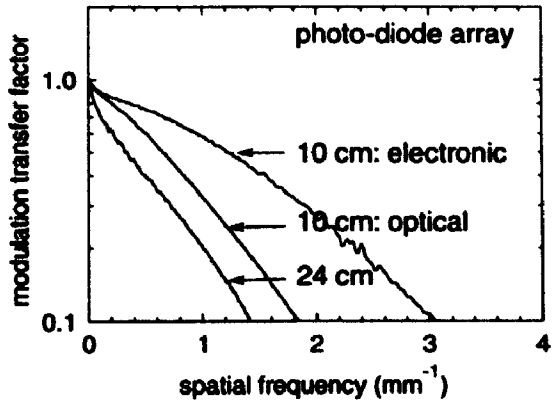

Figure 2.6: XRII-PDA system MTF's measured at FOV=10 cm obtained by electronic and optical zooming of the XRII image. These are compared to the maximum achievable FOV=24 cm.

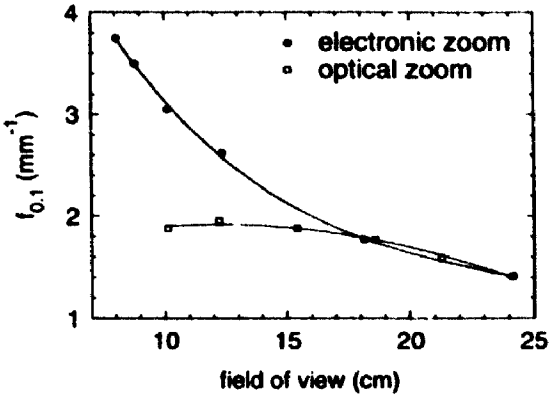

Figure 2.7: The frequency at which the MTF equals 0.1 ($f_{0.1}$) is plotted as a function of field of view for the XRII-PDA system. Results are presented for both optical and electronic zooming.

2.5.4.2 *XRII-video-camera resolution*

Figure 2.8 compares the effects of optical and electronic zooming on the system MTF when the video camera was coupled to the XRII. MTF's are plotted for FOV=24 cm and for optically and electronically zoomed FOV of 10 cm. Electronic zooming from 24 cm to 10 cm leads to an $f_{0.1}$ increase by a factor of 1.7, while optical zooming increases $f_{0.1}$ by a factor of 1.6.

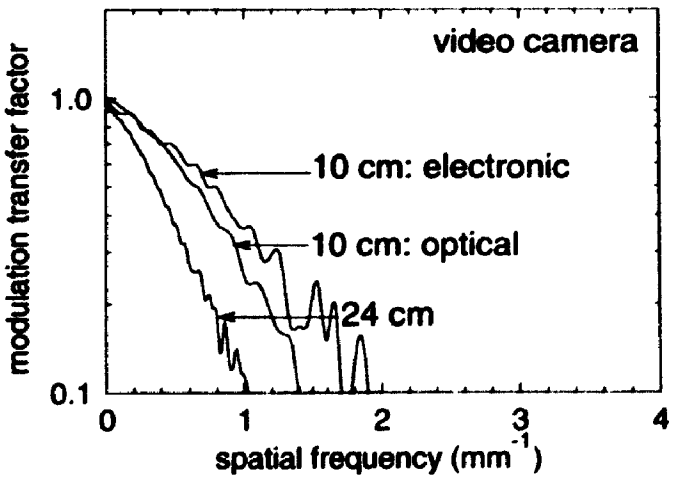

Figure 2.8: XRII-video camera system MTF's measured at FOV=10 cm obtained by electronic and optical zooming of the XRII image. The MTF for FOV=24 cm is common for both optical and electronic zooming.

The bar-pattern images shown in Fig. 2.9 visually compare the resolution of the XRII-video-camera system when the desired magnification is achieved by: (a) optical zooming and (b) electronic zooming. The FOV, referenced to the input of the intensifier for these images acquired with the video camera, was 10 cm. The figure shows that electronic zooming yields a small improvement in resolution when compared to optical zooming of the XRII-video-camera system.

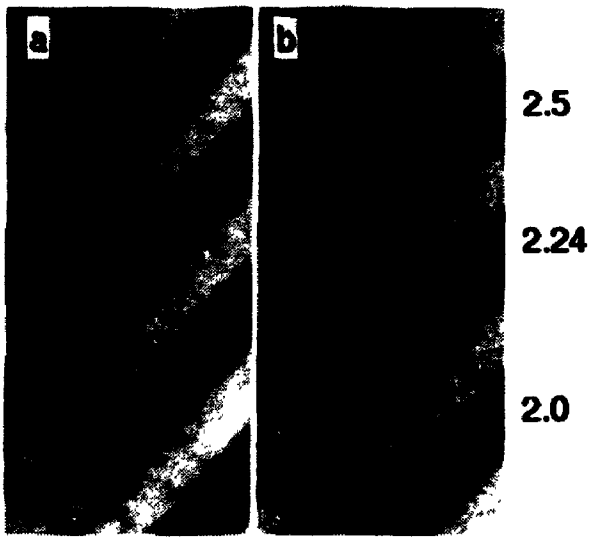

Figure 2.9: Images of a radiographic bar-pattern phantom obtained with the XRII-video camera system by: (a) optical zooming, and (b) electronic zooming to an FOV of 10 cm.

2.6 Discussion and Conclusions

We have modified a standard multiple-field XRII to vary electronically the image magnification between the input of the XRII and the output phosphor. The modification allows the zoom voltage V_{G2} and the focus voltage V_{G3} to be adjusted independently under computer control in order to achieve the desired magnification, while the image retains correct focus, without the introduction of further image distortion.[2] With this modification, which can be applied to any multiple-field XRII, the image can be zoomed continuously over a range of FOV's greater than that determined by the original specifications of the XRII.

An alternative, and easier to implement, means of obtaining the same continuous magnification would be to use an optical zoom lens. To determine the optimal zooming method for achieving increased resolution we compared optical

zooming to electronic zooming and found that electronic zooming provided a greater improvement in resolution with the PDA detector (Fig. 2.6 and Fig. 2.7). However, electronic zooming provided little benefit over optical zooming when the video camera was the detector (Fig. 2.8). In a recent publication, Rudin *et al.*[7] showed that, for an XRII-video-camera system, optical zooming and electronic zooming provided comparable improvements in resolution, in agreement with the results presented here. Our results suggest that this apparent "discrepancy" between the XRII-video-camera system and the XRII-PDA system is due to the difference in relative contribution to the MTF degradation of the XRII and the optical detector.

To test this hypothesis, we used the measurements of the resolution of the two optical detectors and of the two XRII-optical-detector systems to calculate $MTF_{xrii}(\frac{f}{M_e})$ using Eq. 2.1. These results are plotted in Fig. 2.10 for both detectors, when the same FOV was achieved by either optical or electronic zooming. In Fig. 2.10 we have also plotted the MTF's of the appropriate optical detector, with the frequency axis scaled to reference the *MTF*s to the input of the XRII. This enables the comparison of $MTF_{xrii}(\frac{f}{M_e})$ to $MTF_{det}(\frac{f}{M_e M_o})$ for the two systems at the same M_{tot}. From Fig. 2.10(a) and (b) it can be seen that the video camera and the XRII have equivalent *MTF*s, indicating that the XRII-video-camera system falls in the category described by case 3. In the Theory section (2.2) we postulated that for such systems electronic zooming will lead to a slightly better improvement in resolution than optical zooming, for the same total magnification. Our experimental results, for MTF_{sys} of the XRII-video-camera system (Fig. 2.8) confirm this hypothesis.

Similarly, Fig. 2.10(c) and (d) show that at the limiting frequency of the XRII-PDA system, MTF_{det} is significantly greater than MTF_{xrii}, indicating that the XRII-PDA system is an example of a system described by case 2. We predicted that for such systems electronic zooming would yield greater improvements in resolution than

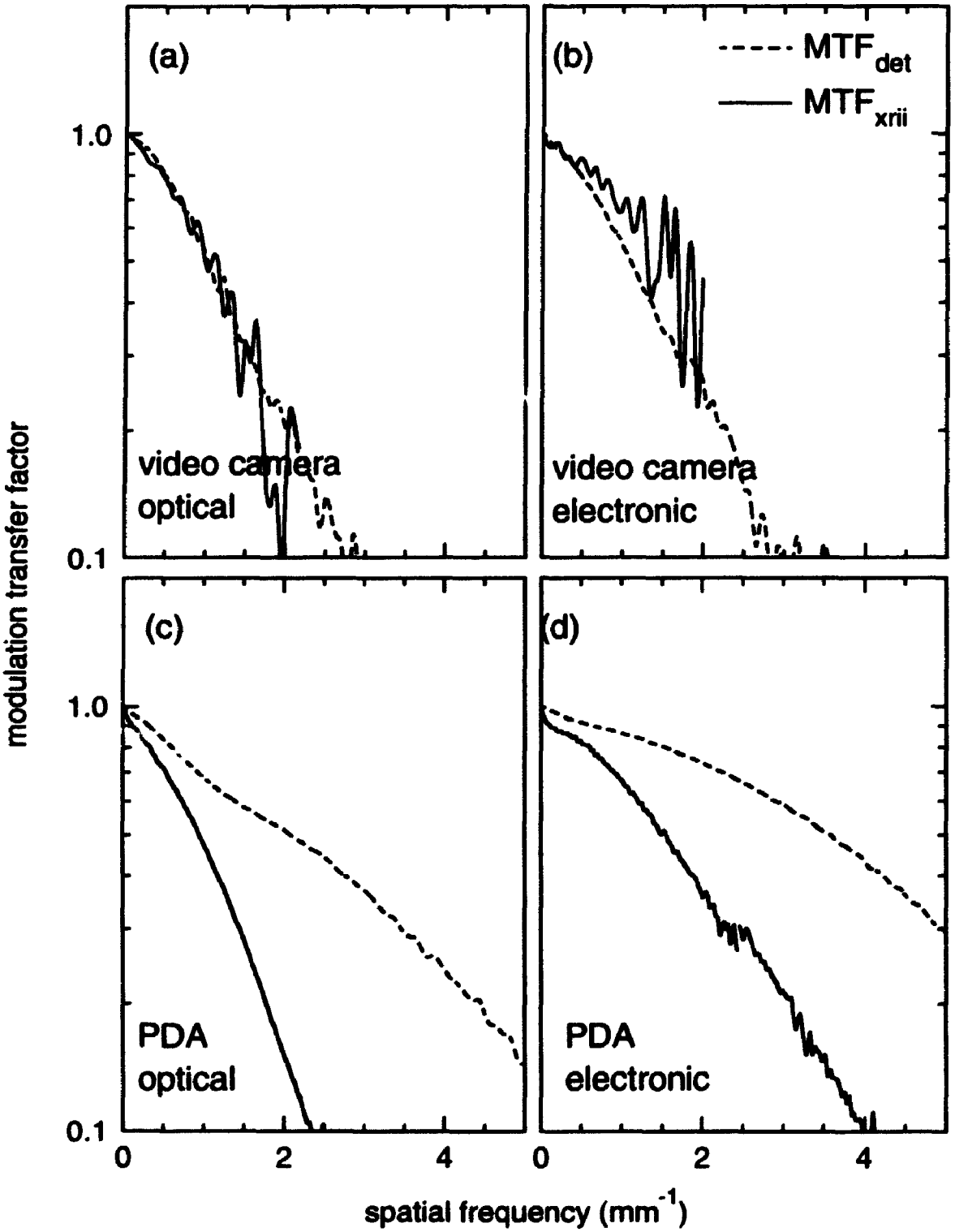

Figure 2.10: Comparison of MTF_{xrii} (solid curves) and MTF_{det} (dashed curves) for a FOV=10 cm. XRII-video camera system: (a) optical and (b) electronic zooming; XRII-PDA system: (c) optical and (d) electronic zooming.

optical zooming. The measurements of MTF_{sys} for the XRII-PDA system (Figs. 2.6 and 2.7) show a marked gain in resolution with electronic zooming over optical zooming, thus supporting this hypothesis.

In designing a complete system other factors must be considered when comparing optical and electronic zooming. As the image is zoomed by either technique, the brightness of the image at the optical detector is decreased because the number of photons per detector element is reduced. The image will either be noisier, or the input photon fluence must be increased to maintain the same quantum noise level. One also must consider the fact that the coupling lenses of a standard fluoroscopic system are matched and are optimized for the given system. Also, optical zoom lenses usually have smaller focal ratios than these dedicated lenses, resulting in reduced light transmission. Finally, one must consider the increase in image blurring which commonly occurs with increasing focal length (as seen in Fig. 2.5).

In summary, the decision of whether to magnify XRII images optically or electronically clearly depends on the relative resolving power of the XRII and the optical detector. We have shown that when the optical detector and the XRII contribute equally to the system resolution, as in the case of the XRII-video-camera system, only minor benefits are realized when zooming electronically rather than optically. However, if the XRII is the dominant factor which determines the system resolution, greater improvements in resolution can be achieved by electronic zooming rather than by optical zooming. Thus, electronic zooming always leads to increased resolution, while optical zooming may not have a significant effect on improving resolution. Therefore, we used the electronically zoomed XRII as the x-ray detector for the high-resolution dynamic CT scanner.

REFERENCES

1. M. Drangova, D.W. Holdsworth, K. Schulenburg and A. Fenster, "Table-top CT system for *in-vitro* analysis of arterial flow and distensibility," Proc. SPIE **1231**, 255-260 (1990).

2. D.W. Holdsworth, M. Drangova, K. Schulenburg, and A. Fenster, "A Table-top CT system for high-resolution volume imaging," Proc. SPIE **1231**, 239-245 (1990).

3. D.W. Holdsworth, P.J. Dunmore, M.R. Roach, and A. Fenster, "A digital-radiographic technique for *in vitro* tissue thickness measurements using iodine displacement," Med. Phys., **19** 545-554 (1992).

4. D.W. Holdsworth, M. Drangova, and A. Fenster, "A high-resolution XRII-based quantitative volume CT scanner," Med. Phys. **20**, 449-462 (1992).

5. J.M. Boone, G.M. Alexander and J.A. Seibert, "Personal computer fluoroscopy CT system for small animal and specimen research," Radiology **177**, 136 (1990) [Abs.]

6. L.E. Feldkamp, S.A. Goldstein, A.M. Parfitt, G. Jesion and M. Kleerekoper, "The direct examination of three-dimensional bone architecture *in vitro* by computed tomography," J. of Bone and Min. Res. **4**, 3-11 (1989).

7. S. Rudin, D.R. Bednarek, R. Wong, " Improving fluoroscopic image quality with continuously variable zoom magnification," Med. Phys. **18**, 972-977 (1991).

8. J. Vine, "The design of electrostatic zoom image intensifiers," Adv. Electron. Electron Phys. **28A**, 537-543 (1969).

9. K.G. Vosburgh, R.K. Swank, J.M. Houston, "X-ray image intensifiers," Adv. Electron. Electron Phys. **43**, 205-245 (1977).

10. C.D. Robbins, R.S. Enck, Jr., and J.P.Sackinger, "High -performance continuous zoom x-ray image intensifier," Proc. SPIE **35**, 23-32 (1972).

11. F. Chazallet and J. Glasser, "Theoretical bases and measurement of the MTF of integrated image sensors," Proc. SPIE **549**, 131-144 (1985).

12. P.F. Judy, "The line spread function and modulation transfer function of a computed tomographic scanner," Med. Phys. **3**, 233-236 (1976).

13. D.W. Holdsworth, R.K. Gerson, and A. Fenster, "A time-delay integration charge-coupled device camera for slot-scanned digital radiography," Med. Phys. **17**, 876-886 (1990).

14. I.A. Cunningham and A Fenster, "A photodiode array x-ray imaging system for digital angiography," Med. Phys. **11**, 303-310 (1984).

15. A.A.J. Franken and W.J.L. Scheren, "The influence of the camera tube on the temporal modulation transfer function in diagnostic x-ray television," Med. Mundi **17**, 121-123 (1972).

16. J.M. Boone, J.A. Seibert, W.A. Barrett, and E.A. Blood, "Analysis and correction of imperfections in the image intensifier-TV-digitizer imaging chain," Med. Phys. **18**, 236-242 (1991).

17. J.A. Rowlands, K.S. Schulenburg, and G. DeCrescenzo, "A light source for testing radiological television cameras," Med. Phys. **16**, 1-6 (1989).

18. J.A. Rowlands, K.W. Taylor, H.N. Cardinal, "Imaging and noise limitations of cesium iodide x-ray image intensifiers," Proc. SPIE **454**, 366-376 (1984).

3. HIGH-RESOLUTION LABORATORY CT SCANNER FOR DYNAMIC IMAGING

3.1 INTRODUCTION

High-quality transverse images of static objects are produced by conventional clinical CT scanners. However, conventional scanners require about 1 s to acquire an image. Thus, for imaging moving objects, such as the beating heart, specialized scanners must be used.[1,2,3] CT has also been used in basic research, for imaging pathological specimens and small animals. Unfortunately, since clinical scanners are not designed to image small objects, they do not have sufficient resolution for these applications. Thus, a number of researchers have developed specialized CT scanners to image vascular specimens, bone samples, and small animals.[4,5,6,7] These scanners can be used to produce high-resolution quantitative images of static samples, but none has sufficient temporal resolution to image moving objects. Applications for a high-resolution dynamic CT scanner include *ex vivo* imaging of arterial specimens subjected to physiological pressure conditions, in order to study the dynamic elastic properties of the vessels; imaging the flow patterns in the same excised vessels in an attempt to link disease sites to haemodynamic effects; or imaging motion, such as that of the heart, in experimental animals.

Chapter three describes a high-resolution dynamic CT scanner, which I developed to image objects undergoing periodic motion. The dynamic CT scanner is based on the modified conventional x-ray image intensifier (XRII) and linear photo-diode-array detector (PDA), which were described in chapter two. The scanner obtains gated projections of a single slice, which are later recombined and reconstructed into cross-sectional images of the object at different phases of its motion cycle. Here I describe the scanner and the method we use to obtain the cross-sectional images. A complete characterization of the

system performance, in terms of spatial resolution, temporal response, precision and accuracy is also presented, and the experimental results are compared to theoretical predictions. The material presented in this chapter comprises the body of a paper entitled "A laboratory CT scanner for dynamic imaging," which has been submitted for publication in Medical Physics.

3.2 Acquisition Geometry

The acquisition geometry of the dynamic CT scanner is shown in Fig. 3.1. For consistency, we have used nomenclature similar to that introduced by Holdsworth *et al.*[4] The linear detector, consisting of n elements spaced $\Delta x'$ apart, is placed at a distance F from the x-ray source and is centered about $x' = 0$. The object rotates in front of the detector about the z axis, which is perpendicular to the x-y reconstruction plane and is a distance R_{fan} from the source. The magnification of the object is thus given by $M = F/R_{fan}$. The reconstructed image contains LxL elements, spaced $\Delta x = \Delta x' n/(ML)$ apart. The half-fan angle is determined by F and the size of the detector as $\delta = \tan^{-1}(\frac{n\Delta x'}{2F})$. The maximum reconstruction radius is given by $r_{max} = L\Delta x/2$, where $r = (x^2+y^2)^{1/2}$. As the object is rotated in angular increments $\Delta\beta$ over $0<\beta<\pi+2\delta$, n_{ang} views are collected to complete the set of projections required for reconstruction.

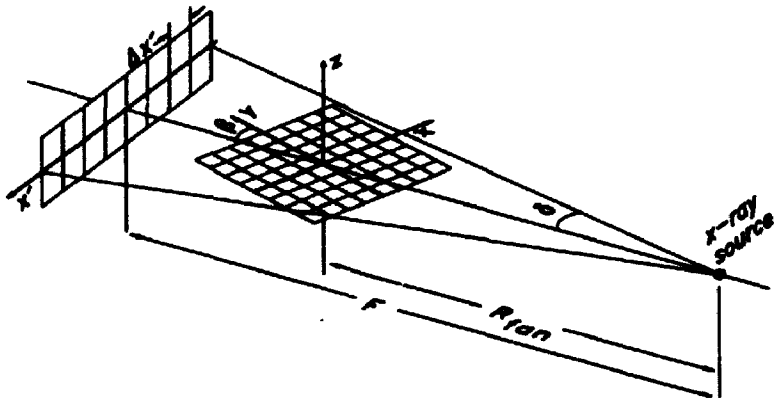

Figure 3.1: Schematic diagram of the acquisition geometry of the dynamic CT scanner.

3.3 System Description

3.3.1 The imaging system

The high-resolution dynamic CT scanner is shown schematically in Fig. 3.2. The x-ray beam, collimated by a narrow slit, is detected at the input phosphor of

the CsI XRII, after passing through the object. The optical image from the XRII is relayed by a pair of collimating lenses (the 90-mm XRII output lens and an 85-mm Nikon lens) and detected by a 1024-element linear photo-diode array (Reticon RL1024S, EG&G Reticon, Sunnyvale CA, USA). The use of this sensor array with an XRII for scanned-projection digital radiography has been described previously.[8] The sensor elements are 2.5-mm high and are spaced on 25-μm centres. The output of the PDA is digitized to 12 bits with a high speed analog-to-digital converter (MetraByte DAS-50, MetraByte Corporation, Taunton MA, USA) and then stored in a PC-AT computer. The signal is continuously integrated and is sampled at a rate of 60.73 image lines per second (equivalent to an exposure time Δt = 16.47 *ms*). The read-out rate of the detector can be increased to as much as 300 lines per second, but as the read-out rate is increased the number of detected x-ray quanta decreases, thereby increasing the statistical noise. Also, since we require that good photon statistics are maintained for all experiments, we used only 512 elements of the detector array and varied the XRII FOV. Thus, for larger objects the best resolution was not achieved.

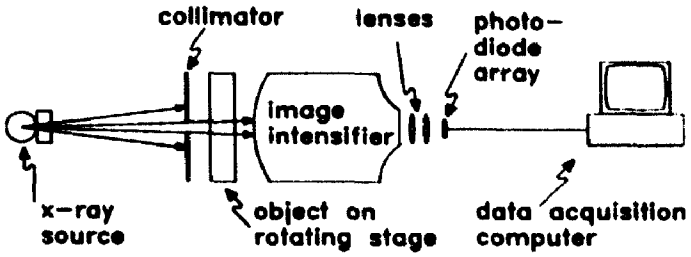

Figure 3.2: Schematic diagram of the dynamic CT scanner.

The x-ray source is a rotating-tungsten anode tube (Dynamax 67, Machlett Laboratories, Connecticut, USA) with a nominal focal-spot size of 1.0 mm and inherent filtration equivalent to 0.5-mm Al. Additional filtration of 3.0-mm Al was introduced to reduce the image artifacts caused by beam hardening. For all the studies presented in this paper, an x-ray beam generated at 90 kVp was used,

with tube current varying between 25 and 200 mA. A 1-mm lead collimator placed in front of the object determines the section of the sample to be imaged and also reduces x-ray scatter and XRII veiling glare.[8]

The XRII, which has been modified to provide continuously variable electronic image zooming,[9] was placed at a distance $F = 75$ cm from the x-ray source. Varying the active field-of-view of the XRII between 4 and 12 cm allows the optimum resolution to be chosen for a given application. For the experiments described here the active field-of-view (FOV) is that seen by 512 PDA elements.

3.3.2 The sample holder

The object under examination is mounted in an acrylic tube, surrounded by an equalization bath, and mounted on a rotating stage. In Fig. 3.3 we show schematically how a sample, such as an excised artery, is mounted for imaging. The rotating stage is controlled by the acquisition computer with angular precision of 0.225°. Depending on the application, the acrylic tube may be filled with dilute iodinated contrast agent, water, or air in order to optimize the contrast between the object and the surroundings. The attenuation of the fluid in the equalization bath also can be selected to provide x-ray path length equalization. This reduces the dynamic range requirements of the system, and the additional filtration reduces beam-

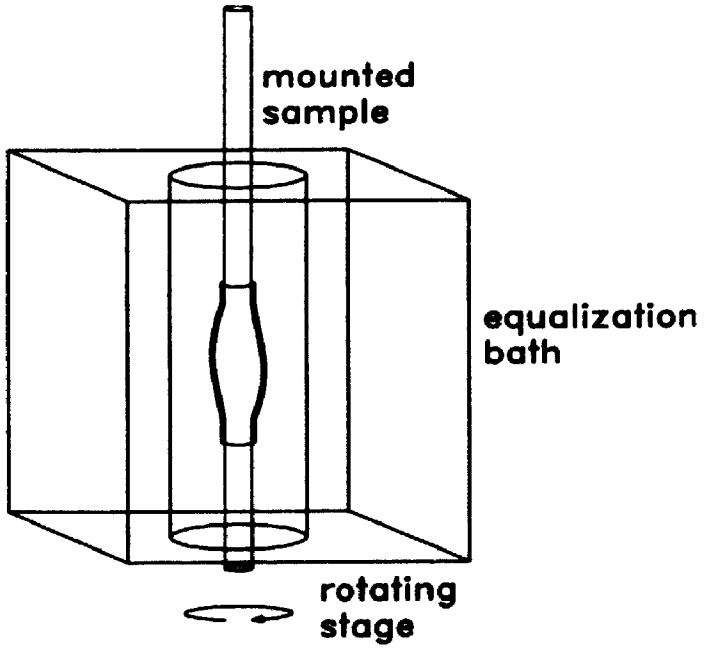

Figure 3.3: Schematic diagram of the sample holder, equalization bath and rotating stage.

hardening artefacts in the reconstructed images. The width of the equalization bath (d_{bath}) can vary up to 17 cm, depending on the size of the object being imaged. A second computer-controlled stage moves the sample vertically, thus allowing the investigation of different slices of the sample. The object can be placed at different distances R_{fan} from the source, thereby providing radiographic magnification.

3.3.3 Data acquisition and analysis

The system can be used in two acquisition modes to obtain CT images either of (1) static objects, or (2) objects exhibiting repetitive dynamic behaviour. For imaging of static samples, our system behaves like a third generation clinical CT scanner, but rather than rotating the x-ray source and detector, the sample is rotated during image acquisition. Typical radiographic parameters are 90 kVp, 3-mm added Al filtration, and 100 mA. The scan times for acquiring images of static objects are 4.15 s for fan-beam reconstruction over 360° and 3.35 s for parallel-beam reconstruction (over 180°).

To image an object undergoing periodic motion, such as a pulsating arterial specimen, a set of projection images from different viewing angles is obtained. At each angular position a sequence of radiographic projections of a single slice through the object is obtained over a period of time equal to at least one period of the motion cycle. For clarity, we refer to these sequences as "time-evolved" projections. As an example, we show schematically a set of time-evolved projections of a "pulsating artery" in Fig. 3.4. The acquisition of each time-evolved projection is triggered by a gating signal, marking the start of the motion cycle. Since the PDA cannot be triggered in coincidence with the gating pulse, the gating pulse may not coincide with the start of data read-out. Thus, a temporal delay is introduced, which varies randomly between 0 and Δt.

Typically, time-evolved projections are acquired at angular increments $\Delta\beta = 1.5°$. For small objects, where the fan angle is small ($\delta \approx \Delta\beta$), 100 views are obtained over π radians and parallel-beam reconstruction is used.[13] For larger objects, where the fan angle is large, 200 time-evolved projections are obtained over 2π radians, and fan-bean reconstruction is used. Typically, the radiographic parameters used in this mode are 90 kVp, 3-mm added Al filtration and tube current varying between 50 and 200 mA, depending on the object size. The acquisition time for each time-evolved projection spans the extent of one motion cycle.

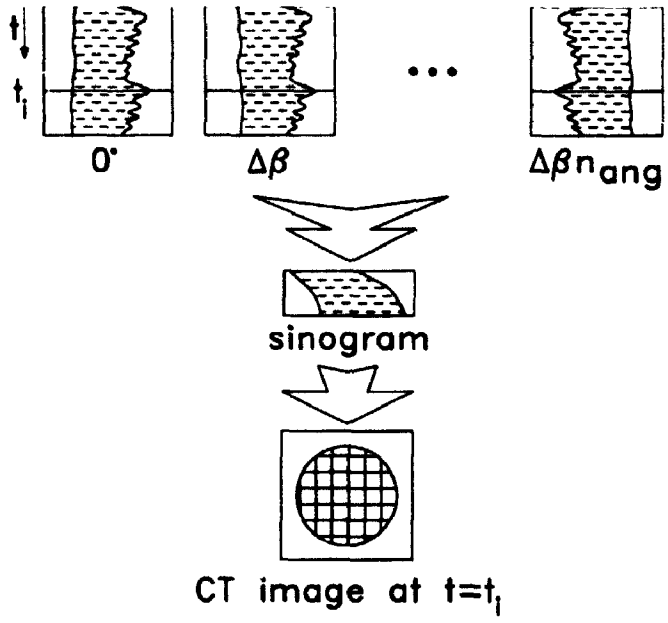

Figure 3.4: Diagram showing a set of time-evolved projections of a pulsating artery, which distends only on one side. These data are reformatted into sinograms and reconstructed to yield transverse images at difference phases of the motion cycle.

In both modes of operation, fixed-pattern mottle, which is introduced by XRII and diode-to-diode response nonunuformities, is corrected by a "bright field." The bright field is the average of a set of projections through the equalization bath alone, collected before and/or after acquisition of the projection data. A sufficient number of projections is acquired to ensure that no additional photon noise is introduced during the bright-field correction procedure. The correction is performed by pixel-to-pixel normalization of the projections by the bright field.[10] Prior to the normalization, a "dark field" is subtracted from each image in order to

remove any DC offset in the signal. A dark field is an average of 50 image lines collected in the absence of signal. Finally, a correction for temporal fluctuations in x-ray beam intensity is performed, using a reference signal obtained from a uniformly exposed strips at the edges of the projections.

For stationary objects, the corrected projection data are then reconstructed. For moving objects, the corrected time-evolved projections are reformatted as shown in Fig. 3.4. A set of sinograms corresponding to different instances in time is extracted from the complete set of time-evolved projections. The sinograms are then reconstructed by a convolution-backprojection reconstruction algorithm.[11] The schematic representation in Fig. 3.4 shows the extraction and reconstruction of one such sinogram, corresponding to one point in the motion cycle of the "pulsating artery." For fan-beam reconstructions a convolution kernel described by Herman *et al.*[12] is used, and for parallel-beam reconstruction a kernel described by Shepp and Logan[13] is employed.

3.4 THEORY

3.4.1 Spatial resolution

The spatial resolution of a CT scanner can be described as a cascade of system stages.[4,14] For the complete system, the modulation transfer function MTF_{CT} is a product of the *MTF*s due to the focal spot, the detector, and the reconstruction algorithm

$$MTF_{CT}(f) = MTF_{foc}(f) \cdot MTF_{sys}(f) \cdot MTF_{alg}(f) , \qquad (3.1)$$

where *foc*, *sys*, and *alg* refer to the focal spot, detector system, and reconstruction filter algorithm, respectively and f is the spatial frequency referenced to the image plane. The focal-spot *MTF* is given by[4,15]

$$MTF_{foc}(f) = \left| sinc\left(f \cdot a_{foc}\frac{(M-1)}{M}\right)\right|, \qquad (3.2)$$

where $sinc(x) \doteq \frac{\sin(\pi x)}{\pi x}$, M is the geometric magnification, and a_{foc} is the focal-spot width. We have shown previously that for the XRII-PDA detector, MTF_{sys} is dominated by the *MTF* of the XRII[9] (see chapter two) and therefore MTF_{sys} cannot be predicted, but must be measured.

The *MTF* degradation due to the reconstruction algorithm results from the interpolation between sampled points in the projections and the application of a convolution filter. Holdsworth *et al.*[4] have shown that assuming linear interpolation[16,17] and convolution with the discrete Shepp-Logan filter function[13,17] MTF_{alg} is given by

$$MTF_{alg}(f) = \left| sinc^3(f\,\Delta x)\right| \qquad (3.3)$$

and provides a good approximation of the resolution degradation due to the reconstruction algorithm for parallel-beam and small-angle fan-beam reconstructions.

3.4.2 Temporal response

The inherent spatial resolution of any dynamic CT scanner is degraded by object motion. The extent of the degradation depends on the velocity of the moving object and the exposure time Δt. For scanners, like the one described in this paper, where the acquisition of each projection is gated to the motion cycle, the resolution is also degraded if the start of image acquisition is not exactly synchronised with the arrival of the gating pulse (see section 3.3.3).

To describe the resolution degradation due to: (1) the finite exposure time and (2) the random delay between the gating pulse and the start of data

acquisition, we consider an idealized object $\delta(x-x_o, y-y_o)$, moving in the x-y plane. Let the object move in periodic fashion in an arbitrary direction d. Also, let the velocity magnitude over a small interval T of the period T_o be given by

$$v(t) = v \qquad 0 \le t \le T \qquad (T < T_o). \tag{3.4}$$

In Eq. 3.4, the duration of the interval T is much greater than the exposure time Δt. Thus, if the start of the acquisition of each view is near the beginning of the period, the velocity can be considered to be constant over the acquisition of each view. First, consider the case where image acquisition is perfectly synchronised to the gating signal. The total distance travelled by the object during the exposure for one view is $v\Delta t$ and, since the object is moving periodically, this distance is the same for each view. Consequently, the reconstructed image is equivalent to that of a stationary object of width $v\Delta t$. Thus, the finite exposure time causes the system resolution to be degraded by[18]

$$E(d) = \frac{1}{v\Delta t} rect(\frac{d}{v\Delta t}) .$$

Next, consider the further resolution degradation that occurs due to the random delay between the gating signal and the start of data acquisition. When the start of data acquisition follows the gating pulse by a delay, randomly varying between 0 and Δt, the probability of recording the object at a given position is given by the probability density function

$$P(d) = \frac{1}{v\Delta t} rect(\frac{d}{v\Delta t}) .$$

Thus, the blurring due to randomly-triggered exposure of width Δt is given by

$$\int_{-\infty}^{\infty} E(d-\zeta)P(\zeta)\,d\zeta = \int_{-\infty}^{\infty} \frac{1}{v\Delta t} rect(\frac{d-\zeta}{v\Delta t}) \; \frac{1}{v\Delta t} rect(\frac{\zeta}{v\Delta t}) \; d\zeta$$

where ζ is the integration variable. Hence, the resolution in the direction of motion is degraded by the effects of convolution with *E(d)* and *P(d)*. In the case described here, where both blurring functions are *rects* of the same width ($v\Delta t$), the modulation transfer function for objects moving with velocity $v(t)$ is given by

$$MTF_{vel}(f, v) = MTF_{CT}(f) \cdot sinc^2(v\Delta t f) \ . \tag{3.5}$$

3.4.3 Noise

Expressions that predict the variance in the reconstructed value of the linear attenuation coefficient σ_μ^2 in CT have been derived by a number of authors.[19,20,21,22] Faulkner and Moores[22] derived an expression for σ_μ^2 for a point in the center of a uniform, circular object placed in an attenuating water bath that yields flat projection profiles. Holdsworth *et al.*[4] adapted that expression to include signal-independent detector noise σ_{sys}

$$\sigma_\mu^2 = \frac{\pi^2}{12\Delta x^2 n_{ang} \bar{N}} + \sigma_{sys}^2 \ , \tag{3.6}$$

where $\bar{N}$, the number of photons detected per projected ray-sum, is given by[22]

$$\bar{N} = \frac{\Phi J \Delta t \, n \, W H \eta \, e^{(-\bar{\mu} d_{bath})}}{L} \ . \tag{3.7}$$

In Eq. 3.7, Φ is the fluence rate per mA at the input of the XRII, J is the tube current, Δt is the exposure time, W and H are the detector width and height, respectively, η is the quantum detector efficiency, $\bar{\mu}$ is the mean attenuation coefficient of the object and the attenuating bath, and d_{bath} is the thickness of the attenuating bath. For the CT scanner described here, H is determined by the width of the collimator, while W is determined by the detector *MTF*. The

equivalent detector width W_{eff} can be calculated from the detector noise-equivalent bandpass[4,23,24]

$$W_{eff} = \frac{1}{2N_e} = \frac{1}{2\int_{-\infty}^{\infty} MTF_{sys}^2(f)\,df}. \tag{3.8}$$

3.5 Experimental Methods

3.5.1 Spatial resolution

The measurement of MTF_{sys} was described in detail in chapter two. Briefly, images of a 0.5-mm thick tantalum edge were collected as the edge was translated in front of the XRII at a constant rate of 0.13 mm s^{-1}.[9] From these images, a highly-sampled edge response function was obtained and then Fourier transformed. Using this technique, $MTF_{sys}(f)$ could be characterised without aliasing for frequencies higher than the Nyquist frequency.[25,26]

The width of the focal spot was measured from a radiograph of a 0.03-mm wide slit oriented perpendicular to the *x-y* plane. A slit was used instead of a pinhole since only the width of the focal spot affects the resolution. The radiographic parameters for the focal spot measurements were 90 kVp, 100 mA, and the magnification was M=11.94.

The resolution of the CT images was characterised by imaging an acrylic hemi-cylinder, which was machined flat along a diameter and inserted in an acrylic tube. For the *MTF* calculations this phantom was scanned in air, thus providing a high-contrast image of an edge. To characterise the *MTF* for frequencies above the Nyquist frequency, we used the technique described by Judy[25] and aligned the edge at a small angle with respect to the *y* axis of the reconstruction plane.

*MTF*s of the detector and the CT reconstructions were measured for two different fields-of-view.

3.5.2 Temporal resolution

The temporal resolution of the system was evaluated by imaging a phantom consisting of a 70-μm diameter copper wire mounted in a 6-mm lucite tube. The tube was positioned on a reciprocating stage, as shown in Fig. 3.5. The stage platform was driven by an eccentric shaft on an aluminum flywheel. The rotation rate of the flywheel was maintained by a DC servo-motor at a constant frequency of 1.83 Hz, resulting in sinusoidal stage motion with an

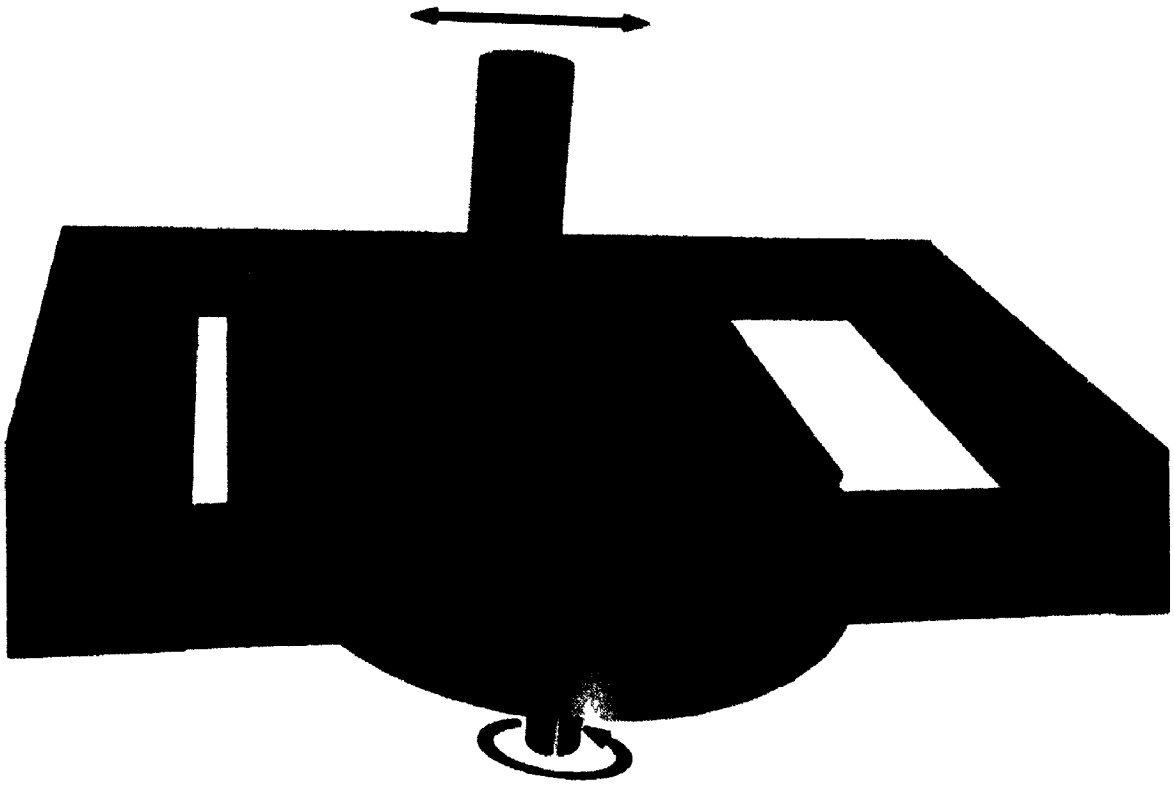

Figure 3.5: Illustration of the reciprocating stage used in the temporal resolution experiments. The thin copper wire underwent sinusoidal motion as the flywheel rotated at a constant rate. The entire assembly was mounted on a rotating stage.

amplitude of 0.94 cm and a maximum velocity of 10.76 cm s^{-1}. The XRII was zoomed to a *FOV* of 40 mm. The proximity of the reciprocating stage to the XRII introduced undesirable distortions in the images, which also varied as the stage was rotated to different view angles β. To overcome this problem, the reciprocating stage was moved away from the XRII (*M = 1.3*) and separate bright fields were collected for different β's. Gated time-evolved projections were collected from 240 view angles over 2π radians and transverse CT images of the wire were reconstructed. Each CT image shows the wire at a point in its motion cycle when it is moving with velocity $\bar{v}$ (see appendix 3.1). From the images of the wire, line-spread functions were obtained and Fourier transformed to provide *MTF*'s of the system for objects moving at velocities up to 10.6 cm s^{-1}.

3.5.3 Noise measurements

The linearity and precision of the dynamic CT scanner were evaluated from images of a phantom consisting of a variety of objects with known linear attenuation coefficients.[4] The mean attenuation coefficients $\bar{\mu}$ varied between 3.5×10^{-4} cm^{-1} and 1.15 cm^{-1} for an incident beam at 90 kVp with 3-mm added Al filtration. The mean attenuation coefficients were calculated based on the material composition, x-ray spectrum and the effects of filtration.[27] From the images, the mean CT number and the standard deviation were determined for each material. In addition, the effect of quantum noise was evaluated by imaging a circular water-filled phantom, placed in an 8-cm thick equalization bath, with radiographic parameters as described above, but with the x-ray tube current varied over the range 25 to 200 mA.

3.5.4 Geometrical accuracy

The geometrical accuracy and precision of the reconstructed images were characterised by imaging a set of coaxial Lucite cylinders with diameters varying

between 6 and 70 mm.[4] The boundary between the cylinders and the air surrounding them was determined by thresholding the CT images at a level equal to the average of the CT numbers of Lucite and air. From the thresholded images, the tube circumferences were calculated from the boundaries using chain-coding techniques.[28] The precision in the measurements was assessed from the calculated circumferences from 10 different images of the Lucite cylinders.

3.6 Results

3.6.1 Spatial resolution

Measurements of $MTF_{sys}(f)$ are presented in detail in chapter two for a wide range of *FOV's*, achieved by both optical and electro-optical zooming. In Fig. 3.6(a) we show $MTF_{sys}(f)$ for $\Delta x' = 80\mu m$ and $M = 1.08$, along with the corresponding $MTF_{CT}(f)$. The full-width-at-half-maximum of the focal spot was measured to be 1.12 mm and $MTF_{foc}(f)$ was calculated using Eq. 3.2, with $a_{foc} = 1.12$ mm, and was plotted in Fig. 3.6(a). $MTF_{alg}(f)$ was calculated from Eq. 3.3 and was used along with $MTF_{sys}(f)$ and $MTF_{foc}(f)$ to provide a theoretical

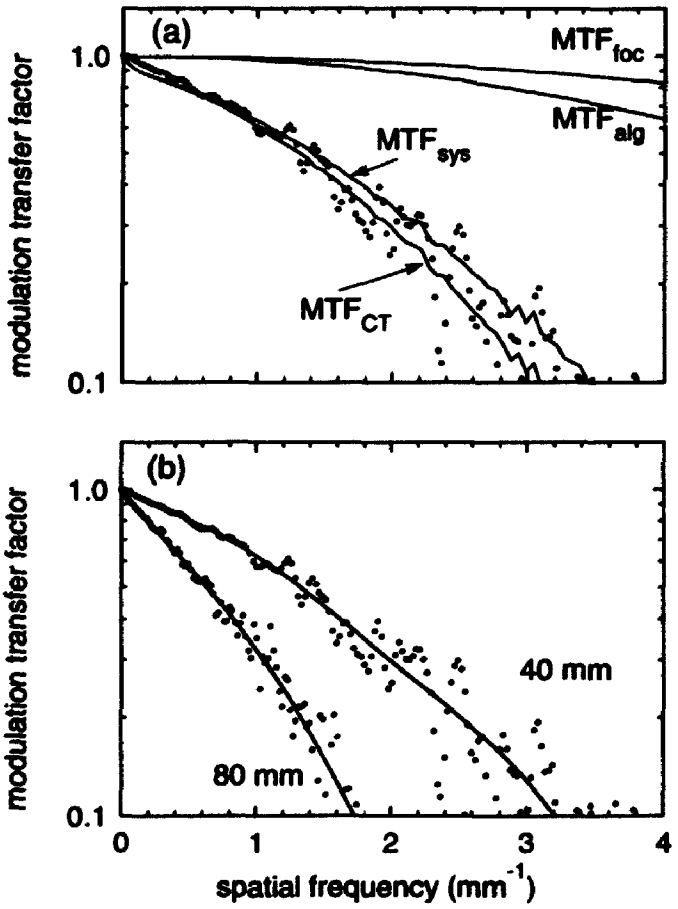

Figure 3.6: (a) Measured $MTF_{CT}(f)$ for $FOV = 40$ mm is compared to the theoretically derived curve. (b) MTF_{CT} for two fields of view.

estimate of $MTF_{CT}(f)$ based on Eq. 3.1. This theoretical estimate, shown in Fig. 3.6(a), is in good agreement with the measured $MTF_{CT}(f)$.

The spatial resolution of the CT images was measured for two *FOV*'s. Figure 3.6(b) shows $MTF_{CT}(f)$ for $FOV = 40\ mm$ ($\Delta x' = 80\mu m$) and $FOV = 80\ mm$ ($\Delta x' = 160\mu m$), with radiographic magnification $M = 1.08$. The frequency at which $MTF_{CT}(f) = 0.1$ ($f_{0.1}$) is 3.2 mm^{-1} for the smallest field-of-view and 1.76 mm^{-1} for the larger one.

3.6.2 Temporal resolution

The images of the moving Cu wire and acrylic tube, are shown in Fig. 3.7(a) for $\bar{v} = 1$ cm s^{-1} and in Fig. 3.7(b) for $\bar{v} = 10.6$ cm s^{-1}. The

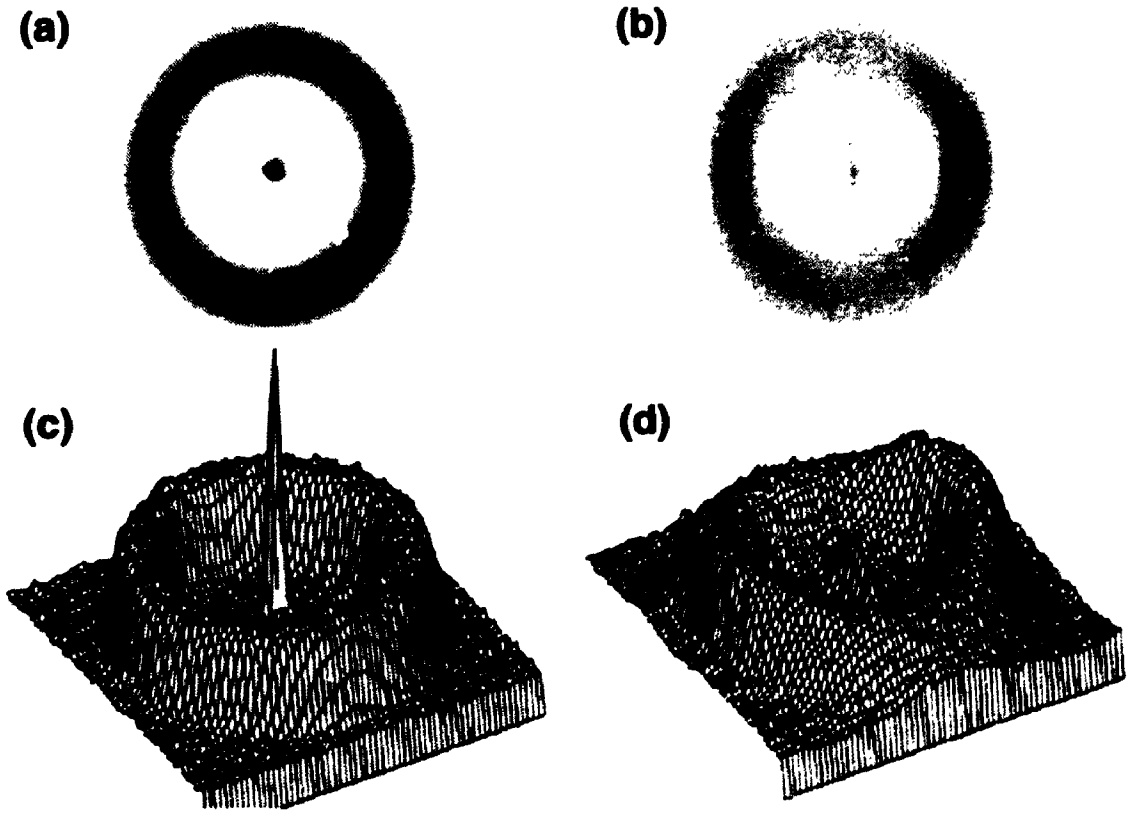

Figure 3.7: Images of the motion phantom at 1 cm s^{-1} (a) and 10.6 cm s^{-1} (b). The Cu wire and lucite tube are seen. Point-spread functions are shown in (c) and (d) for 1 and 10.6 cm s^{-1}, respectively.

corresponding two-dimensional point-spread functions are shown in Figs. 3.7(c) and (d), respectively. Since in our experiment $v(t)$ was not a constant, but varied sinusoidally, the velocities are calculated as the means over the exposure time Δt. The derivations for the expressions used to calculate the mean velocities and the standard deviations in the velocities are presented in appendix 3.1.

Figure 3.8(a) shows $MTF_{vel}(f,v)$ for a range of mean velocities. These MTF's were calculated from images such as those shown in Fig. 3.7. These plots are summarized in Fig. 3.8(b), where $f_{0.1}$ is plotted as a function of $\bar{v}$. The values derived using Eq. 3.5 are plotted as a solid line. The limiting resolution, characterized by $f_{0.1}$, is reduced by 9% for objects moving at $\bar{v}$ = 1 cm s^{-1}, and by 40% when $\bar{v}$ = 3 cm s^{-1}. For a velocity of 8 cm s^{-1}, $f_{0.1}$ is about 0.6 mm^{-1}.

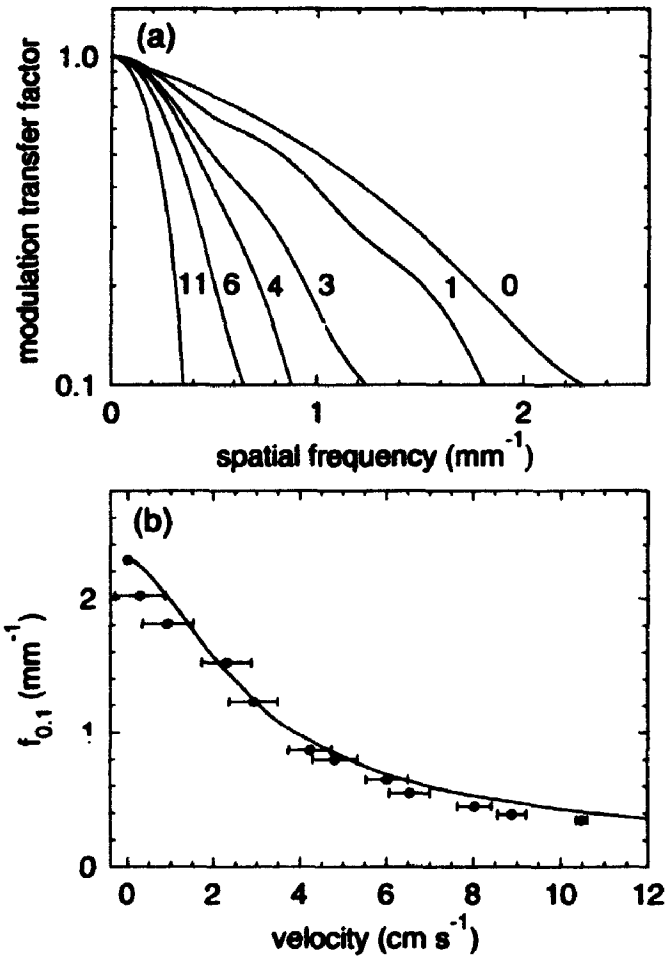

Figure 3.8: (a) $MTF_{vel}(f,v)$ derived from the images in Fig. 3.7 for different velocities. (b) Limiting resolution versus velocity. The solid line is calculated using Eq. 3.5.

3.6.3 Linearity and precision

Figure 3.9 shows the linear relationship between CT number and mean attenuation coefficient, for $\bar{\mu}$ ranging between 0 and 1.5 cm^{-1}. The average accuracy in the measured attenuation coefficients (calculated as the

rms difference between the measured and true attenuation coefficients) was 0.02 cm^{-1}, which is equivalent to an average percentage error of 5%.

Figure 3.10(a) is a plot of the precision in attenuation measurement as a function of x-ray tube current. The solid line through the data is calculated from the theoretical expression in Eq. 3.6. For these experiments $\frac{\bar{N}}{J}$ = 1290, Δx= 0.015 cm, and n_{ang}= 196. In using Eq. 3.6, the equivalent detector aperture was calculated from Eq. 3.8. For the radiographic parameters used in these experiments and assuming typical values for the components of the XRII,[4,29] the quantum detector efficiency η was calculated to be 0.41. Equation 3.6 was fitted to the data in Fig. 3.10(a) and the

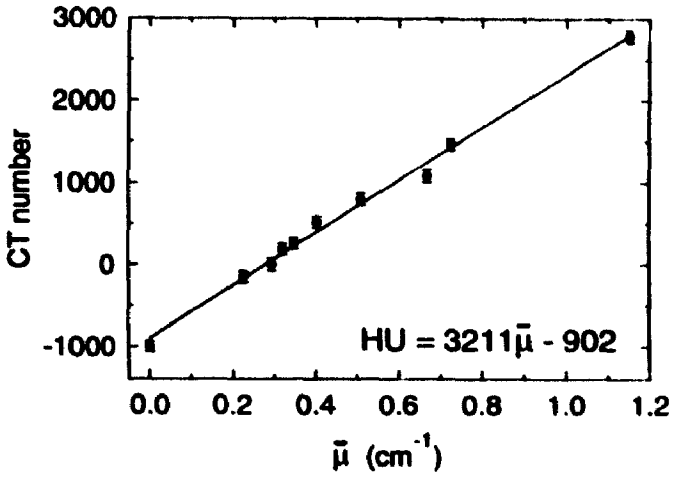

Figure 3.9: Measured CT number versus calculated μ. The line is a linear regression.

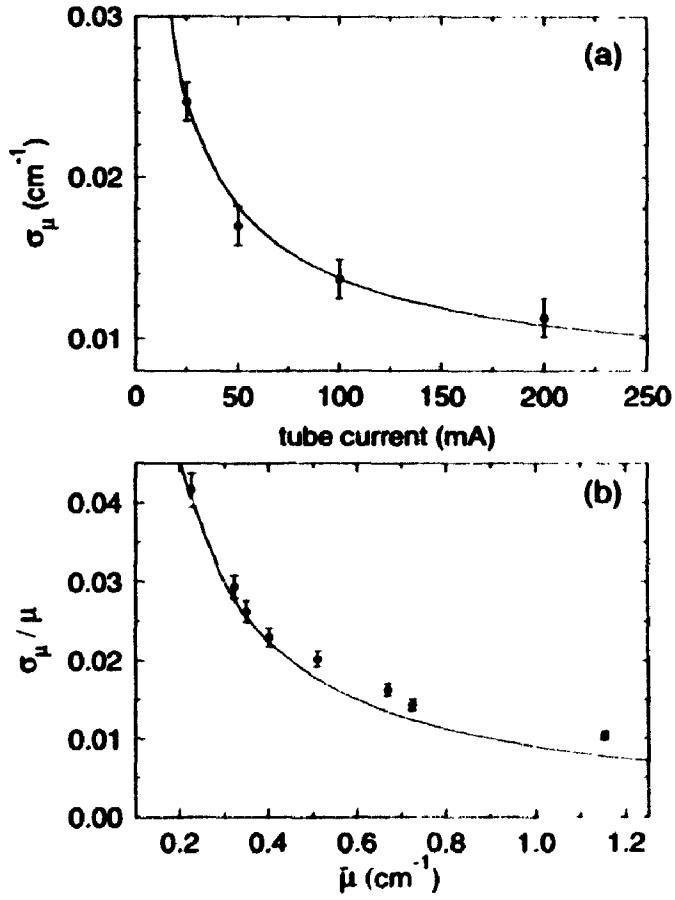

Figure 3.10: (a) Standard deviation in μ versus tube current. The solid line was calculated using Eq. 3.6. (b) Fractional precision in μ versus attenuation coefficient.

best fit to the theoretical expression was obtained with $\sigma_{sys} = 0.007 cm^{-1}$. The fractional precision in the measured attenuation coefficients is plotted in Fig. 3.10(b) as a function of mean attenuation coefficient.

3.6.4 Geometrical accuracy

Figure 3.11(a) shows the relationship between the measured and true circumferences of the cylinders in the phantom that was used to characterise the geometrical accuracy and precision. The residual error, calculated by subtracting the line of best fit from the data in Fig. 3.11(a), is plotted in Fig. 3.11(b). The mean accuracy in the circumference measurements was ±0.3 mm and the average precision, based on ten separate measurements, was ±0.2 mm.

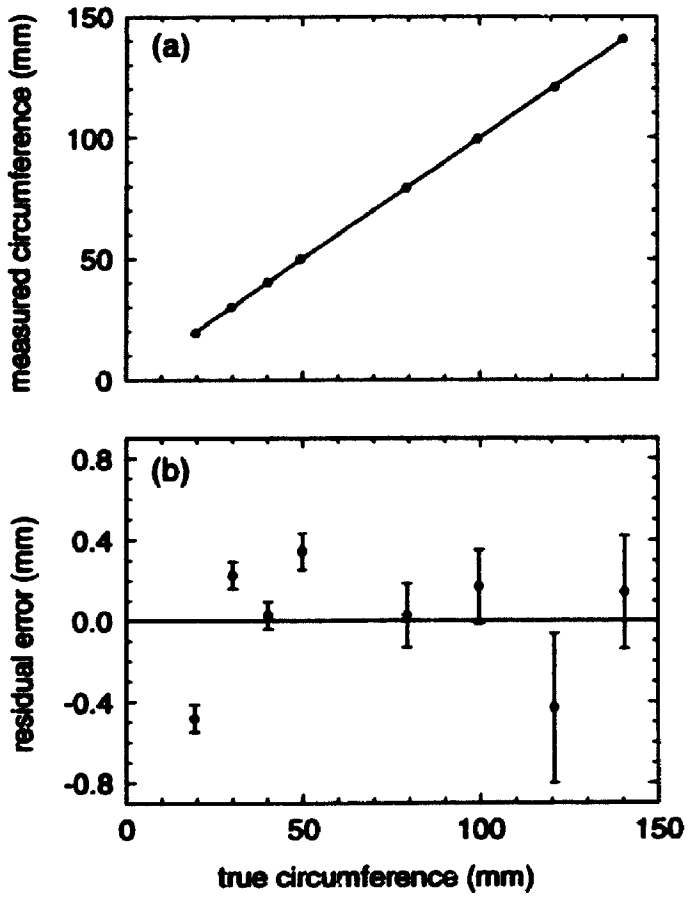

Figure 3.11: The scanner's geometrical accuracy and precision are illustrated. (a) Measured versus true circumference. (b) Residual error calculated from the measured circumferences and the linear regression in (a).

3.7 Discussion and Conclusions

The method of operation and the performance characteristics of a laboratory dynamic CT scanner have been presented. Our results show that the spatial resolution is limited by the XRII and there is good agreement between the measured $MTF_{CT}(f)$ and that predicted theoretically from the measurement of

$MTF_{sys}(f)$. Since the resolution of the scanner is limited by the XRII, further improvements can be achieved by implementing the variable electro-optical zooming modification on a newer XRII, which has higher resolution at its largest field-of-view. Furthermore, greater radiographic magnification would be possible if a tube with a smaller focal spot were used, thereby further improving the resolution in the CT images.

The scanner's temporal response has also been characterized, demonstrating that spatial resolution degradation is observed in the direction of motion (see Figs. 3.7 and 3.8). To minimize the resolution degradation due to object motion, the PDA could be read out at a higher rate, provided that sufficient photon flux is available to produce low-noise projection radiographs. The read-out rate can be increased to 300 scan lines per second, leading to an exposure time $\Delta t = 3.3 ms$. One concern may be that the blurring of moving objects due to the persistence of the XRII input and output phosphors may degrade the *MTF* further. However, the dominant component of this lag, which is primarily due to the output phosphor, can be described by exponential decay with a time constant that is much less than 1 ms.[30] Thus, the additional degradation due to XRII temporal lag is insignificant even at the high read-out rates. A plot of the theoretically-predicted limiting resolution ($f_{0.1}$) as a function of object velocity is show in Fig. 3.12 for

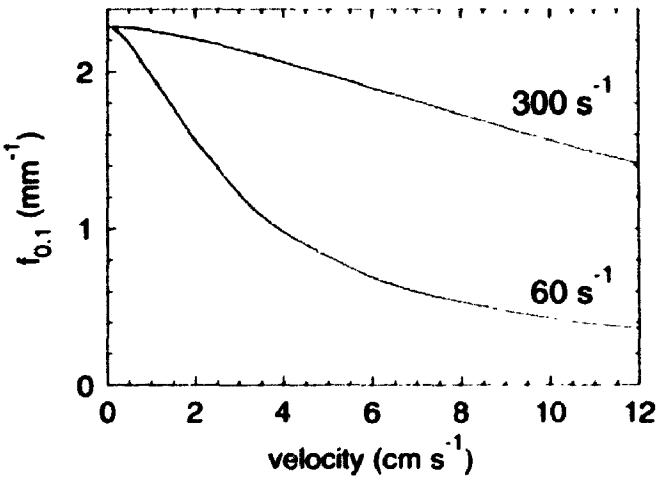

Figure 3.12: The limiting resolution at the smallest *FOV* is plotted for two read-out rates of the PDA. The curves were calculated from Eq. 3.5 and the measured $MTF_{CT}(f)$.

two PDA read-out rates. Figure 3.12 shows that the decrease in $f_{0.1}$ for objects moving at v = 3 cm s^{-1} would be diminished only by a 6% when the read-out rate is set to 300 s^{-1}, compared to the 40% decrease for a read-out rate of 60 s^{-1}. However, for applications where the maximum velocity does not exceed 1 cm s^{-1}, such as pulsating arterial samples, the 9% degradation in $f_{0.1}$, observed at v = 1 cm s^{-1} for the 60-Hz read-out rate, is acceptable.

With this CT scanner, mean attenuation coefficient can be measured accurately (to ±5%) in biological materials, including bone. The precision of the measurements is limited by system-dependent noise to 0.007 cm^{-1} (23 HU). As well as being able to obtain accurate measurements of attenuation coefficient, the scanner can also provide accurate geometrical measurements. Accurate geometrical measurements are important for the characterization of the dynamic properties of the object that is being imaged (e.g. the elasticity of an arterial sample, as discussed in chapters four and six).

Since the total scan time is directly proportional to the number of views acquired, the minimum number should be collected. Currently, the total scan time is limited by the period T of the motion cycle, the heat-loading characteristics of the x-ray tube and by the time required to transfer and save the data. In the ideal case, where the x-ray source has infinite heat capacity and the transfer and storage times are equal to zero, the scan time will be limited only by the cycle period, resulting in a total scan time of: $2Tn_{ang}$ (if, at the end of each cycle, time is allotted for the rotation of the stage to the next β); or Tn_{ang}, (if data is not collected over a small portion at the end of the cycle and the stage is rotated during that time). For arterial-specimen imaging this scan time can be reduced by as much as a factor of five, if an x-ray tube with higher heat capacity were available. For example, in an experiment where the cardiac cycle is 1-s long and

data is transferred directly to random-access memory, a time-evolved projection can be acquired every second cycle, leading to a total scan time of 3.3 min for n_{ang} = 100. For instance, in an experiment where a sample is imaged in a 2.5-cm water bath, with radiographic parameters of 80 kVp and 100 mA over a 1-s period per time-evolved projection, an x-ray tube with an anode capacity of 10^6 heat units would be required, if the x-rays are on only during the data acquisition (1.65 s). This demand on the tube's heat capacity can be reduced by a factor of two if the sample is imaged in air and the tube current is decreased to 50 mA.

In this chapter, I have demonstrated that a dynamic CT scanner based on the gated acquisition of time-evolved projections can be built for the *in vitro* imaging of objects undergoing periodic motion. The performance characteristics of the scanner in "static" mode are comparable to those reported by Holdsworth *et al.*[26] for the XRII-based volume CT scanner, which uses a time-delay integration charge-coupled detector. The temporal response of the dynamic scanner reported here is superior to that of clinically available scanners[2] and is adequate for imaging excised arterial specimens, undergoing physiologically-relevant periodic motion.

APPENDIX 3.1

Here we derive the expressions for the mean velocity $\bar{v}(t)$ and standard deviation $\sigma_v(t)$ of the velocity measured in our system in which the object moves in sinusoidal fashion. Consider an object moving with velocity

$$v(t) = A\sin(\omega t), \tag{A3.1}$$

where A is the amplitude and ω is the frequency of oscillation.

The probability density function for a sinusoid with random initial phase is[31]

$$f(V) = \frac{1}{\pi A[1-(V/A)^2]^{1/2}}. \tag{A3.2}$$

The mean velocity over the exposure time $t_0 - \frac{\Delta t}{2} < t \leq t_0 + \frac{\Delta t}{2}$ is given by the first moment of $f(V)$

$$\bar{v}(t_0) = \langle v \rangle = \frac{\int_{v_{t_0}}^{v_{t_0+\Delta t}} V\, f(V)\, dV}{\int_{v_{t_0}}^{v_{t_0+\Delta t}} f(V)\, dV}. \tag{A3.3}$$

Substituting the expression for $f(V)$ and evaluating the integrals we obtain

$$\bar{v}(t_0) = -\frac{A}{\omega t}\left[\cos(\omega t - \omega \Delta t) - \cos(\omega t)\right]. \tag{A3.4}$$

The standard deviation is given by

$$\sigma_v(t_0) = \left(\langle v^2 \rangle + \langle v \rangle^2\right)^{1/2}, \tag{A3.5}$$

where

$$\langle v^2 \rangle = \frac{\int_{v_{t_0}}^{v_{t_0+\Delta t}} V^2 \, f(V) \, dV}{\int_{v_{t_0}}^{v_{t_0+\Delta t}} f(V) \, dV} \qquad \text{(A3.6)}$$

$$= \frac{A^2}{2} + \frac{A^2}{4\omega\Delta t}\left[\sin(2\omega(t+\Delta t)) - \sin(2\omega t)\right] .$$

The standard deviation in v can thus be determined by substituting Eq. A3.4 and Eq. A3.6 into Eq. A3.5.

REFERENCES:

1. R.A. Robb, J.F. Greenleaf, E.L. Ritman, S.A. Johnson, J.D. Sjostrand, G.T. Herman and E.H. Wood, "Three-dimensional visualization of the intact thorax and contents: A technique for cross-sectional reconstruction from multiplanar x-ray views," Comp. Biomed. Res. **7**, 395-419 (1974).

2. D.P. Boyd, R.G. Gould, J.R. Quinn, R. Sparka, J.H. Stanley, and W.B. Herrmannsfeldt, "A proposed dynamic cardiac 3-D densitometer for early detection and evaluation of heart disease," IEEE Trans. Nuc. Sci. **NS-26**, 2724-2727 (1979).

3. B. Lantz, B. Lindberg, and J. Huebel, "Three-dimensional video reconstruction in fluoroscopy by means of a television system with high temporal resolution," in *Reconstruction Tomography in Diagnostic Radiology and Nuclear Medicine*, M.M. Ter-pogossian *et al.* eds., (University Park Press, Baltimore, 1977, pp. 483-499).

4. D. W. Holdsworth, M. Drangova, and A. Fenster, "A high-resolution XRII-based volume CT scanner," Med. Phys. **20**, 449-462 (1993).

5. S. Webb, J. Sutcliffe, L. Burkinshaw and A. Horsman, "Tomographic reconstruction from experimentally obtained cone-beam projections," IEEE Trans. Med. Imaging **MI-6**, 67-73 (1987).

6. E.J. Morton, S. Webb, J.E. Bateman, L.J. Clarke and C.G. Shelton, "Three-dimensional x-ray microtomography for medical and biological applications," Phys. Med. Biol. **35**, 805-820 (1990).

7. L.E. Feldkamp, S.A. Goldstein, A.M. Parfitt, G. Jesion and M. Kleerekoper, "The direct examination of three-dimensional bone architecture *in vitro* by computed tomography," J. of Bone and Min. Res. **4**, 3-11 (1989).

8. I.A Cunningham and A. Fenster, "A photodiode array x-ray imaging system for digital angiography," Med. Phys. **11**, 303-310 (1984).

9. M. Drangova, D.W. Holdsworth, P.A. Picot, K. Schulenburg, and A. Fenster, "A modified x-ray image intensifier with continuously variable field of view: resolution considerations," submitted for publication , Med. Phys.

10. J.M. Boone, J.A. Seibert, W.A. Barrett and E.A. Blood, "Analysis and correction of imperfections in the image intensifier-TV-digitizer imaging chain," Med. Phys. **18**, 236-242 (1991).

11. R.H. Huesman, G.T. Gullberg, W.L. Greenberg and T.F. Budinger, "Donner algorithms for reconstruction tomography," Pub. **214,** Lawrence Berkeley Laboratory, University of California (1977).

12. G.T. Herman, A.V. Lakshminarayanan and A. Naparstek, "Convolution reconstruction techniques for divergent beams," Comput. Biol. Med. **6,** 259-271 (1976).

13. L.A. Shepp and B.F. Logan, "The Fourier reconstruction of a head section," IEEE Trans. Nucl. Sci. **NS-21,** 21-43 (1974).

14. G.T. Barnes M.V. Yester and M.A. King, "Optimizing computed tomography (CT) scanner geometry," Proc. SPIE **173,** 225-236 (1979).

15. M.V. Yester and G.T. Barnes, "The geometrical limitations of CT scanner resolution," Proc. SPIE **127,** 296-303 (1977).

16. B.E. Oppenheim, "Reconstruction tomography from incomplete projections," in *Reconstruction Tomography in Diagnostic Radiology and Nuclear Medicine,* M.M. Ter-pogossian *et al.* eds., (University Park Press, Baltimore, 1977, pp. 155-183).

17. G.H. Glover and R.L. Eisner, "Theoretical resolution of computed tomography systems," J. of Compt. Ass. Tomo. **3,** 85-91 (1979).

18. D. Wulich and N.S. Kopeika, "Image resolution limits resulting from mechanical vibrations," Opt. Eng. **26,** 529-533 (1987).

19. R.A. Brooks and G. Di Chiro, "Statistical limitations in x-ray reconstructive tomography," Med. Phys. **3,** 237-240 (1976).

20. J.C. Gore and P.S. Tofts, "Statistical limitations in computed tomography," Phys. Med. Biol. **23,** 1176-1182 (1978).

21. D.L. Parker, J.L. Couch, K.R. Peschmann, V. Smith, M. Jimbo and E.C. Wang, "Design constraints in computed tomography: A theoretical review," Med. Phys. **9,** 531-539 (1982).

22. K. Faulkner and B.M. Moores, "Noise and contrast detection in computed tomography images," Phys. Med. Biol. **29,** 329-339 (1984).

23. Robert F. Wagner, "Toward a unified view of radiological imaging systems. Part II: Noisy images," Med. Phys. **4,** 279-296 (1977).

24. R.F. Wagner and D.G. Brown, "Unified SNR analysis of medical imaging systems," Phys. Med. Biol. **30,** p. 497 (1985).

25. P.F. Judy, "The line spread function and modulation transfer function of a computed tomographic scanner," Med. Phys. **3,** 233-236 (1976).

26. D.W. Holdsworth, R.K. Gerson and A. Fenster, "A time-delay integration charge-coupled device camera for slot-scanned digital radiography," Med. Phys. **17,** 876-886 (1990).

27. D.M. Tucker, G.T. Barnes and D.P. Chakraborty, "Semiempirical model for generating tungsten target x-ray spectra," Med. Phys. **18,** 211-218 (1991).

28. W.K. Pratt, *Digital Image Processing,* (John Wiley & Sons, New York, 1991, pp. 606-626).

29. J.A. Rowlands and K.W. Taylor, "Absorption and noise in cesium iodide x-ray image intensifiers," Med. Phys. **10,** 786-795 (1983).

30. R.K. Swank, "Measurement of absorption and noise in an x-ray image intensifier," J. Appl. Phys. **45,** 3673-3678 (1974).

31. J.S. Bendat and A.G. Piersol, *Random data: analysis and measurement procedures,* (John Wiley and Sons, New York, 1986, p. 53).

4. MEASURING THE STATIC ELASTIC PROPERTIES OF VASCULAR SAMPLES

4.1 INTRODUCTION

Due to their degenerative nature, vascular diseases, including atherosclerosis, are frequently associated with changes in the mechanical properties of the arterial wall. These are usually due to local changes in the composition of the arterial wall, such as the deposition of calcified material, reduction in elastin content or fibrous plaque formation. Thus, quantitative evaluation and comparison of the mechanical properties and composition of healthy and diseased vessels will contribute to an improved understanding of the initiation and progression of atherosclerosis.[1] Numerous studies of the elastic properties of vessels have been performed,[2] yet most involve the sectioning of the sample into strips[1,3] or have provided only average measurements over the entire specimen volume.[4,5,6] To the best of our knowledge, no previous *in vitro* investigation of the mechanical properties of arteries has provided cross-sectional information in an intact arterial sample. In this chapter I report on the first non-destructive measurements of the local static mechanical properties of an intact aortic specimen using a new computed tomography (CT) technique. The technique has allowed us to compare the modulus of elasticity of the healthy and diseased regions within a single intact vessel and, subsequently, to perform complete quantitative histological analysis of the same regions.

In this chapter I describe the application of a high-resolution volume CT[7,8] scanner to *in vitro* measurements of the mechanical properties and geometry of intact human arteries. These measurements, coupled with histological analysis, can be used to improve our knowledge of the mechanisms of vascular disease. We have used this technique to measure the elastic properties of an intact abdominal aortic aneurysm. Recent investigations into the formation of abdominal aortic aneurysms suggest an increased elastase activity, leading to a reduction of the amount of elastin

in the media of the aneurysm wall.[6,9,10,11,12,13] A decrease in elastin content would lead to a stiffening of the vessel wall.[14] By using the CT scanner to measure the local elastic properties of the normal and diseased sections of this single specimen and subsequently performing quantitative histological analysis of the same areas, a direct correlation of changes in mechanical properties and variations in wall composition is possible.

Chapter four constitutes the body of a paper entitled "Elasticity and geometry measurements of vascular specimens using a high-resolution laboratory CT scanner," which has been published in Physiological Measurement (**14**, 1993). D.W. Holdsworth was involved in the data acquisition and reconstruction. C.J. Boyd assisted in the data acquisition and the analysis of the errors in the elastic modulus. P.J. Dunmore and Dr. M.R. Roach helped with the sample preparation and histological studies.

4.2 THEORY

4.2.1 Incremental circumferential modulus of elasticity

The elastic properties of arterial specimens are frequently quantified by evaluating the slope of the stress-strain curve - the modulus of elasticity. The non-linear elastic behaviour of arterial walls[14] requires the use of an incremental, or tangential, modulus of elasticity. In the past, researchers have frequently used an expression of the following form for the incremental circumferential Young's modulus of elasticity:[15]

$$E_{inc} = 2\,(1-\sigma^2)\,\frac{dp}{dc_o}\,\frac{c_i^2 c_o}{c_o^2 - c_i^2}\quad , \tag{4.1}$$

where p is the transmural pressure, σ is Poisson's ratio, and c_i and c_o are the inner and outer circumferences respectively. Most previous techniques[4,16] have been limited to measurements of only a single diameter for elasticity calculations, whereas the cross-sectional CT images obtained in this investigation provide circumferential measurements directly. These measurements of inner and outer arterial circumference result in higher accuracy in the determination of circumferential strain, in part because the exact center of the vessel need not be known. Circumference measurements from cross-sectional images also allow the determination of strain at very low pressures, including zero pressure, when the vessel shape may not be circular and the diameter is not well defined. Although very low pressures are not normally observed *in vivo*, stress-strain measurements at low pressures provide information about the non-linear elasticity of arteries in the regime where compliance is determined largely by elastin content.[14] Equation 4.1 has been derived for a cylindrical specimen with the assumptions that the vessel wall is: (1) circular; (2) relatively thin, *i.e.*, the midwall-radius to thickness is greater than about five; (3) homogeneous and isotropic; and (4) incompressible, in the simplifying case where σ=0.5. These assumptions have been made in most calculations of the elastic

moduli of biological tissues and their validity, when applied to arterial specimens, is discussed in detail elsewhere.[17] In this study, the cross-sectional CT images obtained through the specimen provide an unique ability to estimate the validity of these assumptions for this specimen.

4.2.7 Circumference-pressure fits

When the slope of the circumference-pressure curve approaches zero, *i.e.*, for very stiff samples, discrete evaluation of $\frac{dp}{dc_o}$, in Eq. 4.1, becomes susceptible to small fluctuations in the data. Fitting the data to a smooth function overcomes this problem and also allows the continuous evaluation of E_{inc} over the pressure range studied. Exponential functions have been used previously to describe the elastic behaviour of arterial specimens.[1,18] We have chosen to fit the internal and external circumference data to an exponential function of the form:

$$c = A\,[\,1 - e^{(-Kp)}\,] + B \quad , \tag{4.2}$$

where *A*, *B* and K are the fitting parameters. By using the functional form of the circumferences, obtained by fitting the data to Eq. 4.2, E_{inc} can be evaluated over a continuous range of pressures, not confined to the discrete pressures at which measurements are obtained. Circumference measurements at low transmural pressures also have a significant effect on the fitting parameters, indicating the importance of measurements at low-pressure. The uncertainty in the circumference due to the uncertainty in the fitting parameters is calculated using standard error analysis techniques.[19]

4.3 Methods

4.3.1 CT scanner description

The CT scanner used to quantify the mechanical properties of the specimen is illustrated in Fig. 4.1. This volume CT scanner is described in detail in reference ?.

Although this volume scanner was used for the elasticity measurements described in this chapter, equivalent measurements can be obtained using the scanner described in chapter three, in its static imaging mode. The benefit of using the volume CT scanner is its ability to produce three-dimensional images, which are useful in quantifying the geometry of the specimen.

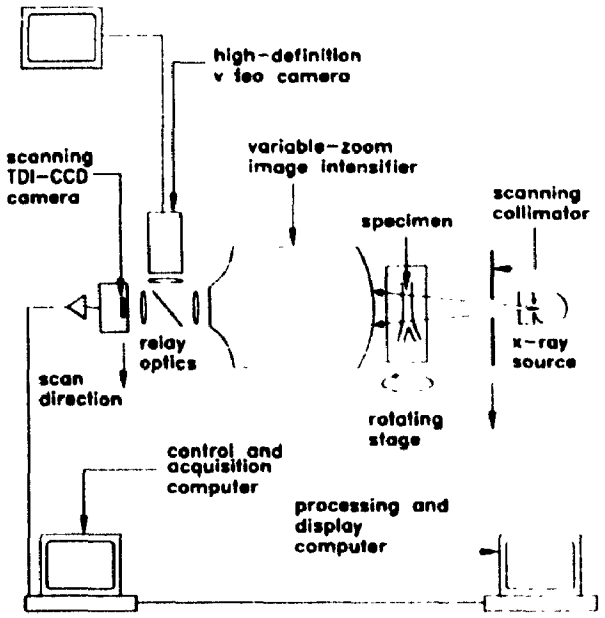

Figure 4.1: Schematic diagram of the high-resolution volume CT scanner used for the elasticity and geometry studies.

Briefly, the volume CT scanner can be operated in two modes: first, it can be used to produce fast, cross-sectional images of a single slice; and secondly, it can produce three-dimensional (volume) images. In both single-slice and volume modes the resolution of the scanner is higher than that achieved with clinical systems and is comparable to that achieved with the dynamic CT scanner described in chapter three.[8]

In fast, single-slice mode, CT images are obtained by rotating the specimen in front of the x-ray image intensifier (XRII) while collecting 400 radiographic projections of a thin slice in 4 s. The convolution-backprojection technique is then used to reconstruct the single transverse image from these projections.[20] The CT slice thickness is determined by the width of the lead collimator that is placed at the front of the XRII, and was chosen to be 0.5 mm for this experiment. Different positions along the artery can be imaged by moving the elevation stage on which the

sample holder is mounted. Since image acquisition requires only 4 s, images of fresh specimens can be obtained at several positions and at a number of pressures.

In volume mode, three-dimensional (3-D) images are obtained by acquiring 120 digital projection radiographs as the specimen is rotated through 180°. These data provide a minimum data set for the reconstruction of up to 512 cross sectional CT images. The acquisition time for a volume image is limited by the x-ray tube heat loading characteristics and currently is 90 minutes for a 512-slice volume image. The system is also equipped with a high-definition video camera attached to the output of the XRII, providing real-time fluoroscopy during the positioning of the specimen. High-resolution, low-noise digital projection radiographs of the specimen can also be acquired at any time and are valuable for the precise localization of the sections under investigation.

4.3.2 Aortic specimen preparation

The abdominal aortic sample, which we studied, was obtained at autopsy from a 60 year-old female who died of a myocardial infarction. The 37-mm diameter aneurysm, which was an incidental finding at autopsy, was located just below the renal arteries and extended to the iliac bifurcation. The enlargement appeared to be primarily on the anterior side. The average diameter of the aorta proximal to the aneurysm was 17 mm, consistent with the data reported by Horejs *et al.*[21] for normal aortas of females in this age group. Thus, we refer to the region of the aorta proximal to the aneurysm as normal. A thrombus, present in the aneurysm at the time of autopsy, washed away when the thin neointimal layer covering it ruptured during sample preparation. The presence of such thrombi is not uncommon and is frequently observed during clinical CT examinations.[22]

Following autopsy, the arterial specimen was refrigerated for 60 hours, in 0.9% saline solution at 5 °C. The delay was sufficient to ensure the inactivation of cellular

components in the arterial wall, allowing the measurement of passive mechanical properties while avoiding the effects of muscle contraction. The sample was allowed to come to equilibrium at room temperature and was subsequently mounted, at *in situ* length, on a rotating stage. The transmural pressure was provided by regulated humid air and was measured using a Cobe (Lakewood, Colorado, USA) transducer with an accuracy of ±1%. The humidity of the air was maintained at a minimum of 95% during the experiment. To reduce the effect of hysteresis, the sample was conditioned prior to the distensibility measurements by cycling the transmural pressure between 0 and 12 kPa several times over the period of 10 minutes.

4.3.3 Distensibility measurements

Transverse images of the specimen were obtained using the high-resolution CT scanner shown in Fig. 4.1. The radiographic parameters were 80 kVp with 7.7-mm aluminum filtration and 40 mA. A series of cross-sectional images were obtained at five transmural pressures ranging from 0 to 12 kPa, at the four positions shown in Fig. 4.2(a) (two of the normal aorta, N1 and N2; and two of the aneurysm, A1 and A2). To verify that stress relaxation did not alter the distensibility of the artery during the measurement period (70 minutes), the circumferences at N2 were measured at the beginning and end of the experiment.

Antero-posterior and lateral projection radiographs of the mounted, pressurized specimen were acquired prior to the distensibility measurements. These radiographs provided the locations of the CT sections relative to the subsequently acquired volume image and to anatomical landmarks such as the aorto-iliac bifurcation.

4.3.4 Circumference measurements

A computerised technique, based on data clustering methods,[23] was used to extract the arterial wall from the cross-sectional CT images automatically. Boundary tracking and chain coding techniques[23] were then used to calculate the

inner and outer circumferences. The accuracy and precision with which arterial wall circumferences can be measured, using this technique, were determined from CT images of lucite tubes, as described in chapter three, to be ±0.2 mm and ±0.1 mm, respectively.

4.3.5 Verification of assumptions made in E_{inc} calculations

To establish that the vessel has a circular cross-section the inner circumferences of the sections N1 and A2 at 2 kPa were superimposed on best-fit circles through the circumference data. The standard deviation, of the fluctuations of true arterial radius from the mean radius, for all points on the circumference was also calculated, to find the mean departures from circularity. The assumption that the vessel is thin walled was verified by calculating the midwall radius-to-thickness ratio for the four sections studied. To quantify the inhomogeneity of the wall, a cluster growing technique[23] was used to calculate the total volume of calcified tissue present in the sections studied. To verify the assumption of incompressibility, the total wall volume of the sections studied was calculated from the cross-sectional area of the arterial wall (derived from the circumference measurements) and the known image slice thickness. Finally, to verify that the mechanical properties of the specimen remained stable during the course of the experiment, the elastic modulus at N2 was calculated from circumference measurements obtained at the beginning and end of the experiment.

4.3.6 E_{inc} determination

The inner and outer circumferences of the wall at each of the four positions were measured at each pressure. The circumference measurements were fitted to the exponential function in Eq. 4.2, and the incremental circumferential modulus of elasticity was calculated based on these fits and Eq. 4.1, with σ=0.5. The error bars

of the circumference-pressure plots and of the E_{inc}-pressure plots are due to the uncertainty in the fitting parameters.

When calculating the circumferences of the aneurysm sections, the neointimal layer (see Fig. 4.2(d)) was ignored. This was justified since the pressure on both sides of this layer was the same, due to the fact that this layer was not intact. Furthermore, CT images also showed that it was not taut, and therefore, provided no retractive tension. Thus, it did not affect the elasticity measurements. The effect of thrombi on the elasticity of aneurysms has previously been discussed by Dobrin,[10] who indicates that the thrombus does not exert retractive tension.

4.3.7 Three-dimensional imaging

Upon completion of the distensibility experiment, the sample was pressure-fixed in 10% formaldehyde at 13.3 kPa while still mounted at *in situ* length. A volume image consisting of 512 cross-sectional images, each 0.225-mm thick, was acquired with the CT scanner. From this volume image, the complete geometry of the sample was quantified and "landmarks" on the specimen were defined. These landmarks were used to identify the positions of the four sections for which distensibility measurements were performed. Histological sections corresponding to the CT cross-sections in normal (N1) and aneurysmal (A2) regions were then obtained.

To provide a 3-D representation of the specimen, as it would be seen if it were cut open while under pressure, a volume rendering algorithm[24,25] was used to obtain a computer-generated image of the aneurysm, using the volume CT data.

4.3.8 Histological analysis

Following decalcification in 10% formic acid, the pressure-fixed specimen was sectioned at positions N1 and A2, which were identified with the aid of the 3-D image as described above. The 7-μm sections were subsequently stained with Movat's pentachrome to differentiate between elastin, collagen, ground substance and

muscle.[26] Stereological point counting[27] of 47 micrographs from the normal aorta and 47 from the aneurysm, was used to quantify the percent-by-volume composition of the specimen.

4.4 Results

4.4.1 Elasticity measurements

The lateral and antero-posterior digital projection radiographs of the mounted, pressurized specimen are shown in Fig. 4.2(a) and (b), where the examination sites are also indicated. Figure 4.2 also shows the cross-sectional CT images obtained at the five pressures at position N1, through the normal aorta (Fig. 4.2(c)), and

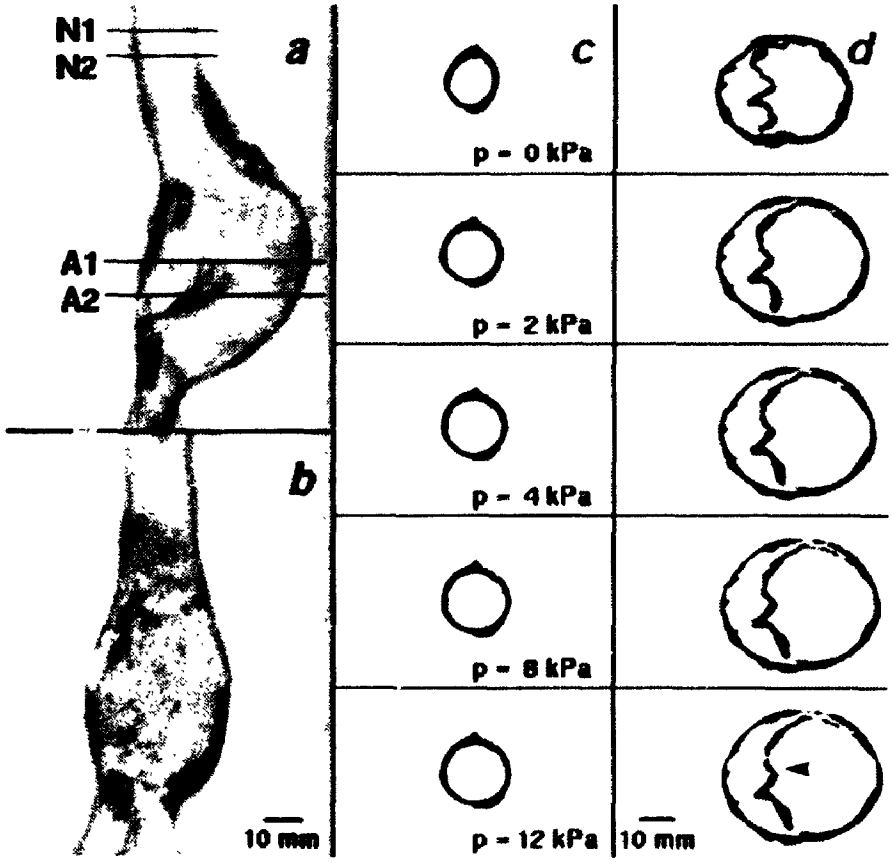

Figure 4.2: Lateral (a) and antero-posterior (b) projection radiographs of the specimen. Cross-sectional images obtained through the normal aorta at N1 (c), and the aneurysm at A2 (d). The arrow points to the neointimal thrombus covering.

position A2, through the aneurysm (Fig. 4.2(d)). The circumferences obtained from these images are plotted in Fig. 4.3 as a function of transmural pressure. The measured data are plotted along with the results from the curves fitted to Eq. 4.2. The error bars plotted are due to the uncertainty in the fitting parameters, and are as much as ten times greater than the measurement error in the circumference data.

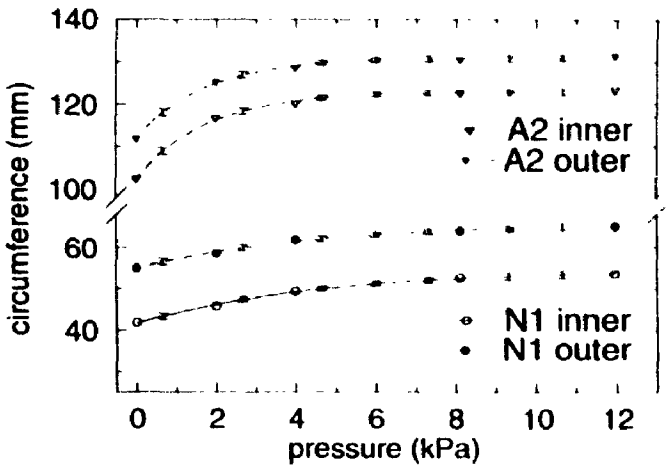

Figure 4.3: The inner and outer circumferences of the wall of the normal aorta and the aneurysm are plotted as a function of transmural pressure. The symbols represent the measured data and the lines are exponential fits.

Figure 4.4 is a semi-logarithmic plot of the incremental circumferential elastic modulus as a function of transmural pressure, for the four sections shown in Fig. 4.2(a). The error bars were calculated

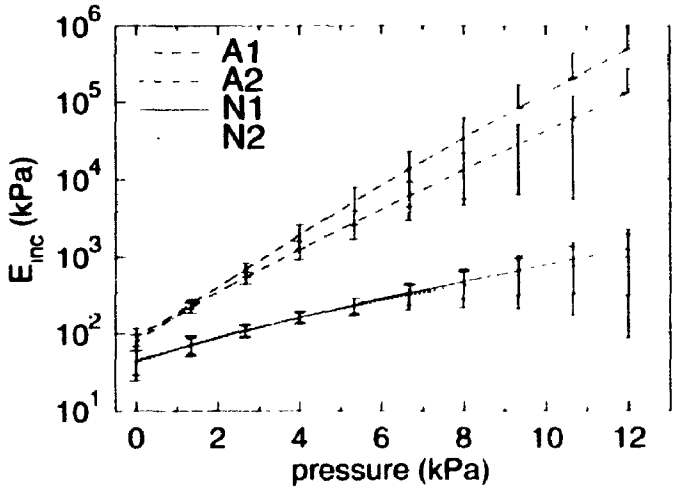

Figure 4.4: The incremental circumferential Young's modulus of elasticity (E_{inc}) is plotted against pressure on a semi-logarithmic scale for the four sections studied.

from the uncertainty due to the fitting parameters of the circumferences. At 12 kPa, E_{inc} of the aneurysm is approximately 275 times greater than that of the normal aorta proximal to the aneurysm. Confirmation that this large difference in E_{inc} reflects a real difference in the mechanical properties of the two tissues (rather than an

artifactual difference induced during the protracted data acquisition interval) was provided by measurements of E_{inc} at location N2, obtained at the beginning and end of the study. At 9 kPa, E_{inc} was 565±270 kPa at the start of the study and 820±760 kPa after 70 minutes in the humid enclosure.

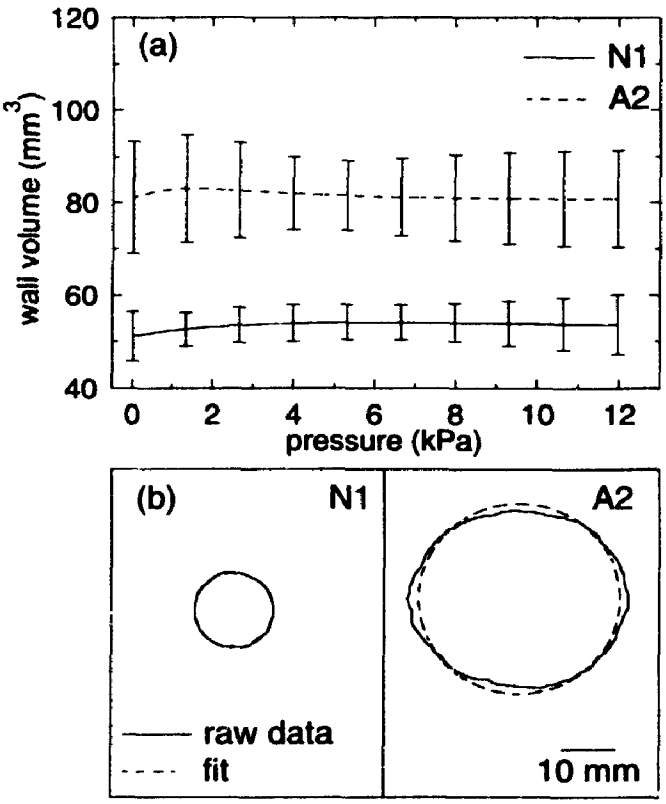

Figure 4.5: (a) The wall volume of sections N1 and A2 is plotted as a function of pressure. (b) Best-fit circles are superimposed on outlines of the inner circumferences for sections N1 and A2 at 2 kPa.

Figure 4.5(a) shows the wall volume, of the sections through the normal aorta (N1) and the aneurysm (A2), as a function of transmural pressure. For all slices studied, the wall volume remained constant to within ±9%, which is within our experimental error, and is thus consistent with the assumption of an incompressible wall. Figure 4.5(b) shows a comparison between the inner circumferences of the sections N1 and A2 at 2 kPa and best-fit circles through the circumference data. The mean departures from circularity were 1.7% for the normal aorta and 5.7% for the aneurysm. For the specimen studied, the midwall radius-to-thickness ratio was approximately 5 for the normal section and 19 for the aneurysm at 12 kPa, indicating the validity of the thin-wall assumption implicit in Eq. 4.1. The assumption that the wall was homogeneous is not strictly true, but the small calcified inclusions observed in the aneurysm wall (Fig. 4.7(a)) made up only 3.5% of the wall volume.

4.4.2 Three-dimensional geometry

Figure 4.6 shows a volume rendered image, illustrating the internal 3-D structure of the aneurysm. This view is equivalent to the view that would be obtained if the specimen were physically sectioned into two parts, while held at physiological pressure. In this image, the location of the cavity left behind by the thrombus isclearly seen. The image confirmed our assumptions that the neointimal layer covering the thrombus was not intact and that there was no pressure difference across the layer during the elasticity measurements.

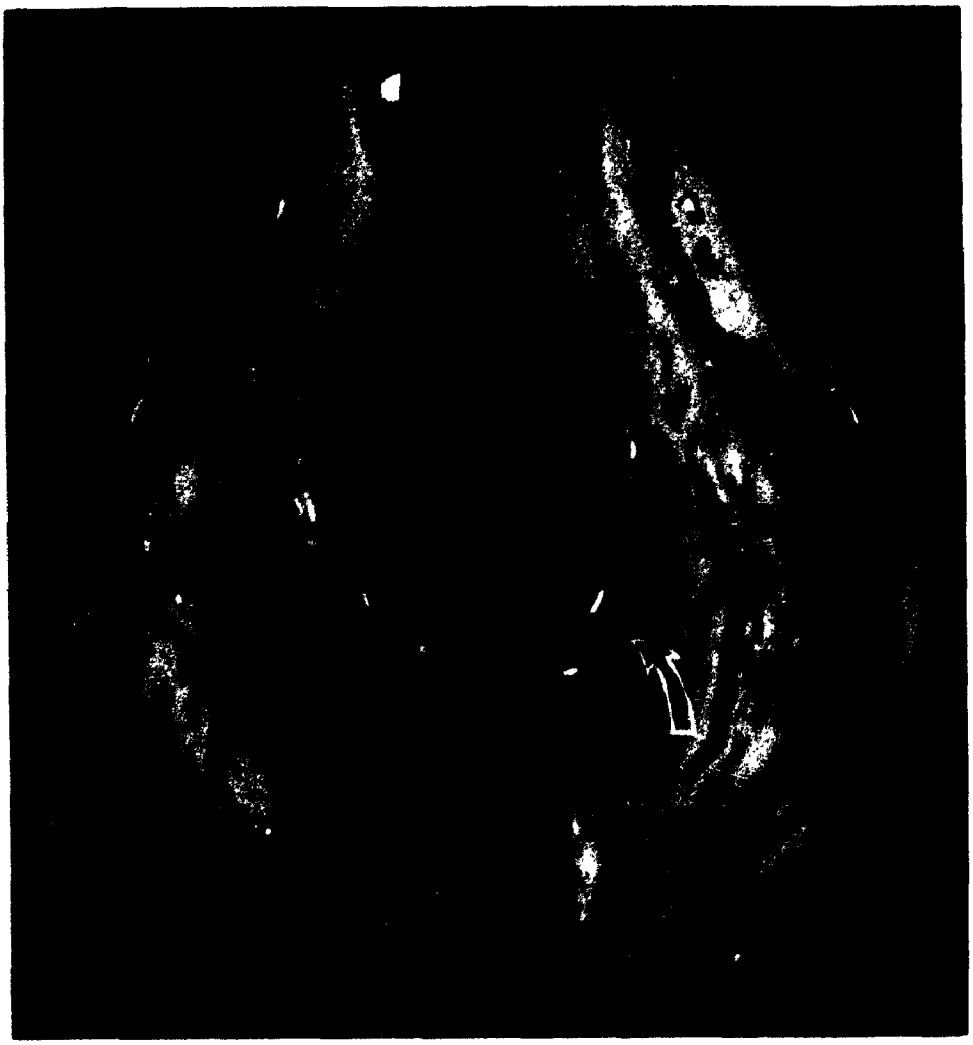

Figure 4.6: A volume rendered image of the intact sample, showing the three-dimensional nature of the aneurysm and the location of the cavity left behind by the thrombus (see arrow). Calcified plaques, located within the wall are coded in white.

4.4.3 Histology

Figure 4.7 shows a comparison between two CT sections (a) and the corresponding histological slides (b), along with magnified views of the normal aortic and aneurysm walls (Fig. 4.7(c) and (d)). Circumference measurements from the CT images and histological sections agree to within 5%. However, note that the circular shape of the vessel that was observed in the CT images is not preserved in the histological sections, due to mechanical distortions inherent in sectioning and mounting the specimen. Stereological point-counting of the stained sections yielded the average percentage composition by volume for the normal aortic media and the aneurysmal media. The results of the composition analysis are presented in table 4.1. In the aneurysm sections, the bulk of the elastin was present in the undistended (posterior) part of the wall.

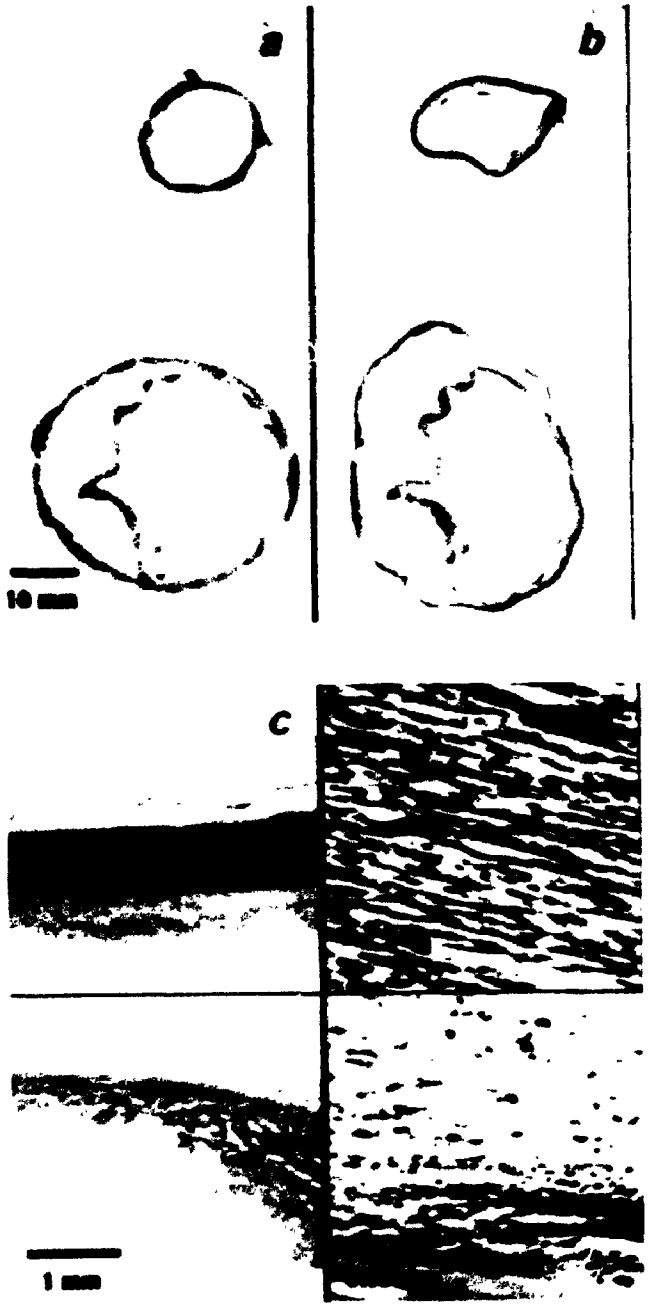

Figure 4.7: CT images (a) and the corresponding histological sections (b) through the normal (top) and aneurysm (bottom). Micrographs of wall segments from the histological sections at (c) 25 and (d) 400 times magnification.

Table 4.1: Elastin and collagen content (percent by volume) of the normal aorta and the aneurysm, as derived by stereological point counting of histological sections through N1 and A2 which were stained with Movat's pentachrome.

	Normal	Aneurysm
Elastin	36±14 %	6± 5 %
Collagen	23± 9 %	45± 9 %

4.5 Discussion and Conclusions

Previous techniques for measuring the elastic properties of vascular specimens involve approximations of either the pressure or wall thickness, or involve measurements on sectioned strips. We have developed a new technique, based on CT imaging, which provides cross-sectional images of intact vascular specimens at known static transmural pressures. Thus, we are able to calculate the true incremental circumferential modulus of elasticity of selected sections of an intact specimen. When the vessel is subsequently fixed, a 3-D (volume) image can be obtained to quantify the 3-D geometry of the specimen. The sample can then be sectioned for histological analysis and the results can be correlated with the distensibility measurements.

We have demonstrated the use of the high resolution CT scanner, built in our laboratory, for quantification of the geometry and static elastic properties of excised arteries. Due to the nigh resolution in the plane of the image (transverse cross-section) and the small slice thickness (0.2 mm), this scanner can be used to measure wall circumference of intact vessels with an accuracy better than ±0.2 mm. This high accuracy is due, in part, to our ability to control the contrast between the vessel wall and its surroundings. In clinical applications, radiographic contrast is provided by iodinated liquid contrast agents. However, these contrast agents were found to diffuse into the arterial wall over the course of an experiment. Humidified air can also

be used as a contrast medium for *in vitro* applications, providing high radiographic contrast without drying the sample during the course of the experiment. Using air as the contrast medium also results in reduced x-ray beam attenuation compared to iodinated contrast agents. Thus, higher quality images can be produced with equivalent heat loading of the x-ray tube. Comparisons of elastic modulus measurements made over an interval of 70 minutes show no significant change due to mounting tissue samples in humidified air.

We have used this system to analyze the static elasticity and geometry of an intact abdominal aorta with an aneurysm. For the elasticity studies, we used transmural pressures ranging between 0 and 12 kPa. Although this range may be considered low compared to average physiological pressures, Fig. 4.3 clearly shows that it is this range of pressures that determines the shape of the circumference-pressure curves. This range would have to be extended to higher transmural pressures when younger, more elastic arteries are being examined. Fitting the circumference-pressure data to the form of Eq. 4.2 reduces the errors in E_{inc} due to noise in the circumference measurements of stiff specimens, and reduces the number of measurement points required for the determination of the elastic modulus. Although we have chosen Eq. 4.1 to calculate E_{inc} of the specimen in this study, our imaging technique provides us with sufficient information, such as inner and outer radius, wall thickness, and composition, to analyze the elastic properties using other analytical techniques, if required. In addition, finite-element analysis techniques can also be applied for specimens which severely violate the assumptions made in applying Eq. 4.1.

The results of the elasticity studies (Fig. 4.4) show that the incremental circumferential Young's modulus of the aneurysm is as high as 3×10^5 kPa at 12 kPa, compared to 10^3 kPa for the normal aorta. Previous measurements of E_{inc} for pure

collagen[2] range between $0.3x10^6$ and $2.5x10^6$ kPa, compared with $3x10^2$ kPa for elastin,[28] suggesting that the aneurysm wall is composed primarily of collagen. The results of the histological analysis of the same regions (Fig. 4.7 and table 4.1) show that the increase in elastic modulus is indeed coupled to a decrease in elastin content in this specimen. This relationship between increased stiffness and decrease in elastin is in agreement with previous studies of distensibility variation due to reduction in elastin content.[6,14] A significant decrease in elastin content in aortic aneurysms has also been reported previously[11,12] and evidence exists[13] that the change is caused by an increase in elastase activity.

Studies on this arterial specimen provided a unique opportunity to compare normal and diseased tissues, without the necessity of accounting for inter-specimen variability, and to demonstrate the utility of our technique. Detailed analysis of a single vessel does not replace the need for the examination of a large ensemble of specimens, but allows us to draw conclusions regarding the processes that may have led to a particular disease state within an individual. Further investigations using this technique, involving arterial samples from individuals of both sexes and a range of ages, will lead to a better understanding of the development of arterial disease. Since the technique allows a paired comparison to be made between the local composition and elastic properties, fewer specimens need to be used in a study of arterial mechanical properties.

Knowledge of the 3-D geometry of an aortic specimen also provides an opportunity for modelling the flow through the specimen *in vitro*, by building anthropomorphic replicas of the vessel.[29] The measurement of the mechanical properties of the vessel being modeled could also be used in determining whether a flexible or rigid model is appropriate. For instance, the high modulus of elasticity of the aneurysm in this specimen warrants the use of a rigid, anthropomorphic flow

phantom, which could then be compared to previous studies of flow in simpler rigid flow models.[30]

The non-destructive technique presented here, for studying the static elasticity and geometry of arterial specimens *in vitro,* allows the elasticity results to be correlated with subsequent histological analysis of the same vessel. In demonstrating the use of this technique on an abdominal aortic aneurysm, we have shown that the stiffening of the wall of this aneurysm was coupled to a local decrease in the elastin content. The technique described here is limited to measurements of static properties because the imaging time (4 seconds) and the interval between images (30 seconds) are too long to provide dynamic measurements on physiologically-relevant time scales. However, the high-resolution dynamic CT scanner described in chapter three will allow the technique for measuring static elasticity presented here to be extended to *in vitro*, dynamic elasticity measurements in intact samples.

REFERENCES

1. M.H. Sherebrin, J.E. Hegney, and M.R. Roach, "Effects of age on the anisotropy of the descending human thoracic aorta determined by uniaxial tensile testing and digestion by NaOH under load," Can. J. Physiol. Pharmacol. **67**, 871-878 (1989).

2. P.B. Dobrin, "Mechanical properties of arteries," Physiol. Rev. **58**, 397-459 (1978).

3. R.B. Hickler, "Aortic and large artery stiffness: Current methodology and clinical correlations," Clin. Cardiol. **13**, 317-321 (1990).

4. B.M. Learoyd and M.G. Taylor, "Alterations with age in the viscoelastic properties of human arterial walls," Circ. Res. **18**, 278-292 (1966).

5. G.L. Papageorgiou and N.B. Jones, "Circumferential and longitudinal viscoelasticity of human iliac arterial segments *in vitro*," *J. Biomed. Eng.* **19**, 82-90 (1988).

6. D.S. Sumner, D.E. Hokanson, and D.E. Strandness, "Stress-strain characteristics and collagen-elastin content of abdominal aortic aneurysms," Surg. Gynecol. Obstet. **139**, 459-466 (1970).

7. D.W. Holdsworth, M. Drangova, K. Schulenburg, and A. Fenster, "A table-top CT system for high resolution volume imaging," Proc. Soc. Photo. Instrum. Eng. **1231**, 239-244 (1990).

8. D.W. Holdsworth, M. Drangova, and A. Fenster, "A high-resolution XRII-based quantitative volume CT scanner," Med. Phys. **20** 449-62 (1993).

9. R.W. Busuttil, H. Rinderbreicht, A. Flesher, and C. Carmack, "Elastase activity: The role of elastase in aortic aneurysm formation," J. Surg. Res. **32**, 214-217 (1982).

10. P.B. Dobrin, M.D. Baker, and C. Gley, "Elastolytic and collagenolytic studies of arteries," Arch. Surg. **119**, 405-409 (1984).

11. J.S. Campa, R.M. Greenhalgh, and J.T. Powell, "Elastin degradation in abdominal aortic aneurysms," Atherosclerosis **65**, 13-21 (1987).

12. R.J. Rizzo, W.J. McCarthy, S.N. Dixit, M.P. Lilly, V.P. Shively, W.R. Flinn, and J.S.T. Yao, "Collagen types and matrix protein content in human abdominal aortic aneurysms," J. Vasc. Surg. **10**, 365-373 (1989).

13. S. Anidjar, J.L. Salzmann, D. Gentric, P. Lagneau, J.P. Camilleri, and J.B. Michel, "Elastase-induced experimental aneurysms in rats," Circulation **82**, 973-981 (199).

14. M.R. Roach and A.C. Burton, "The reason for the shape of the distensibility curves of arteries," Can. J. Biochem. Physiol. **35**, 681-690 (1957).

15. D.H. Bergel, "The static elastic properties of the arterial wall," J. Physiol. **156**, 445-457 (1961).

16. G.J. Langewouters, K.H. Wesseling, and W.J.A. Goedhard, "The static elastic properties of 45 human thoracic and 20 abdominal aortas *in vitro* and the parameters of a new model," J. Biomechanics. **17**, 425-435 (1984).

17. D.J. Patel and R.N. Vaishnav, *Basic Hemodynamics and its Role in Disease Processes* (University Park Press, Baltimore,1980) pp. 180-196.

18. Y.C. Fung, K. Fronek, and P. Patitucci, "Pseudoelasticity of arteries and the choice of its mathematical expression," Am. J. Physiol. **237**, H620-H631 (1979).

19. P.R. Bevington, *Data reduction and error analysis for the physical sciences*, (McGraw Hill Book Company, New York, 1969) pp. 204-246.

20. R.H. Huesman, G.T. Gullberg, W.L. Greenberg, and T.F. Budinger, *Donner algorithms for reconstruction tomography* (Lawrence Berkeley Laboratory, California) 1977.

21. D. Horejs, P.M. Gilbert, S. Burstein, and R.L. Vogelzang, "Normal aortoiliac diameters by CT," J. Comput. Assist. Tomogr. **4**, 602-603 (1988).

22. D.H. Stephens, P.F. Sheedy, and R.H. Hattery, "Retroperitoneal space," in *Essentials of body computed tomography*, edited by M. Greenberg (W.B Saunders Company, Philadelphia, 1988) p. 235.

23. W.K. Pratt, *Digital Image Processing*, (John Wiley & Sons, New York, 1991) pp. 606-626.

24. D. McMillan, R. Johnson, and C. Mosher, "Volume rendering on the TAAC-1," Suntech Journal **2**, 52 (1989).

25. H.E. Cline, W.E. Lorensen, and S. Ludke, "Two algorithms for the three-dimensional reconstruction of tomograms," Med. Phys. **15**, 320-327 (1988).

26. G.C. Brown *An Introduction to Histotechnology* (Appleton-Century Crofts, New York, 1978) pp. 234-235.

27. H. Elias and D.M. Hyde *A Guide to Practical Stereology* (S. Karger A.G., New York, 1983).

28. C.G. Caro, T.J. Pedley, R.C. Schroter, and W.A. Seed, *The mechanics of the circulation* (Oxford University Press, New York, 1978) p 91.

29. R. Frayne, L.M. Gowman, D.W. Rickey, D.W. Holdsworth, P. Picot, M. Drangova, C.B. Caldwell, A. Fenster, and B.K. Rutt, "A geometrically accurate vascular phantom for comparative studies of x-ray, ultrasound and magnetic resonance vascular imaging: Construction and geometrical verification," Med. Phys. **20**, 415-425 (1993).

30. T Fukushima, T. Matsuzawa, and T. Homma, "Visualization and finite element analysis of pulsatile flow in models of the abdominal aortic aneurysm," Biorheology **26**, 109-130 (1989).

5 PUMP FOR PHYSIOLOGICAL FLOW SIMULATION

5.1 INTRODUCTION

Our ability to study the dynamic elastic properties of intact excised vascular specimens depends on our ability to reproduce physiological flow waveforms accurately and reliably. Previously, simulated pulsatile flow has been used extensively in haemodynamic investigations in arterial models with bifurcations and stenoses. Many different techniques have been used to measure flow in these models, including laser Doppler anemometry,[1] Doppler ultrasound,[2,3] magnetic resonance[4] and digital radiography.[5] Physiological pulsatile flow waveforms are also required to investigate the role of pulsatility in tissue perfusion.[6]

In all these cases the requirements of the flow source are quite demanding. The desired volume flow waveform must be generated both accurately and reproducibly. Most techniques for the investigation of time-varying flow, as well as our technique for acquiring dynamic computed-tomography images, require gated acquisition of many cardiac cycles, so cycle-to-cycle variability in the flow waveform must be small. Long-term stability is equally important. The pump must be capable of producing a wide range of flow rates in order to simulate flow in the peripheral vasculature, where peak flow rates of 30 ml s^{-1} are reported.[7] It must be easily programmed to produce a variety of pulsatile waveforms, including waveforms with flow reversal. For haemodynamic investigations, the pump must also be capable of producing continuous steady flow. It is essential that the pumping mechanism not produce gas bubbles or cavitation, since bubbles will change the hydrodynamic properties of the fluid and their presence will produce measurement artifacts. Finally, a device to simulate physiological flow should operate as an ideal flow source, capable of generating sufficient pressure to be unaffected by changes in the downstream resistance.

Many different pumps have been proposed to meet these requirements and Law *et al.* provide a thorough review of previous work.[8] Briefly, previous devices can be categorised according to their basic pump type; gear, peristaltic or piston. Gear pumps have been used[9,10,11,12] to generate pulsatile waveforms, however, a major drawback of this approach is the sensitivity to cavitation due to the action of the gears. Modified peristaltic pumps have been used[8,13] to simulate physiological flow waveforms by manipulation of the backplate or computer-control of the roller. This approach allows the production of only a limited subset of waveforms and is not well suited to the production of steady flow. It is also difficult to program new waveforms, or produce reverse flow with this technique. Cam-driven piston pumps[14,15,16] share the general disadvantage of difficulty in programming new waveforms and difficulty in producing steady flow. All the flow simulators described here have one other significant disadvantage, namely that flow monitoring must be performed to provide feedback and determine the output waveform.

A promising variation of flow simulator reported by Werneck *et al.*[17] makes use of a servo-motor-driven piston pump which acts as an ideal flow source. This approach overcomes many of the limitations of previous designs, but is not well suited to the production of uninterrupted constant flow. We have developed a variation of this design, which allows the production of physiological flow waveforms, including reverse flow, as well as steady flow for indefinite periods of time.

The material presented in chapter five is a portion of a paper entitled "Computer-controlled positive displacement pump for physiological flow simulation," which has been published in Medical and Biological Engineering and Computing (**29**, 565-570, 1991). D.W. Holdsworth invented the pump and D.W. Rickey wrote the control software. Assistance in building the device was supplied by D.J.M. Miller. I was involved in the design of the device and the characterisation of its performance.

5.2 System Description

A schematic diagram of our pump is shown in Fig. 5.1. Two rack-mounted pistons are driven in horizontally-opposed lucite cylinders (internal diameter 2.5 cm) by a computer-controlled micro-stepping motor (Compumotor Corporation, Cupertino CA). The motor produces 0.5 N·m torque at rotational speeds of up to 8 rev s^{-1}. The motor controller divides each shaft rotation into 25000 discrete microsteps. Gearing between the motor and rack is chosen so that one motor microstep results in the displacement of 0.198 µl from the pump cylinder. In the original design, each cylinder has a usable stroke volume of 180 ml. although larger or smaller volumes are possible with a minimal design change. A 4-way spool valve (Mark 7, Numatics, Highland, MI) is used to interchange the outlet and inlet paths when the piston

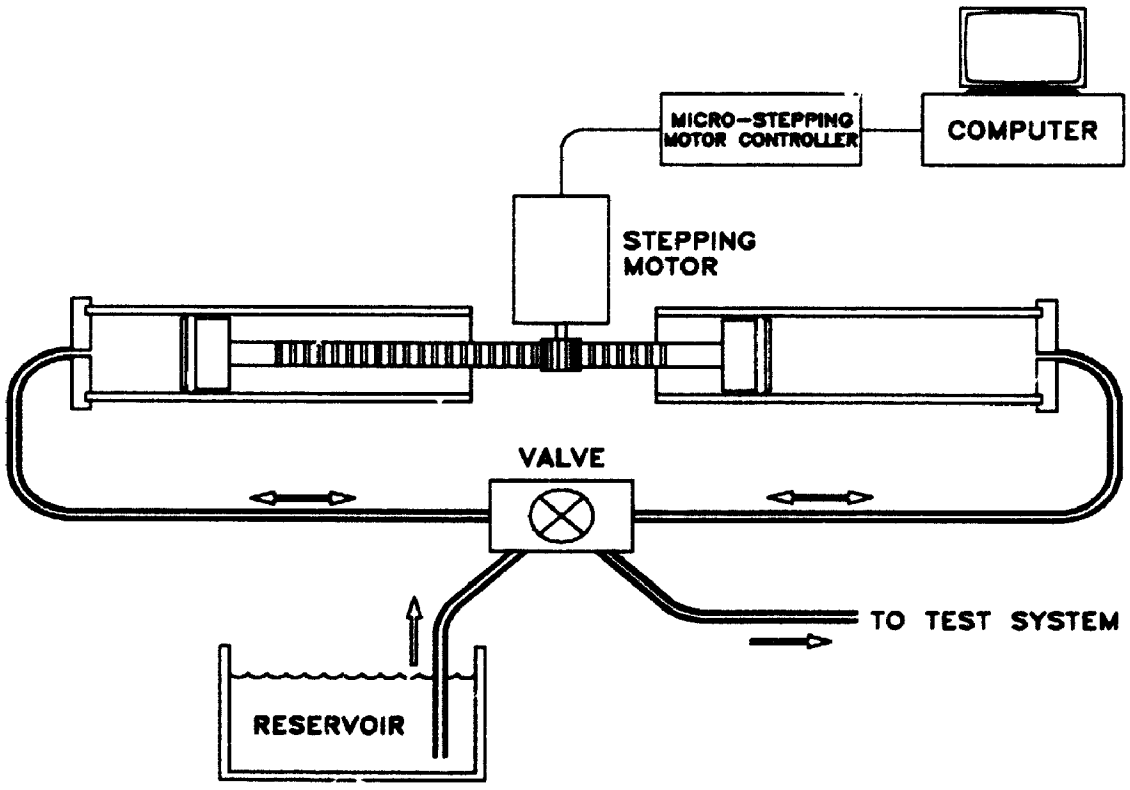

Figure 5.1: Schematic diagram of the pulsatile flow simulator.

reaches the end of its travel. This valve logic allows the pump to refill one cylinder while forcing fluid from the other, providing nearly 100% duty cycle. An active-control valve is used, rather than passive check valves, to enable reverse flow production.

The pump is controlled by a PC/AT-based motor controller (Model PC-23, Compumotor Corporation, Cupertino CA) with an on-board 68008 microprocessor. Control of the pump flow rate is achieved through the known relationship between the angular displacement of the motor shaft and the volume displaced from the pump; i.e., 0.198 μl per microstep. To program a new flow waveform, the flow rate as a function of time must first be digitised and interpolated to a known temporal interval. The motor controller produces the shaft rotation which ejects the appropriate volume of fluid in each time interval. The controller architecture allows us to choose this interval to be between 2 and 60 ms. For the present study we have chosen a 10 ms time interval. Once loaded with the waveform data, the motor controller can repeat the complete waveform a preset number of times without further instructions from the host computer. Valid waveforms are limited by the available torque of the stepper motor and the usable cylinder volume. The controller also produces the required control signals for the spool valve and generates a TTL logic pulse once each cardiac cycle, allowing gated data acquisition.

5.3 System Evaluation

5.3.1 Methods

To evaluate the performance of our pump we have used a simple test system, consisting of a 20-cm length of 6.7-mm diameter polyester tubing connected between outlet and reservoir, with an in-line electromagnetic flowmeter probe (Model 322, Carolina Medical Electronics Inc., King NC) providing flow measurement. This short length of tubing was used in most experiments since it was observed that the final shape of the output waveform depends strongly on the compliance, and hence the

length, of the test system. To investigate the effect of tube type and compliance on the output waveform, some measurements were obtained with 2 m lengths of braided polyester, latex or copper tubes in line with the EM flowmeter. The manufacturer's specifications for the flowmeter state that its response drops to -6 dB at 50 Hz. To avoid aliasing we have digitised the output signal from the flowmeter at 410 Hz, using a 12-bit analogue-to-digital converter.

To verify the flowmeter calibration and to measure the steady flow output of the pump, we used timed collection in a volumetric flask with flow rates ranging from 0.1 to 60 ml s^{-1}. For all measurements we have used a mixture of glycerol and water as the working fluid. In appropriate proportions (4 parts glycerol to 5 parts water) the viscosity of this mixture approximates that of blood.[9] The salinity of the fluid was adjusted to normal physiological levels (0.9% by weight) to ensure proper functioning of the electromagnetic flowmeter.

5.3.2 Results

We first evaluated the performance of our pump in producing steady flow. Figure 5.2 shows the results of our measurements using timed collection in a volumetric flask, comparing the observed flow rate with the programmed flow rate. Figure 5.2(a) shows the high degree of correspondence between these quantities, with linear regression of the data yielding a slope of 1.003 and an intercept of 0.022 ml s^{-1}. Figure 5.2(b) shows the residual errors obtained by subtracting the linear regression flow rates from the programmed flow rate. It is apparent that at low flow rates the error is negligible and at a flow rate of 60 ml s^{-1} the error is maximum and is less than 250 µl s^{-1}. The pump is unable to produce flow rates greater than 60 ml s^{-1} because the drive motor has insufficient torque at high rotation rates, and at flow rates less than 0.1 ml s^{-1} mechanical resonances add unwanted perturbations to the output waveform.

Although Fig. 5.2 indicates that the average volume flow from the pump is accurate, it is also necessary to characterise the steady flow output for short-term, cyclic variations. Therefore, to perform this analysis we have digitised 10 seconds of flowmeter data, collected while the pump was producing 10 ml s^{-1} steady flow. These data were then Fourier transformed, and the resulting power spectrum is shown in Fig. 5.3. This plot shows that the output power is contained nearly entirely in the zero frequency component, with negligible contributions at higher frequencies.

One other concern about the production of steady flow is the disruption of flow which occurs each time the piston reaches the end of a cylinder. This is a result of the abrupt

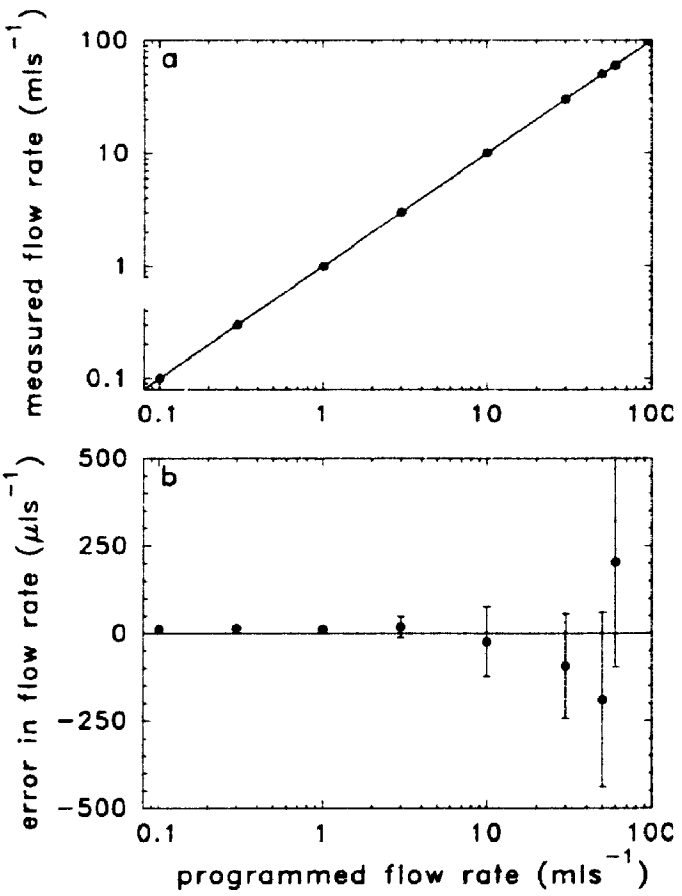

Figure 5.2: Linearity and accuracy of steady flow produced by the pump. (b) shows the residual error in flow rate when the line of best fit in (a) is subtracted from the measured flow rate.

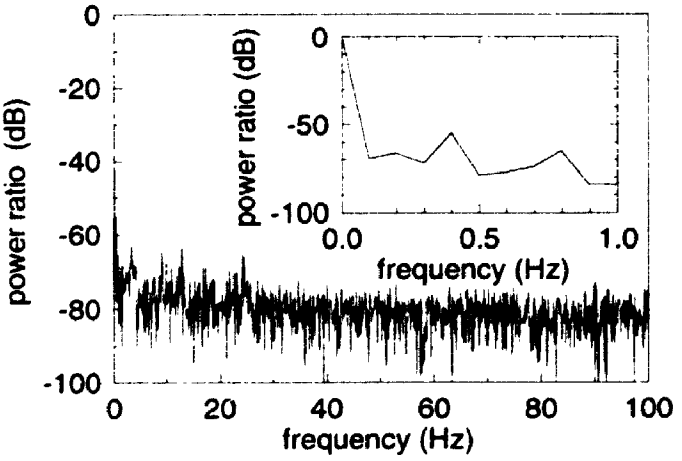

Figure 5.3: Power spectrum of 10 s of digitised flowmeter measurements. The inset shows the data between 0 and 1 Hz, plotted on an expanded scale to illustrate the drop in power between zero frequency and 0.1 Hz.

reversal of piston direction coupled with a valve switch. We have observed that the spool valve controlling the inlet and outlet paths changes state within 40 ms, so it might be expected that the flow disruption would be of similar length. However, distensibility in the test system results in ringing which lasts considerably longer. Figure 5.4 shows flowmeter data collected during a piston reversal using 2 m lengths of polyester (Fig. 5.4(a)), latex (Fig. 5.4(b)) and copper (Fig. 5.4(c)) tubes. The minimum ringing time of about 400 ms was obtained with polyester tubing. Clearly, the duration and shape of the flow disruption depend strongly on the materials used in the driven hydraulic system, with a minimum interval of about 400 ms required to return to steady flow after a piston reversal.

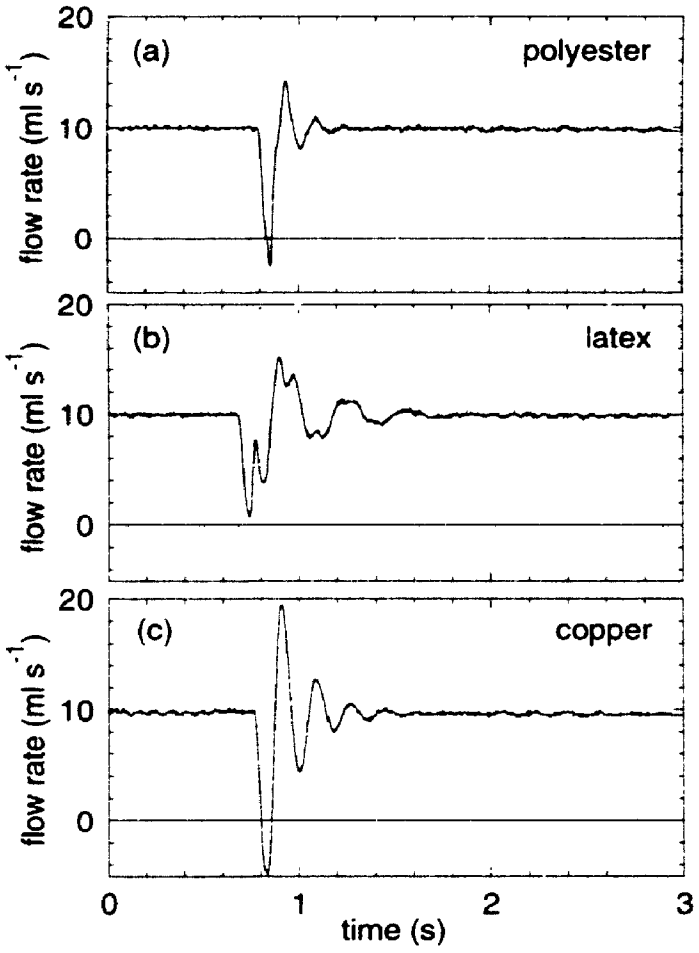

Figure 5.4: Flowmeter measurements of the flow disruption which occurs after valve switching and piston reversal. Measurements were made while pumping through 2 m of (a) polyester, (b) latex, and (c) copper tubing.

While the production of steady flow is an essential feature of flow simulation, steady flow alone is not sufficient for *in vitro* studies of vascular haemodynamics. Therefore, we have evaluated the capabilities of our pump to produce time-varying flow waveforms, such as sinusoids and physiological waveforms. Figure 5.5(a) is a plot of data obtained with a flowmeter when the pump was programmed to produce

a 5-Hz sine wave with an amplitude of 10 ml s^{-1}, using a 20-cm length of polyester tubing on the pump outlet. These data were Fourier transformed to obtain the power spectrum plotted in Fig. 5.5(b), where we observe that the power is mainly at the programmed frequency, with less than 0.3% of the total power contained in harmonics at 10 and 15 Hz. To investigate the frequency response of the pump we have collected flow waveforms during the production of sine waves ranging in frequency from 1 to 30 Hz, with an amplitude of 20 ml s^{-1}. For these tests the impedance of the outlet hose and flowmeter probe (diameter 3.2 mm) provided a suitable load, such that steady flow of 10 ml s^{-1} resulted in a gauge pressure of 22.5 kPa at the pump outlet. The Fourier transform of these sinusoidal waveforms provided frequency domain spectra similar to that shown in Fig. 5.5(b), and from these plots it was possible to determine the observed flow amplitude within a 1.2-Hz bandwidth about the fundamental frequency. The amplitude ratio was calculated as the ratio of the observed flow amplitude to the requested flow amplitude, and in Fig. 5.5(c) we have

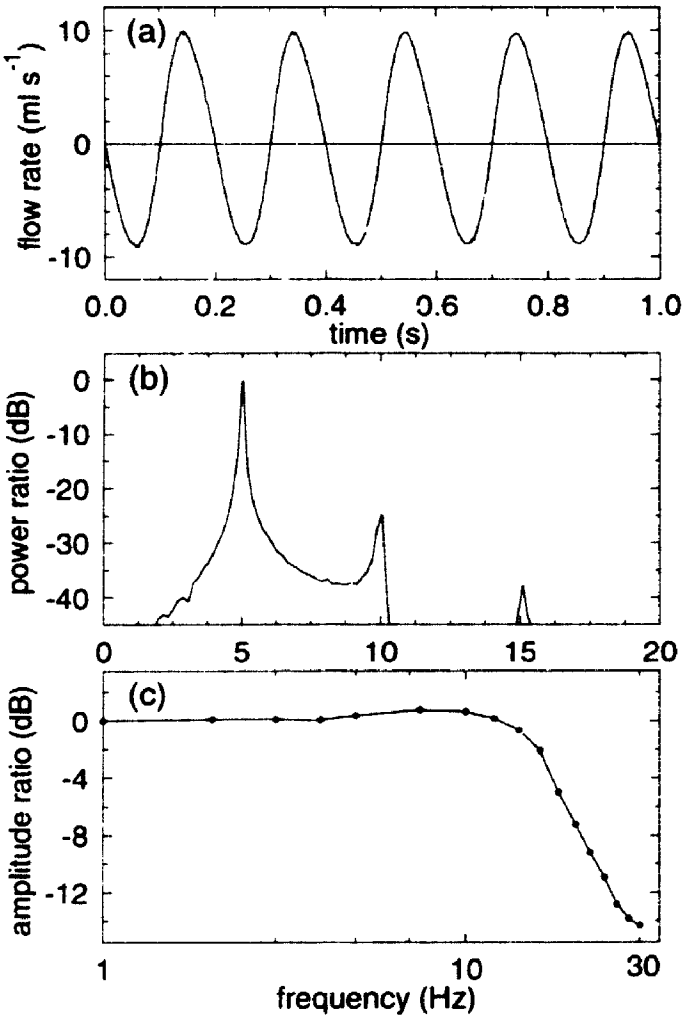

Figure 5.5: (a) Measured pump output for a programmed 5 Hz, 10 ml s^{-1} sine waveform. (b) Power spectrum of the data in (a). (c) frequency response of the pump. Error bars are smaller than the points.

plotted this amplitude ratio as a function of frequency. Figure 5.5(c) indicates a nearly flat frequency response to about 10 Hz, dropping to -6 dB at about 19 Hz. Previous *in vivo* flow studies[17,18] have shown that frequency components above 12 Hz are insignificant in the peripheral vasculature. Thus, our system can provide physiological flow waveforms without a correction[11] for diminished high frequency response.

To test the ability of the pump to reproduce physiological flow waveforms we have programmed our device with a waveform typical of the common femoral artery during rest.[7] Figure 5.6(a) shows the results of our flowmeter measurements using this waveform, with the programmed flow rate superimposed for comparison. The small discrepancy between programmed and measured flow rates is probably due to tube compliance.

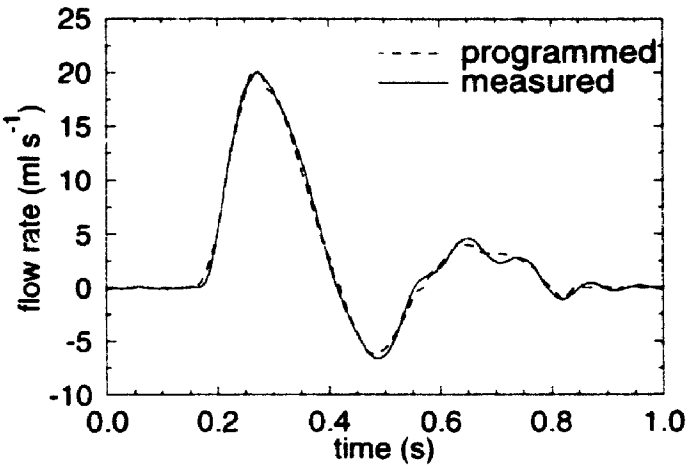

Figure 5.6: Flowmeter measurements of a simulated femoral flow waveform (solid line), compared with the programmed waveform (dotted line).

Cycle-to-cycle reproducibility was investigated by programming the pump to produce continuous cycles (60 per minute) of the common carotid flow waveform while recording the observed flow with the electromagnetic flow meter. Data acquisition was gated to start collection 0.2 seconds before peak systole and continue for a period of 0.98 seconds, over which time 512 flow-rate values were recorded. Two thousand cycles were digitally recorded over a period of 66 minutes, producing a data set consisting of 2000 flow waveforms with 1.9 ms temporal resolution. Figure 5.7 shows a superposition of these 2000 waveforms. The width

of the curve, plotted in Fig. 5.7, shows the maximum spread of flow rates observed during the 66-minute experiment, thus indicating the largest possible deviation in the flow rate waveforms. Since the figure shows only the maximum spread of flow rates, we have calculated a histogram of flow rates at each temporal point in the cycle by placing the 2000 measured values into bins of width 87 $\mu l\ s^{-1}$. For example, in Fig. 5.8(a) we show a plot of one such histogram, obtained from measurements made 0.04 seconds after initiation of data collection (position **a** in Fig. 5.7). The distribution of flow rates is centred at 5.28 $ml\ s^{-1}$, with a standard deviation of 0.07 $ml\ s^{-1}$. Figure 5.8(b) shows another distribution, obtained near peak systole (position **b** in Fig. 5.7). This histogram has a mean value of 22 $ml\ s^{-1}$ and a standard deviation of 0.13 $ml\ s^{-1}$. The average standard deviation of the 512 observed distributions is 0.1 $ml\ s^{-1}$.

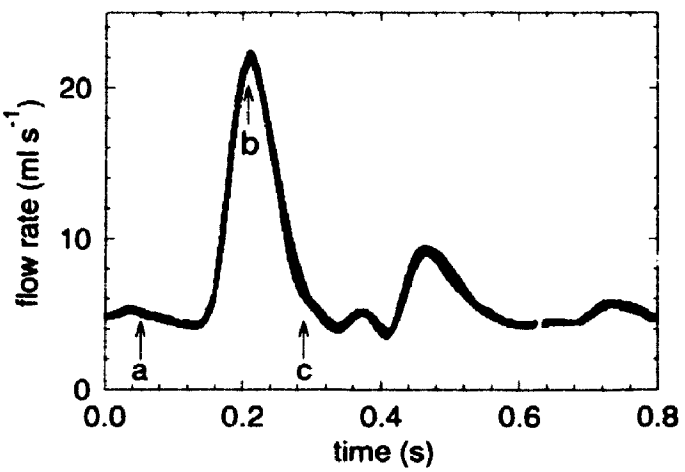

Figure 5.7: Two thousand repetitions of a common carotid waveform were acquired and superimposed. The width of the curve represents the maximum excursion of the distributions. Flow-rate histograms are displayed in Fig. 5.8 for the marked points.

At points when the carotid waveform of Fig. 5.7 exhibits a large negative slope (position **c**), the flow rate histograms are split into bimodal distributions, as shown in Fig. 5.8(c). These two distributions represent a difference in output from the two independent cylinders of the pump. This small discrepancy in output from the left and right cylinders is probably due to slight differences in compliance in the cylinder walls and associated tubing.

5.4 Discussion and Conclusions

We have shown that it is possible to produce both pulsatile and steady flow waveforms with a computer-controlled, positive-displacement pump. This pump has advantages over previous designs, such as a nearly 100% duty cycle for steady flow by virtue of the dual cylinders. When the pump is programmed to reproduce a steady volume flow rate typical of the peripheral vasculature, the time between valve switches is 12 seconds, which is long in comparison to the observed duration of the flow disruption. The 0.4 second flow disturbance is less disruptive in pulsatile wave forms, because valve switching and associated piston reversal can occur at a point of little or zero flow. Also, the controller provides a TTL signal so that this flow disruption can be excluded from data collection.

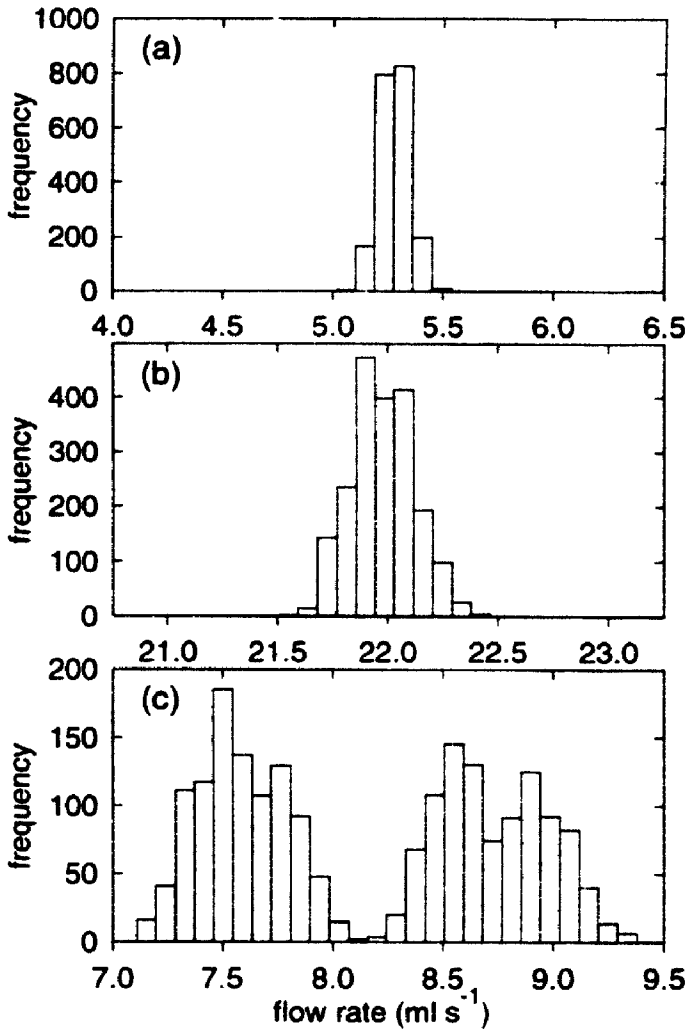

Figure 5.8: Flow rate frequency distributions, measured at the points indicated on the carotid waveform of Fig. 7. Histograms for (a) t = 0.04 s, (b) t = 0.21 s and (c) t = 0.28 s have been plotted with the same time axis scale, for comparison.

There is no requirement for continuous feedback with this pump, as the open-loop performance is observed to be extremely stable for long periods of time. The basic design of our pump is also easily modified to accommodate larger or smaller

flow rates, since maximum flow rate depends only on piston diameter and available motor torque.

Although it is possible to produce an accurate, reproducible flow waveform at the outlet of this pump, we have found that the compliance of the driven system is extremely important in determining the waveform at the actual measurement point. This fact is of particular importance when the pump is located far from the measurement point. In this case, it is important that the transfer function of the driven system be taken into account when programming the waveform to be produced at the pump outlet. We have also found that the accurate transmission of pulsatile waveforms is dependent on the proper choice of both tube compliance and downstream resistance.

Of particular importance, to the application of this pump for dynamic CT studies, is the cycle-to-cycle reproducibility. We have shown that the flow waveform is stable to within about 1% over thousands of cycles. Although this pump was not designed to maintain a physiological pressure waveform, if can be used to generate physiological pressure waveforms in excised vessels, provided the pressure is monitored and that the flow rate can be adjusted to provide the desired pressure waveform. Since the pressure depends on the flow rate and the system impedance, the pressure waveform should also be reproducible provided that the impedance does not change over time.

REFERENCES

1. D.N. Ku, and D.P. Giddens, "Laser Doppler anemometer measurements of pulsatile flow in a model carotid bifurcation," J. Biomechanics **20,** 407-421. (1987).

2. Y.I. Cho, L.H. Back, D.W. Crawford, and R.F. Cuffel, "Experimental study of pulsatile and steady flow through a smooth tube and an atherosclerotic coronary artery casting of man.," J. Biomechanics **16,** 933-946 (1983).

3. D.Y. Fei, C. Billian, and S.E. Rittgers, "Flow dynamics in a stenosed carotid bifurcation model-part 1: basic velocity measurements," Ultrasound in Med. & Biol. **14,** 21-31 (1988).

4. A.J. Evans, L.W. Hedlund, R.J. Herfkens, J.A. Utz, E.K. Fram and R.A. Blinder, "Evaluation of steady and pulsatile flow with dynamic MRI using limited flip angles and gradient refocused echoes," Magnetic Resonance Imaging **5,** 475-482 (1987).

5. I.A. Cunningham, S. Yamada, B.B. Hobbes, and A. Fenster, "Arterial flow characterization with a photodiode array based imaging system," Med. Phys. **16,** 179-187 (1989).

6. B.I. Tranmer, C.E. Gross, G.W. Kindt, and G.R Adey, "Pulsatile versus nonpulsatile blood flow in the treatment of acute cerebral ischemia," Neurosurgery **19,** 724-731 (1986).

7. C. Marquis, J.J. Meister, E. Mooser and R. Mosimann, "Quantitative pulsed Doppler measurement of common femoral artery blood flow variables during postocclusive reactive hyperemia," J. Clin. Ultrasound **14,** 165-170 (1986).

8. Y.F. Law, R.S.C. Cobbold, K.W. Johnson, and P.A.J. Bascom, "Computer-controlled pulsatile pump system for physiological flow simulation. Med. & Biol. Eng. & Comput. **25,** 590-595 (1987).

9. W.N. McDicken, "A versatile test-object for calibration of ultrasonic Doppler flow instruments," Ultrasound in Med. and Biol. **26**, 245-249 (1986).

10. P. Issartier, M. Sioffi and R. Pelissier, "Simulation of blood flow by a hydrodynamic generator," Med. Prog. Technol. **6,** 39-40 (1978).

11. J.N. Petersen, "Digitally controlled system for reproducing blood flow waveforms in vitro," Med. & Biol. Eng. & Comput. **22,** 277-280, (1980).

12. P.R. Hoskins, T. Anderson, and W.N. Mcdicken, "A computer controlled flow phantom for generation of physiological Doppler waveforms." Phys. Med. Biol. **34,** 1709-1717 (1989).

13. Y. Douville, K.W. Johnston, M. Kassam, P.Zuech, R.S.C. Cobbold, and A. Jares, "An in vitro model and its application for the study of carotid Doppler spectral broadening,' Ultrasound in Med. & Biol. **9,** 347-356 (1983).

14. T.A. Kiyose, M. Kusaba, M. Kamori, Y. Inokuchi, Y. Takamatsu, and H. Takahara, "Development of *a* pump system for experimental model simulation of blood flow in peripheral artery," Fucuota Acta Med. **68,** 86-91 (1977).

15. R. Appugliese, R. Jares, M. Kassam K.W. Johnston, R.S.C. Cobbold, R.L. Hummel and P. Arato, "Pulsatile flow visualisation for in-vitro hemodynamic studies related to Doppler ultrasound," Dig. 8th Can. Biol. Eng. Conf. 3-4 (1980).

16. K. Poots, R.S.C. Cobbold, K.W. Johnston, R. Appugliese, M. Kassam, P.E. Zuech, and R.L. Hummel, "A new pulsatile flow visualisation method using a photochromic dye with application to Doppler ultrasound," Ann. Biomed. Eng. **14,** 203-218 (1986).

17. M.M. Werneck, N.B. Jones, and J. Morgon, "Flexible hydraulic simulator for cardiovascular studies," Med. & Biol. Eng. & Comput. **22,** 86-89 (1984).

18. D.J. Patel, J.C. Greenfield Jr., W.G. Austen, A.G. Morrow, and D.L. Fry, "Pressure-flow relationships in the ascending aorta and femoral artery of man," J. Appl. Physiol. **20,** 459-463 (1964).

6. MEASURING THE DYNAMIC ELASTIC PROPERTIES OF VASCULAR SAMPLES

6.1 Introduction

The technique described in chapter 4 for the measurement of the static elastic properties of arterial specimens using a high resolution CT scanner cannot be applied to the measurement of the dynamic elastic properties of excised arteries due to the 4-s image acquisition. Since the arterial wall is not a purely elastic material, but exhibits visco-elastic effects, its mechanical properties must also be studied dynamically.

The visco-elastic properties of the arterial wall have been studied *in vitro* since the mid 1950's. Measurements were performed on isolated canine aortic strips[1] and later on intact aortas[2,3] where the oscillations of the arterial wall were measured upon the application of sinusoidally varying pressure waveforms. Later measurements include those of Gow *et al.*,[4,5] who measured the external diameter of coronary arteries using an electronic calliper attached to the vessel. In all measurements of the visco-elastic properties of the arterial wall, including those performed more recently[6,7] and those performed *in vivo*,[8,9,10,11] only the external dimensions of the vessel were measured. Thus, for the *in vitro* studies, the elastic modulus was calculated using an average wall thickness, which typically was determined from volumetric measurement of the arterial specimen. For the *in vivo* studies, where the wall thickness could not be determined, only the pressure-strain modulus was calculated. Furthermore, in many of these studies,[3,7] heavily diseased arteries were excluded, since for those specimens the arterial mechanical properties vary around the circumference of the vessel.

In this chapter I describe a technique for measuring the dynamic elastic properties of excised vessels, which uses the dynamic CT scanner described in chapter three, in conjunction with the physiological flow simulator described in

chapter five. From the CT images we can quantify not only the external arterial dimensions, but also the wall thickness at all positions around the sample. By tagging the arterial wall with small copper wires, we also are able to quantify the dynamic elasticity of distinct healthy and diseased regions around the vessel circumference. Furthermore, we have applied Fourier analysis in order to obtain the dynamic modulus of elasticity at different frequencies from a single experiment in which the vessel is distended by a pressure waveform with physiologically-relevant shape. A porcine abdominal aorta was used to demonstrate the technique.

6.2 THEORY

6.2.1 Coordinate system

For the purposes of the experiments described in this chapter, we defined a standard coordinate system. The coordinate system is shown in Fig. 6.1, where a quadrant of an image of an artery is displayed schematically. The coordinate system is defined with respect to the centroid of the arterial lumen boundary. All tagging wires are numbered, starting at 0 for the wire at the smallest angle θ, and increasing in the counterclockwise direction. The angle θ is measured with respect to the x axis. The position of a wire *n* (on the outer surface of the arterial wall) is given by its cartesian coordinates (x_n, y_n), or its polar coordinates $(r_{o,n}, \theta_n)$. The wall thickness at wire *n* is given by h_n. The radial distance $r_{i,n}$ is between the origin and the intersection of the inner wall boundary with the line normal to the outside boundary at (x_n, y_n). The distance along the outer boundary between two adjacent wires (*n* and *n+1*) is $a_{o,n}$ and, similarly, the distance along the inner boundary is $a_{i,n}$.

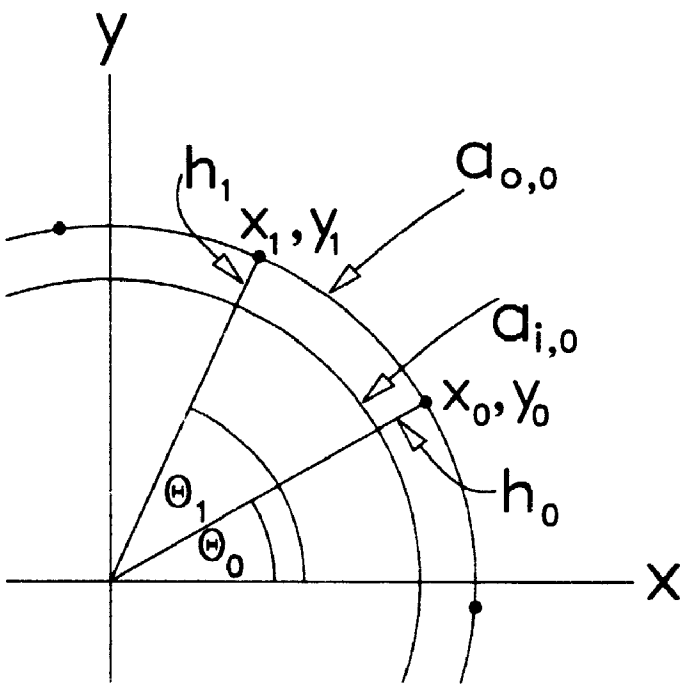

Figure 6.1: Standard coordinate system defining the locations of the tagging wires (see text).

6.2.2 Dynamic modulus of elasticity

The dynamic elastic properties of arterial specimens are commonly characterised by the dynamic modulus E_{dyn} given by[2]

$$E_{dyn}(f) = 2(1-\sigma^2)\frac{\Delta p}{\Delta c_o}\frac{c_i^2 c_o}{c_o^2 - c_i^2}\cos(\phi) \ , \qquad (6.1)$$

where f is the frequency, c_i and c_o are the inner and outer circumferences, p refers to the transmural pressure, σ is Poisson's ratio and ϕ is the phase lag of circumference behind pressure. As in Eq. 4.1, which is equivalent to Eq. 6.1 for static incremental modulus of elasticity, we have substituted circumference for the commonly used radius or diameter measurement. Standard measurement techniques involve the application of low-amplitude sinusoidal pressure waveforms at known frequencies and measuring the corresponding sinusoidal changes in radius or diameter.[3,4,6] The inherent assumption in these measurements is that the vessel wall behaves linearly over the range of the pressure waveform, *i.e.* the radius waveform is also a sinusoid at the same frequency. In this case, the amplitudes of the pressure and radius (or circumference) variations are used as Δp and Δc_o in Eq. 6.1, for the calculation of E_{dyn} at a single frequency. Thus, E_{dyn} at one mean pressure is obtained, for a range of frequencies, from a series of experiments.

Fourier decomposition allows E_{dyn} (at one mean pressure) to be derived as a function of frequency from a single experiment, in which the pressure waveform mimics the waveforms found *in vivo*, provided that the vessel expands linearly with pressure. By evaluating the Fourier transforms (FT) of the pressure and circumference waveforms we can quantify Δp, Δc and ϕ at all harmonics of the heart rate, from a single experiment. Similar Fourier analysis of pressure-diameter data was performed by Imura *et al.*[9] but since they were measuring the elasticity *in vivo* they could not control the amplitude of the pressure waveform to ensure a linear relationship between pressure and arterial diameter.

6.2.3 Variation of E_{dyn} with angular position

Since our imaging technique also allows the measurement of strain and wall thickness of distinct segments around the circumference of the vessel, we have modified Eq. 6.1 in order to calculate E_{dyn} of the distinct segments. The modification involves the separation of Eq. 6.1 into a "strain term" and a "stress term". The strain is evaluated from the segment length and the stress from the transmural pressure, the average wall thickness, and the average radius of curvature for the segment. Thus, Eq. 6.1 becomes

$$E_{dyn,n}(f) = 2(1-\sigma^2)P(f)\frac{1}{\left(1+\frac{2\pi h_n(0)}{A_{i,n}(0)}\right)^2-1}\frac{A_{o,n}(0)}{A_{o,n}(f)}\cos(\phi(f)), \qquad (6.2)$$

where n is the segment index, $A_{i,n}(0)$ and $A_{o,n}(0)$ are the mean inner and outer segment lengths respectively, and are determined from the magnitudes of the FT's of $a_{i,n}(t)$ and $a_{o,n}(t)$ at zero frequency. The magnitude of the FT of $a_{o,n}(t)$ at f is $A_{o,n}(f)$, and similarly $P(f)$ is the magnitude of FT(p(t)) at f. The phase lag $\phi(f)$ is determined by subtracting the phase of FT(c_o(t)) from FT(p(t)) Since the phase lag is typically very small and independent of frequency, many researchers disregard its effect on the dynamic modulus. We have chosen to use the phase lag between $c_o(t)$ and $p(t)$, obtained from the first harmonic, for all calculations.

6.3 Methods

6.3.1 Arterial specimen preparation

The arterial specimen (a porcine abdominal aorta) was stored as described in chapter three. Prior to the imaging experiment, all loose connective tissue surrounding the sample was separated from the vessel, leaving only a clean

adventitial surface. All branching arteries were tied off, ensuring that the vessel was pressure tight.

In order to distinguish between different segments of the arterial wall, appropriate markers needed to be attached to the wall. These markers had to provide sufficient radiographic contrast in order to be tracked easily in the images, yet be small and light enough not to affect the vessel's mechanical properties. Thin copper wire (70-μm diameter) was chosen as the tagging material which met these

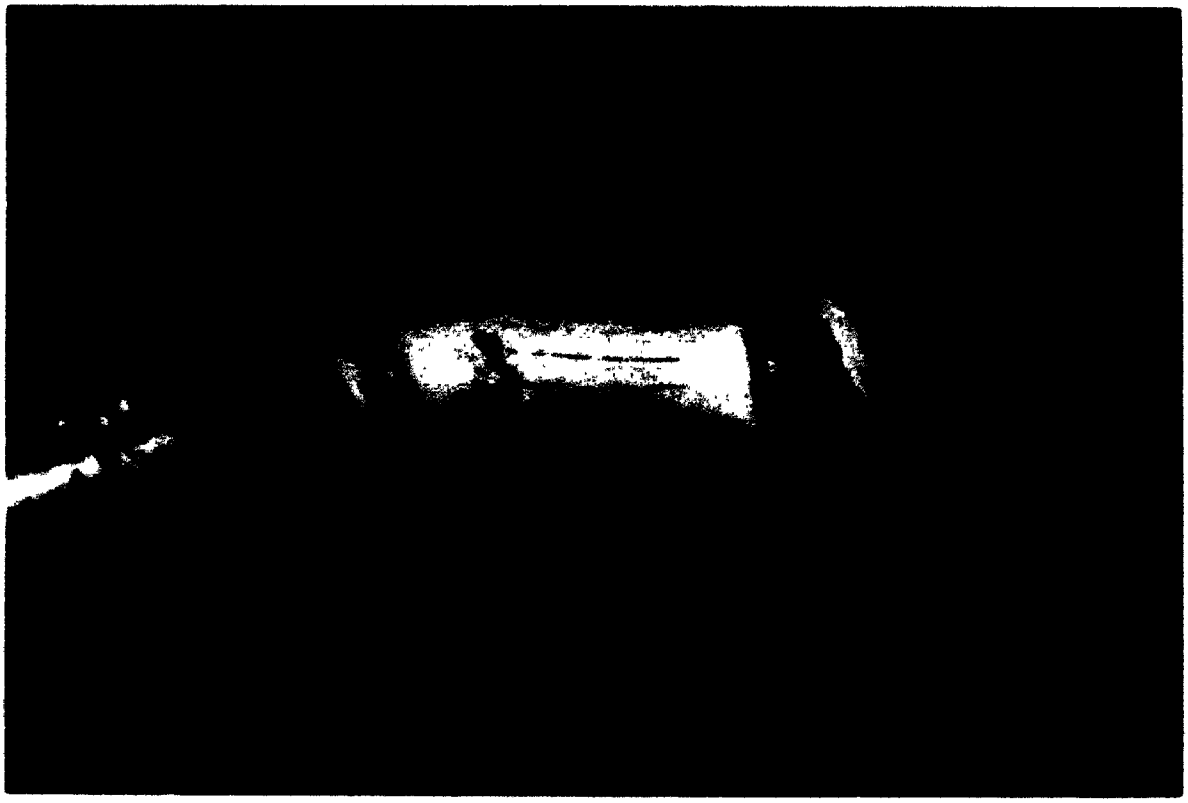

Figure 6.2: Photograph of an artery illustrating the tagging wires which were inserted into the adventitia. (The external diameter of the mounting tube was 9 mm.)

requirements. The tagging wires were inserted just within the adventitia tissue at a spacing of approximately 6 mm around the circumference in the area to be imaged, as shown in Fig. 6.2. In order to facilitate the accurate positioning of the tagging wires just within the outer layers of the adventitia, wire insertion was performed while

keeping the vessel distended by saline solution under pressure. The wires were 1.5-2 cm in length and were not tethered in the longitudinal direction. The total weight of the wires was less than 10 mg, which was less than 1% of the weight of the vessel segment. This small mass should have a negligible effect on the mechanical properties of the vessel wall, and is much less than the mass of measurement devices attached to the wall in previous studies (for comparison, the calliper used by Gow *et al.*[4] weighed 250 mg).

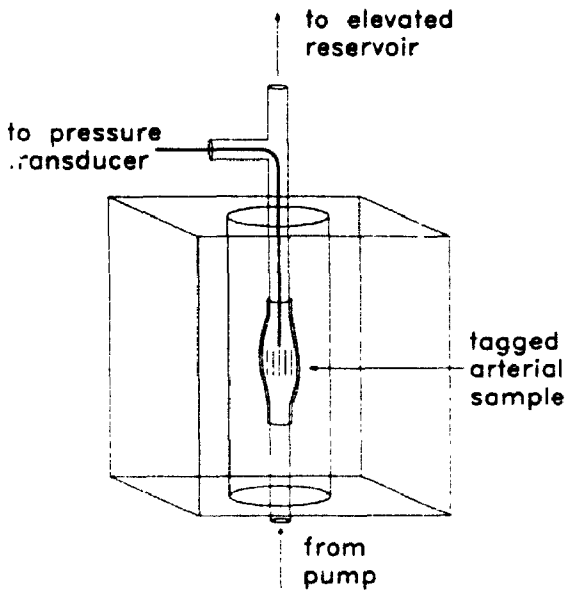

Figure 6.3: Schematic diagram of the mounted specimen. Iodinated saline is pumped through the vessel by the physiological flow simulator. Images are acquired through the tagged portion of the sample, while the pressure is monitored.

Once the wires were inserted, the artery was mounted in the specimen holder as illustrated in Fig. 6.3. The artery may be surrounded by saline solution, moist air, or iodinated saline solution. For the experiment described here, the artery was surrounded by humidified air.

6.3.2 Pressure waveform generation

Pressure waveforms were generated using a commercial version of the flow simulator described in chapter five (University Hospital Development Corporation, London, Ont. Canada). Iodinated isotonic saline solution (30 mg ml^{-1}) was used in order to provide radiographic contrast between the vessel and its lumen. A reservoir elevated to 1.5 m above the vessel and placed downstream of the vessel provided a pressure offset, approximately equivalent to the diastolic pressure (see Fig. 6.3).

The pressure in the artery was measured using a 4.5 F end-hole catheter connected to a Cobe pressure transducer. The pressure measurements were digitized during the acquisition of each time-evolved projection (see below) to confirm that the pressure waveform remained constant. Prior to image acquisition the shape of the pressure waveform was monitored on an oscilloscope and the flow waveform was scaled until a low-amplitude physiologically-relevant pressure waveform was obtained.

6.3.3 Distensibility measurements

To measure arterial distensibility, transverse CT images of the vessel at different points in the cardiac cycle were acquired using the scanner described in chapter three. CT images were reconstructed from one hundred gated time-evolved projections. Each time-evolved projection was acquired over one cardiac cycle, which in this case was 0.84-s long. Gating pulses were provided by the flow simulator. Since there is a short disturbance in the flow waveform when the pump piston reverses direction, the timing of this direction change needed to be monitored as well as the ECG trigger. Following the detection of a piston reversal, four of the succeeding waveform cycles were omitted. The radiographic parameters were 90 kVp with 3 mm Al added filtration and 50 mA, and the total scan time for 100 projections was 41 minutes. The XRII was zoomed to the smallest field-of-view.

In this experiment we applied a low amplitude physiological pressure waveform with a mean pressure of 13.3 kPa. The experiment was repeated four times to characterise the precision of the measurements, for imaging biological specimens, and to investigate the diffusion of contrast medium into the arterial wall.

A set of time-evolved projections was also obtained for a 1.19-Hz sinusoidal distending pressure waveform, with a mean pressure of 14.5 kPa and amplitude of 1.25 kPa. The amplitude of this sinusoidal waveform was similar to the magnitude of the component of the physiological pressure waveform at the same frequency.

Finally, the wires were removed without disturbing the vessel and a set of time-evolved projections was obtained in order to ensure that the tagging wires did not affect the mechanical properties of the vessel. The time-evolved projections were reformatted and reconstructed as described in chapter three.

6.3.4 Image analysis

The boundary between two materials, such as the lumen and the arterial wall, was determined from the CT images by setting a threshold at a value equal to the mean of the two materials. To ensure that only contiguous points in the image were considered, cluster growing techniques[12] were used in the extraction of the lumen boundary, outer wall boundary and the wires. The center of gravity of the arterial section was calculated as the centroid[12] of the lumen region. Streak artefacts from the highly-attenuating Cu wires may perturb the lumen boundary and thus increase its apparent perimeter. To avoid this problem we converted the points which define this boundary to polar coordinates, replicate the data for $\pi/4$ beyond $\pm\pi$, and fit a ninth-order polynomial to the data.

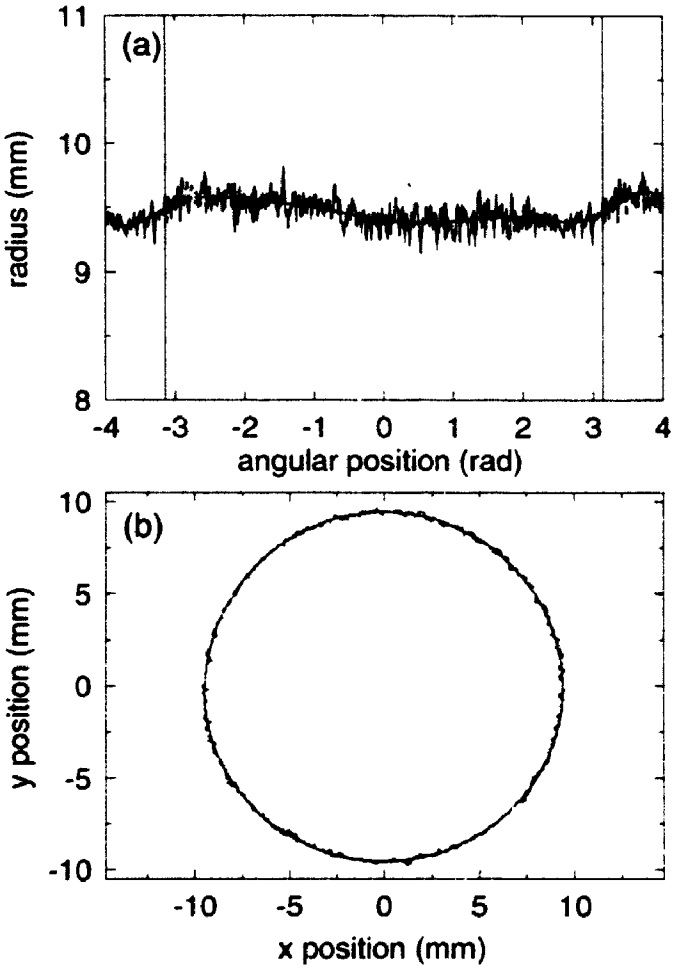

Figure 6.4: (a) Radial position versus angular position with a 9th order polynomial fit through the data. The vertical lines correspond to $\pm\pi$. (b) The same data shown in cartesian coordinates.

This procedure, which smooths the boundary is illustrated in Fig 6.4. The positions of the tagging wires were also converted to polar coordinates, as described above. Spline curves were fit to the positions (in polar coordinates) of the wires to define the boundary. The inner boundary segments were determined from the intersections of the normals to the outer boundary, which pass through the wire centroids, with the inner boundary. The segment lengths $a_{o,n}$ and $a_{i,n}$ were determined from the spline and the polynomial fit, respectively, by numerical line integration.

6.3.5 Elastic modulus calculation

The inner and outer circumferences, all segment lengths and the pressure waveform were Fourier transformed. The wall thickness was also calculated at each tagging position, and the mean for each segment was determined by averaging the thicknesses at the two tagging positions which define the segment. From these, and using Eq 6.2, the dynamic modulus of elasticity was calculated as a function of frequency for the different segments. A mean E_{dyn}, over the arterial circumference, was also calculated from the total circumferential strain.

6.4 Results

6.4.1 CT images and analysis

Figure 6.5(a) shows a cross-sectional image through the vessel at peak systole. The image in Fig. 6.5(b) shows the locations of the tagging wires and the inner and outer wall boundaries, which were obtained from the image in (a) using the techniques described above. Segment 4 was the posterior wall of the artery. Figure 6.6 shows the wire positions, outer boundary and inner boundary for the vessel section at peak systole and diastole.

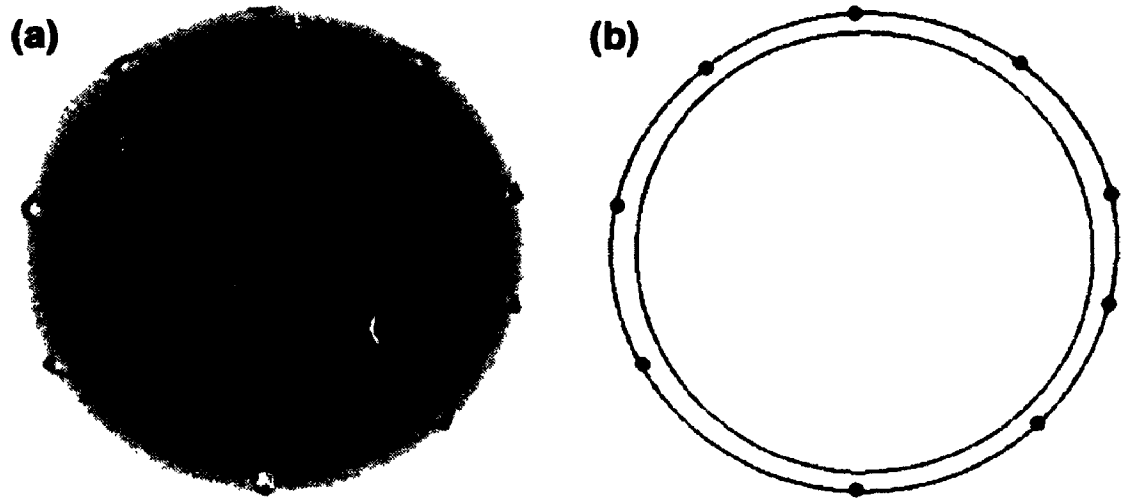

Figure 6.5: (a) CT image of the porcine aorta at peak systole. (b) The inner and outer wall boundaries, along with the positions of the tagging wires have been extracted from the image in (a).

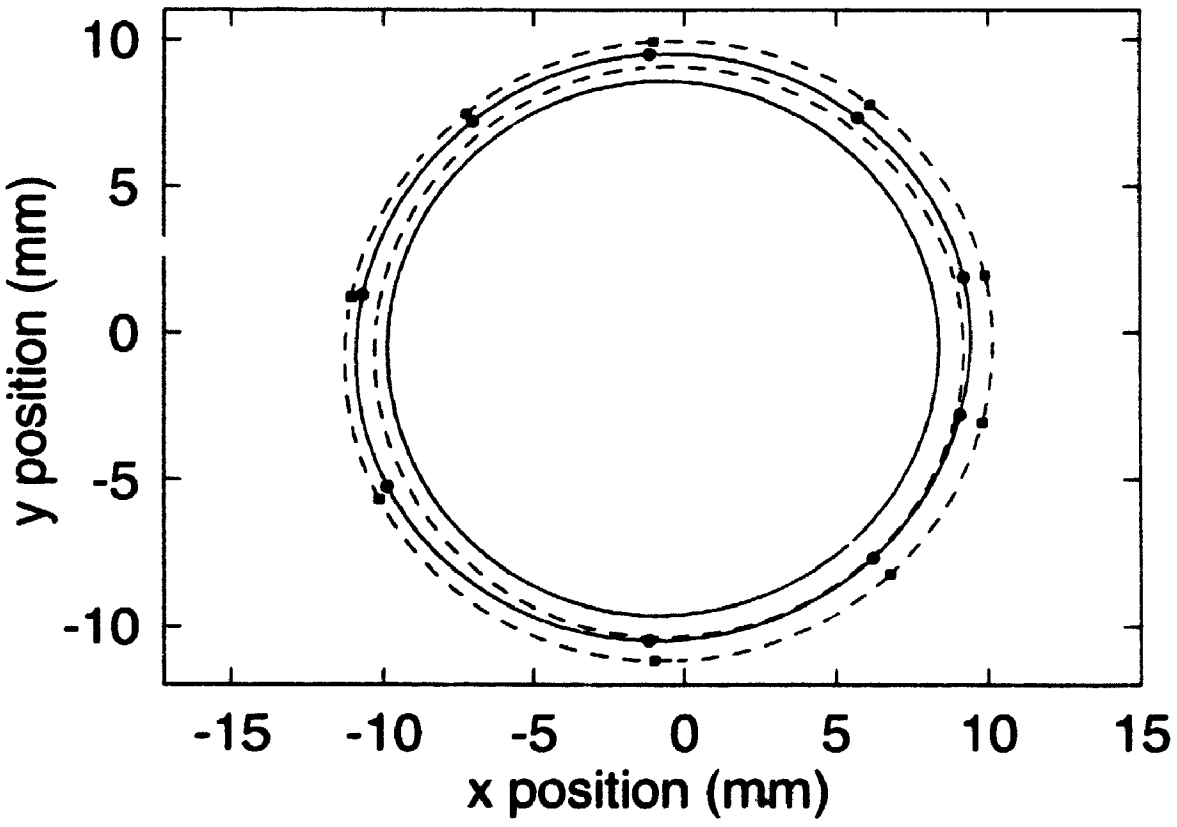

Figure 6.6: The inner and outer wall boundaries are plotted for peak systole (dashed line) and diastole (solid line). The wire positions for both are also shown.

6.4.2 Verification of linear response

As a verification that the arterial wall responds linearly with pressure we have plotted the $p(t)$ and $c_o(t)$, along with the corresponding Fourier transforms in Fig. 6.7, for the sinusoidally varying pressure waveform. Figure 6.7(a) shows that, although the pressure waveform was not a pure sinusoid, less than 1% of the power was distributed at frequencies higher than the first harmonic. The waveform produced by the pump was probably altered slightly by the compliance of the tubing, which connected the pump to the artery. If the pressure were purely sinusoidal, any power at higher frequencies would indicate a non-linear system. The FT of the outer circumference (Fig. 6.7(b)) does not show excess power distributed to the higher frequencies, compared to that of the pressure waveform. This indicates that the assumption of linear response is reasonable for pressure waveforms with a mean near 14 kPa and amplitude smaller than 1.3 kPa.

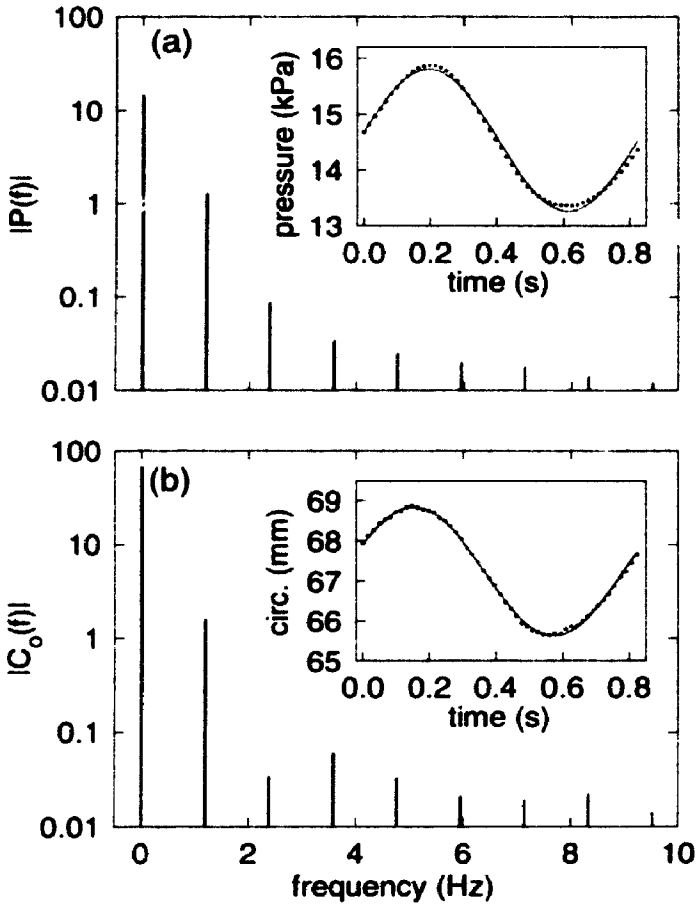

Figure 6.7: (a) Sinusoidally applied pressure waveform (inset) and the magnitude of its Fourier transform. (b) The resultant outer circumference (inset) and the magnitude of its Fourier transform.

The applied physiologically-shaped pressure waveform is shown in Fig. 6.8(a). The pressure waveforms recorded during the acquisition of the four sets of 100 time-

evolved projections were reproducible to within 1%. A representative error bar is shown in Fig. 6.8(a). The FT of the physiological pressure waveform is shown in Fig. 6.8(b). The amplitude of the first harmonic is comparable to the amplitude of the sinusoidal pressure waveform used to test that the wall responds linearly to changes in pressure. Thus, we can apply Fourier theory in order to characterise the dynamic elastic properties of this vessel at different frequencies.

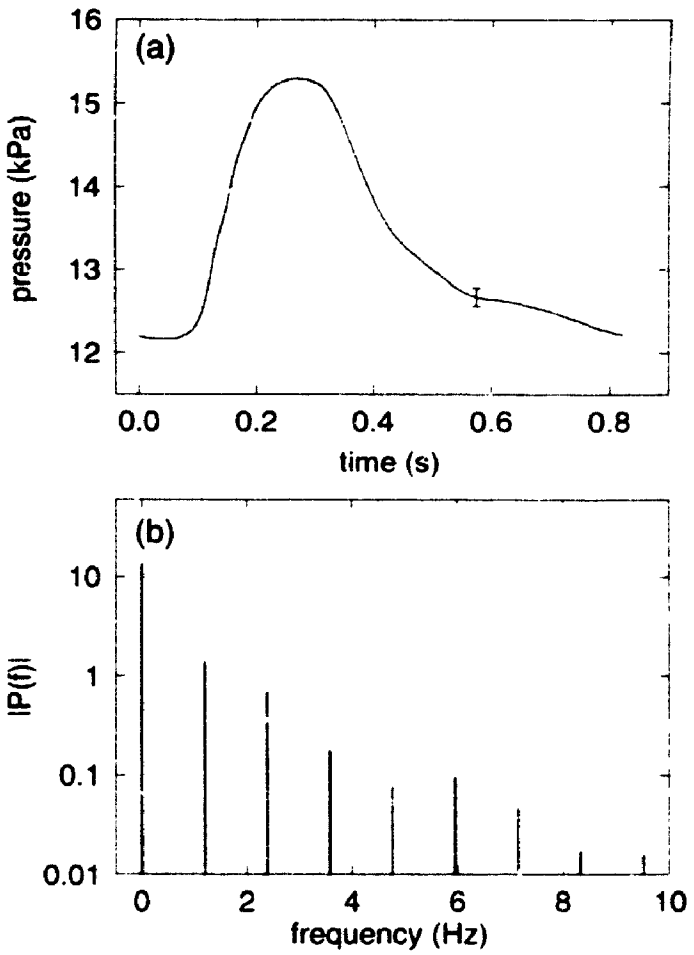

Figure 6.8: The physiological pressure waveform which was applied (a) and the magnitude of its Fourier transform (b).

6.4.3 Measurement precision and contrast-agent diffusion

Figure 6.9(a) shows the apparent decrease in mean wall thickness with time, caused by the diffusion of iodinated contrast material from the intimal side of the vessel wall. The wall thickness shown is the mean over the cardiac cycle and the dashed lines show the full range of variation over the cardiac cycle. These were calculated from the cross-sectional images for the four different studies performed with the same pressure waveform, and using the same threshold level when segmenting the lumen boundary. When these data are extrapolated to the start of the experiment (by a second order polynomial fit) the mean wall thickness was found

to be 0.98 mm, compared to 0.96 mm for the mean wall thickness obtained from the first series of images. Since the decrease in apparent wall thickness will have a significant effect on the calculated elastic modulus, we only calculated the modulus from the first set of images. However, the outer boundary (and outer segment lengths) could be compared, since the outer boundary of the vessels is defined by the tagging wires, which are unaffected by the diffusion of contrast agent into the wall. Thus, we plotted the average $c_o(t)$ and $a_{o,3}(t)$ in Fig. 6.9(b), where the error bars represent the standard deviation over the four experiments. The precision in the outer circumference measurements was ±0.2 mm, which is similar to that reported for static objects in chapter three. The precision in the segment-length measurements was ±0.05 mm.

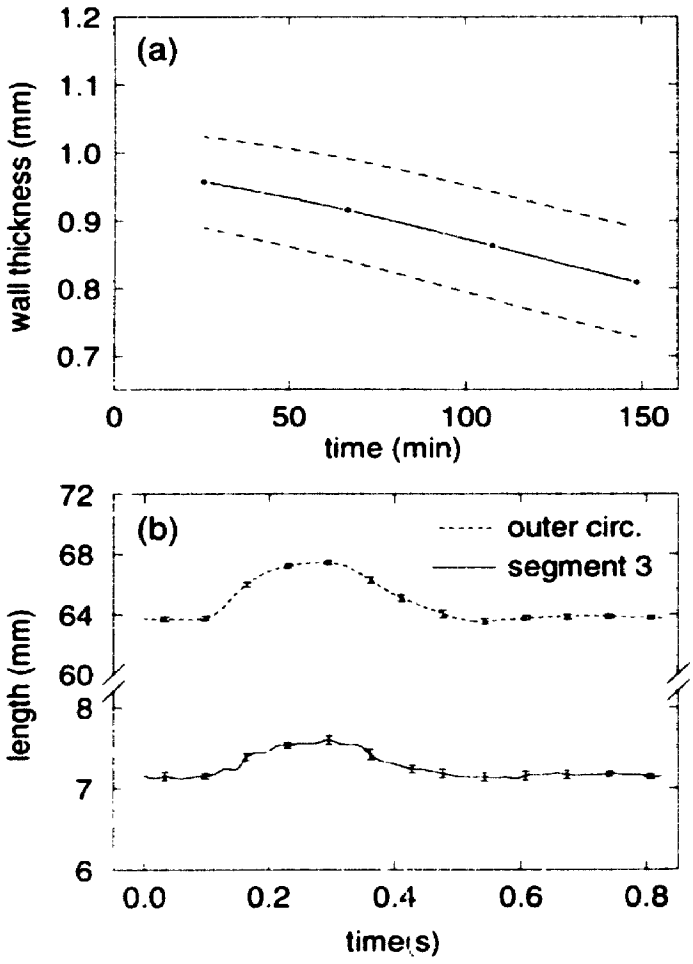

Figure 6.9: (a) Decrease in wall thickness observed due to diffusion of contrast agent into the wall. (b) Outer circumference and the length of segment 3 versus time. The error bars represent one standard deviation over the four series of images.

Figure 6.10 is a plot of the uncertainty in the magnitude of the FT as a function of frequency. The data were obtained for the outer circumference and the segments from the four series of images, by calculating the standard deviation and

the mean of the magnitudes of the Fourier transforms. The figure shows that there is a dramatic increase in this uncertainty for frequencies above 8 Hz, and as expected, the uncertainty is greater for the individual segments.

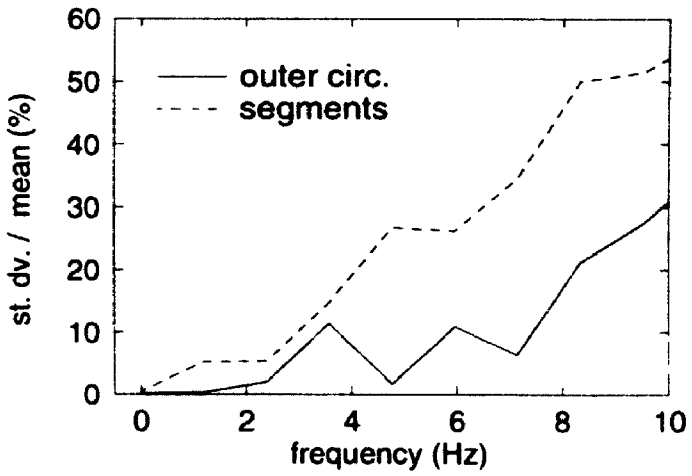

Figure 6.10: Plot of the ratio of standard deviation over the mean amplitude as a function of frequency for the outside circumference (solid line) and the segments (dashed line).

6.4.4 Effect of tagging wires

By the end of the experiment, when the tagging wires were removed, the iodinated contrast agent had diffused through the arterial wall and no wall was "visible" in the images. Thus, only the outer circumference could be measured from these images. This was done by segmenting the artery from the surrounding air and fitting a ninth order polynomial to the boundary coordinates. The outer circumference was the same as that when the wires were still in place to within 1.5%, and the magnitude of the excursion between systole and diastole was the same to within 1%, thus indicating that the tagging wires did not alter the mechanical properties of the vascular wall significantly.

6.4.5 Dynamic modulus of elasticity

Figure 6.11 shows that the wall thickness varied with angular position and that the change in wall thickness over the cardiac cycle also varied with angular position. For instance, the change in wall thickness between systole and diastole for segment 7 ($\theta = -1.3$ radians) was 8% (of the mean), while it was only 1% for segment 3 ($\theta = 2.7$ radians).

Figure 6.12(a) shows $E_{n,dyn}(f)$ for three of the segments as a function of frequency. The phase lag of circumference behind pressure was 0.2 radians. The

mean $E_{dyn}(f)$ over the vessel circumference was calculated both by averaging $E_{n,dyn}(f)$ and by using the circumferential strain $\left(\frac{C_o(0)}{C_o(f)}\right)$ in Eq. 6.2 instead of the segment strain $\left(\frac{A_{o,n}(0)}{A_{o,n}(f)}\right)$. The agreement between the two means is shown in Fig. 6.12(b). The variation of E_{dyn} with angular position is displayed in Fig. 6.13 for the first three harmonics.

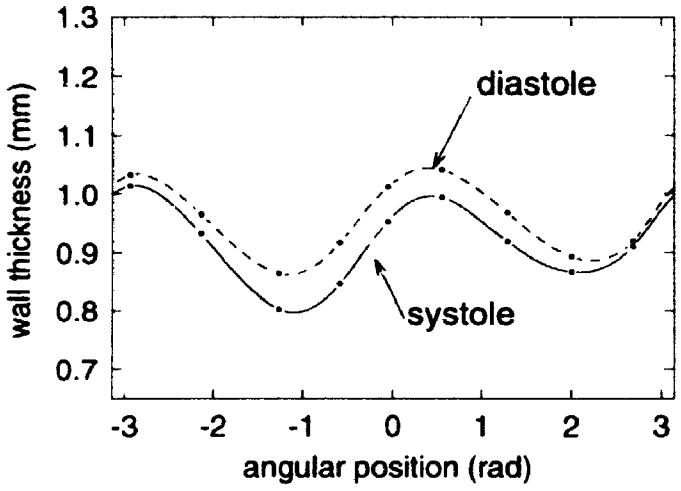

Figure 6.11: Wall thickness at systole and diastole as a function of radial position.

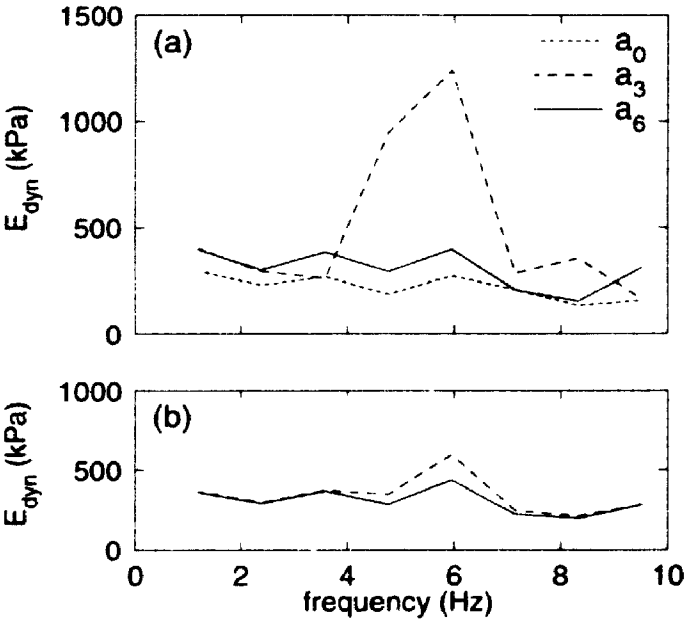

Figure 6.12: (a) $E_{dyn}(f)$ for three segments. (b) Mean $E_{dyn}(f)$ calculated from $E_{n,dyn}(f)$ (dashed line) and from the circumference-pressure measurements (solid line).

6.5 Discussion and Conclusions

In this chapter I have described a novel technique for the measurement of the dynamic elastic properties of intact excised arterial samples. The technique allows $E_{dyn}(f)$ to be determined not only for a transverse section of the vessel, but for separate segments around the circumference of the vessel. By using the dynamic CT scanner described in chapter three we can monitor the movement of both the inner and outer boundaries of the vessel wall, and since the copper wires provide reliable tagging of the wall, we can measure the wall thickness of each

segment directly. From the individual wall thicknesses and the individual strains, we can quantify the dynamic mechanical properties of the different segments. This ability would be of particular importance when the technique is applied to diseased vessels, which typically have plaques distributed in a patchy fashion.

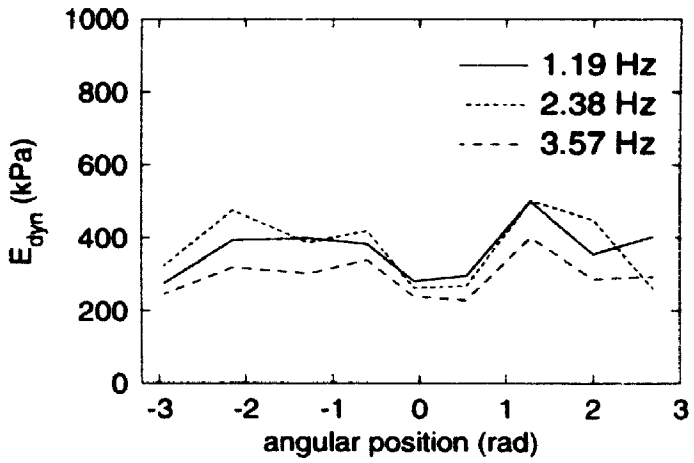

Figure 6.13: E_{dyn} is plotted as a function of angular position for the first three harmonics.

We have used a porcine abdominal aorta to demonstrate the technique. By using a low amplitude transmural pressure waveform and Fourier analysis, we were able to characterise the dynamic modulus of elasticity at different frequencies (for a mean pressure of 13.3 kPa) from only one experiment. Since Fourier analysis is only valid for a linear system, we verified that the arterial wall distends linearly with pressure, over the small pressure range studied, by applying a sinusoidally varying pressure waveform and showing that the resultant variation in circumference is also sinusoidal.

The technique described in this chapter allows the circumference and the segment lengths to be measured with a precision of ±0.2 mm and ±0.05 mm respectively. When $c_o(t)$ and $a_{o,n}(t)$ are Fourier transformed, however, the uncertainty in $C_o(f)$ increases with increasing frequency and is greater than 20% for frequencies above 8 Hz (see Fig. 6.10). The uncertainty in $A_{o,n}(f)$ increases at a higher rate than that in $C_o(f)$, and thus the uncertainty in $E_{dyn,n}$ would be higher than that of the average E_{dyn} (around the circumference), especially for frequencies above 4 Hz.

The dynamic elastic modulus results presented here show that for this artery, there was no significant change in E_{dyn} with increasing frequency above the first harmonic. Figure 6.12 shows E_{dyn} for frequencies up to 10 Hz, although Fig. 6.10 demonstrated that the uncertainty in E_{dyn} above 8 Hz is large. However, multiple experiments on the same vessel or on an ensemble of vessels would reduce this uncertainty. Previous studies on porcine thoracic aortas[13] reported comparable values for E_{dyn} for the frequencies investigated here. Goedhard and Knoop's[13] results show that the dynamic elastic modulus increases for frequencies below 2 Hz to a value near 700 kPa. Our results show an average E_{dyn} of about 320 kPa. Goedhard and Knoop's[13] study was performed on freshly excised rings of aortic tissue, with the smooth muscle in a relaxed or contracted state, and showed a small increase in dynamic modulus when the muscle was contracted. Since our experiments were performed three days after the swine was slaughtered, we expect that smooth muscle did not have an effect on the mechanical properties. Our technique could, however, be used to study the effects of smooth muscle, provided that the vessel is kept in physiological solution which simulates the natural environment of the tissue and that the experiment is performed soon after death.[6,13]

For the static elasticity experiments described in chapter four we used humidified air to provide contrast between the arterial wall and its surroundings. Unfortunately, for the dynamic studies radiographic contrast agent must be pumped through the vessel. As is shown in Fig. 6.9 the iodinated compound diffuses into the wall, at a rate of 1 $\mu m\ min^{-1}$, even at the low concentration used in our experiments. Holdsworth *et al.*[14] reported a higher diffusion rate (20 $\mu m\ min^{-1}$), during their tissue-thickness measuring experiments, but in those experiments the iodine concentration was ten times greater, and the solution was not isotonic. To reduce the effects of diffusion, care must be taken to minimise the time over which the

vessel is exposed to the iodinated solution, by beginning image acquisition as soon after the vessel is mounted as possible. As discussed in chapter three, it is possible to reduce the total acquisition time to less than five minutes if a higher-heat-capacity tube were available. In this case the diffusion of contrast agent would not pose a significant problen., and would allow the experiment to be repeated at a number of mean pressures.

The technique presented here, in combination with that presented in chapter four for the measurement of the static elastic properties of intact arterial specimens, represents a powerful tool for the investigation of the differences in mechanical properties between healthy and diseased arterial specimens. Since both techniques are non-destructive, direct correlative comparisons can be performed between the static and dynamic mechanical properties and composition of the same vessel.

REFERENCES

1. W. Lawton, "Measurements on the elasticity and damping of isolated aortic strips of the dog," Circ. Res. **3**, 403-408 (1955).

2. D.H. Bergel, "The dynamic elastic properties of the arterial wall," J. Physiol. **156**, 458-469 (1961).

3. B.M. Learoyd and M.G. Taylor, "Alterations with age in the viscoelastic properties of human arterial wall," Circ. Res. **18**, 278-291 (1966).

4. B.S. Gow, D. Schonfeld, and D.J. Patel, "The dynamic elastic properties of the canine left circumflex coronary artery," J. Biomechanics **7**, 389-395 (1974).

5. B.S. Gow and C.D. Hadfield, "The elasticity of canine and human coronary arteries with reference to postmortem changes," Circ. Res. **45**, 588-594, (1979).

6. A.M. Brant, S.S. Shah, V.G.J. Rogers, J. Hoffmeister, I.M. Herman, R.L. Kormos, and H. Borovetz, "Biomechanics of the arterial wall under simulated flow conditions," J. Biomechanics **21**, 107-113 (1988).

7. G.L. Papageorgiou and N.B. Jones, "Circumferential and longitudinal viscoelasticity of human iliac arterial segments *in vitro," J. Biomed. Eng.* **19**, 82-90 (1988).

8. A.P.G. Hoeks, P.J. Brands, F.A.M. Smeets, and R.S. Reneman, "Assessment of the distensibility of superficial arteries," Ultrasound in Med. & Biol. **16**, 121-128, (1990).

9. T. Imura, K. Yamamamoto, T. Satoh, K. Kanamori, T. Mikami, and H. Yasuda, "In vivo viscoelastic behaviour in the human aorta," Circ. Res. **66**, 1413-1419 (1990).

10. T. Lanne, H. Stale, H. Bengtsson, D. Gustafsson, D. Bergqvist, B. Sonesson, H. Lecerof, and P. Dahl, "Noninvasive measurement of diameter changes in the distal abdominal aorta in man," Ultrasound in Med. & Biol. **18**, 451-457 (1992).

11. Y. Tardy, J.J. Meister, F. Perret, H.R. Brunner, and M. Arditi, "Non-invasive estimate of the mechanical properties of peripheral arteries from ultrasonic and photoplethysmographic measurements," Clin. Phys. Physiol. Meas. **12**, 39-54 (1991).

12. W.K. Pratt, *Digital Image Processing*, (John Wiley & Sons, New York, 1991) pp. 606-626.

13. W.J.A. Goedhard and A.A. Knoop, "A model of the arterial wall," J. Biomechanics **6**, 281-288 (1973).

14. D.W. Holdsworth, P.J. Dunmore, M.R. Roach, and A. Fenster, "A digital-radiographic technique for *in vitro* tissue thickness measurement using iodine displacement," Med. Phys. **19**, 545-554 (1992).

7. SUMMARY AND FUTURE APPLICATIONS

This chapter briefly summarizes the results of my research and outlines a few possible avenues for extending the applications of the high-resolution dynamic computed-tomography (CT) scanner in the future.

7.1 Summary of Results

7.1.1 Modified XRII

The requirement for a high-resolution detector, which could be used as the x-ray detector for the dynamic CT scanner, resulted in the modification of a conventional x-ray image intensifier (XRII) to extend its limiting resolution for small fields-of-view. This was achieved by varying the voltages applied to the electrodes which define the size of the field-of-view and focus the image at the output phosphor of the intensifier. We found that reducing the field-of-view from 24 cm to 8 cm, by electro-optical means, increased the limiting resolution $f_{0.1}$ by a factor of 2.2. Achieving the same reduction in size using an optical zoom lens increased $f_{0.1}$ only by a factor of 1.3. With this modification we were able to increase the limiting resolution of a conventional XRII to a level that was sufficient for imaging arterial specimens.

7.1.2 Laboratory CT scanner for dynamic imaging

Using the modified XRII and a linear photo-diode array detector, a high-resolution dynamic CT scanner was built for measuring the dynamic mechanical properties of excised arterial samples. It can be used to provide dynamic images of a single-slice of an object undergoing periodic motion. The CT images are reconstructed from gated time-evolved projection radiographs, which are acquired around the object. Currently, the images are obtained at a rate of 60 Hz, although this rate could be increased to as high as 300 Hz with the existing equipment. Although additional image blurring occurs for moving objects, the limiting resolution

is decreased only by 9% for objects moving at 1 cm s^{-1} (in comparison with that obtained for static objects). The highest limiting resolution achievable with the scanner is 3.2 mm^{-1}. The scanner's response is linear with changes in attenuation coefficient varying between 0 and 1.5 cm^{-1}. Of particular importance to the use of the scanner, to the investigation of the mechanical properties of arterial specimens, is the geometrical accuracy and precision. The accuracy and precision in geometric measurements were ±0.3 mm and ±0.2 mm, respectively. This innovative CT scanner, with its high spatial and temporal resolution, provides a unique opportunity to analyze the dynamic mechanical properties of intact human vessels under simulated physiological conditions.

7.1.3 Technique for measuring the static elastic properties of vessels *in vitro*

Prior to developing a technique for measuring the *dynamic* elastic properties of excised arteries, we developed a technique for measuring the geometry and *static* mechanical properties of intact arterial specimens. There are two major advantages of this technique over existing techniques for measuring static mechanical properties: (1) the ability to measure the inner and outer circumferences, wall thickness and transmural pressure simultaneously; and (2) the capability to measure the three-dimensional geometry of the arterial specimen. Furthermore, the nondestructive nature of the imaging techniques provides a unique opportunity for directly correlating the local mechanical properties with the histologically-obtained composition of the wall. The technique was demonstrated using an intact human abdominal aorta with an aneurysm. The results showed that, for this sample, the increase in circumferential modulus of elasticity measured in the aneurysm was correlated with a substantial decrease of elastin content. To the best of my knowledge, this is the first direct correlation between local mechanical properties and arterial wall composition in intact arterial specimens.

7.1.4 Pump for physiological flow simulation

Our ability to measure the dynamic elastic properties of arterial specimens *in vitro* depended on a device which could reproduce physiological flow and pressure waveforms reliably. A dual-piston positive-displacement pump was, thus, designed to produce highly-reproducible physiologically-relevant flow waveforms, as well as nearly uninterrupted steady flow. This pump was essential for distending excised arterial samples under physiological pressures. Steady flow produced by the pump has an accuracy and precision better than ±1%. The reproducibility of physiological flow waveforms over thousands of cycles (measured as the standard deviation in flow rate at a point of the cycle) is ±0.1 ml s^{-1}. Since the pump is computer-controlled and programmable, various waveform shapes can be produced, including waveforms with reverse-flow components. The computer-controlled pump has been commercialized and is currently being used in similar vascular studies, using magnetic resonance and ultrasound, in laboratories around the world.

7.1.5 Technique for measuring the dynamic elastic properties of arteries *in vitro*

The dynamic CT scanner and the physiological flow simulator allowed me to extend the static technique into a technique for measuring the dynamic elastic properties of excised arteries *in vitro.* The technique was further expanded by the attachment of fine tagging wires to the adventitial surface of the vessel, thus enabling the measurement of the dynamic elastic modulus of different segments around the circumference of the specimen. Application of a low-amplitude pressure waveform allowed the use of Fourier analysis to decompose the pressure waveform and the corresponding circumferential measurements into sinusoids at frequencies corresponding to the harmonics of the heart rate. Thus, the dynamic elastic modulus could be calculated, at several circumferential positions, and at different frequencies, from a single experiment.

7.1.6 Discussion

The dynamic CT scanner described in this thesis is a unique device, which can be used to provide high-resolution tomographic images of objects undergoing periodic motion. This device, along with the physiological flow simulator, and the techniques described in chapters four and six provide an opportunity to study the mechanical properties of excised vessels under conditions mimicking those found *in vivo*. These techniques provide the first opportunity to characterize the differences in distensibility around the circumference of an intact vessel and to correlate variations in distensibility directly with variations in composition. In addition to the investigations presented in the body of this thesis, there are many other research and clinical applications for this technology. I will outline some of these possible avenues for future research in the concluding section of this chapter.

7.2 Future Applications

In this section I suggest improvements to and extensions of the work presented in the thesis, and introduce suggestions for future applications of the dynamic CT scanner. One promising application is the use of the scanner and physiological flow simulator for measuring velocity and shear rate in excised vessels. An application of the technique for the acquisition of gated time-evolved projections to clinical imaging is also discussed.

7.2.1 CT scanner modification

In its current configuration, the dynamic CT scanner can acquire only one tomographic section at a time. However, as discussed in chapter three, we only use 512 of the 1024 diode elements available. Thus, the remaining 512 elements are available to acquire another section of the specimen. If a pair of narrow transverse collimators are placed at the input of the XRII, as shown in Fig. 7.1(a), instead of the single one currently used, the projection radiographs of two sections of the object

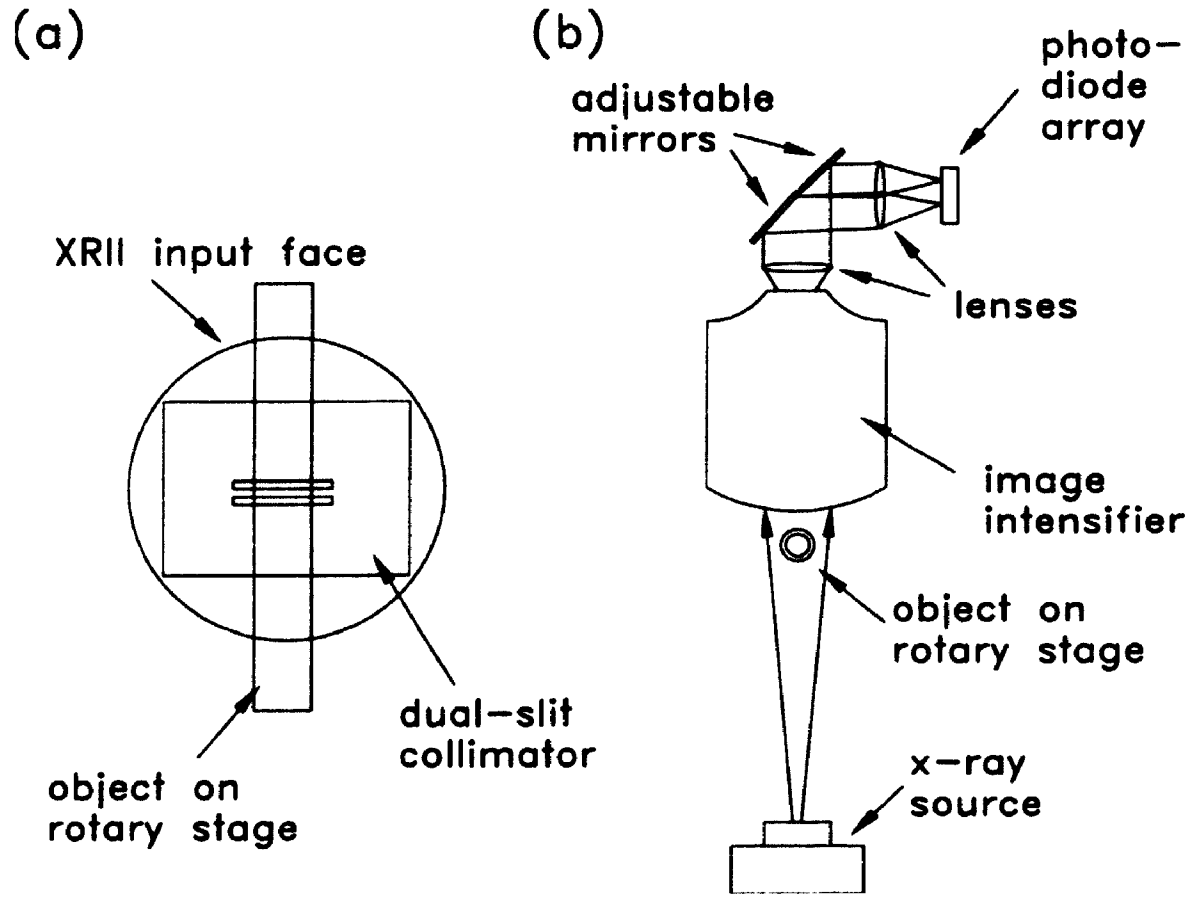

Figure 7.1: (a) The XRII input face with the two collimators. (b) Top view of the system showing the orientation of the mirrors and the PDA.

would be seen with a two-dimensional detector coupled to the XRII. Since the PDA is only a linear detector, we need to shift the projection of one section to be in horizontal alignment with the projection of the other section. One possible way to achieve this would be to place a pair of front-surface mirrors in the optical path between the two relay lenses. Figure 7.1(b) illustrates this possible combination. The mirrors can be adjusted on three-point mounts to shift the image of one collimator so that it is lined up horizontally with the image of the other collimator. Thus, the first 512 diode-array elements can be used to image one slice, while the next 512 elements image a slice above or below it. Using this scheme, the projections of two slices can be recorded simultaneously, at rates as high as 300 Hz.

The system could also be expanded to acquire full three-dimensional images rapidly. This can be achieved if a charge-coupled device (CCD) camera is used as the optical detector. The analog signal from the video camera can be recorded at a rate of 30 frames per second, which may be adequate for some applications. Also, some commercial CCD video cameras are available with electronic shutters, which can limit exposure times to as little as 0.1 ms. Such devices could be implemented for applications where blurring due to motion has to be minimized. An important parameter that must be considered in the use of a CCD video camera is the lower dynamic range of these cameras. Thus, a conventional CCD video camera may not be appropriate for applications where extremely low-noise images are required, but may require specialized electronics and/or cooling.

7.2.2 Measuring the static and dynamic properties of arterial specimens

Chapters four and six describe two separate techniques, using two separate laboratory CT scanners, for the measurement of the static and dynamic elastic properties of excised arterial specimens. These two techniques can be combined in order to characterize both the static and dynamic mechanical properties of a specimen, as well as its three-dimensional geometry and composition. This can be achieved by either combining the two scanners into one (by attaching the photo-diode array based camera to an auxiliary port of the XRII) or by using the dynamic scanner to obtain both the static and dynamic images of single sections. The volume CT scanner can be used only for the acquisition of the 3-D image. Since the measurements of static elasticity are performed on a single slice of the vessel, rather than the complete volume, tagging wires can also be used while performing the static experiments. This will provide a measure of the static incremental modulus of elasticity for different segments around the circumference of the selected slice.

In order to study the static and dynamic mechanical properties of a single vessel, as well as to assess the complete 3-D geometry, I propose that the sample, with the inserted tagging wires, be mounted in the humidified-air chamber in order that static measurements of the mechanical properties can be performed. The sample must then be pre-conditioned to avoid the effects of creep and hysteresis before cross-sectional images are obtained at different transmural pressures and at different positions along the sample. Once the static measurements are completed, the physiological flow simulator can be attached and dynamic images of the same sections can be obtained. If an x-ray tube with sufficient heat-loading capabilities is used, and the duration of the acquisition of each series is reduced to less than five minutes, the dynamic experiments can be repeated at a number of different mean pressures. As discussed in chapter six, the major problem with a prolonged acquisition period is the diffusion of contrast agent into the arterial wall. This problem can be minimized if the osmolality of the fluid being pumped is matched to that of blood so that diffusion of contrast agent into the wall does not occur or occurs at a very slow rate. One other possibility is to use Freon 113 ($CClF_2$-CCl_2F) as the working fluid, since it has an attenuation coefficient which is nearly the same as that of 40 mg ml^{-1} iodinated solution (CT number = 1600 HU, at 90 kVp, with 3-mm added Al filtration). Chu, in our laboratory, has used this fluid while performing mechanical testing of arterial specimens using magnetic resonance imaging[1] and has observed no diffusion of the Freon into the arterial wall. By comparing the mechanical properties of fresh strips of porcine aortas to those of aortas soaked in Freon 113, he has shown that the fluid does not affect the elasticity, though it dissolved some of the fat component of the wall. Although this work is preliminary, and further validation of these results is necessary, the use of Freon 113 offers a unique opportunity to solve the problem of diffusion of contrast agent into the vessel wall.

Following the dynamic measurements, the vessel should be fixed in formaldehyde at physiological pressure, while mounted in the same configuration as for the elasticity experiments. The pressure-fixed vessel can then be imaged using the volume CT scanner to characterize the 3-D geometry. Histological analysis, as described in chapter four, should then be performed on the slices for which the mechanical properties were measured.

The present techniques have been developed to study straight arterial segments. Since atherosclerotic lesions are frequently found in the vicinity of bifurcations, the techniques must be modified to study these locations. One possibility is to use finite-element modelling to estimate the circumferential stresses in the area of the bifurcation, given the 3-D geometry of the vessel, at a few static pressures, and the transmural pressure. These stresses can then be used along with the measured strains to characterize the mechanical properties at bifurcations.

7.2.3 Velocity and shear rate measurements

In chapter six I described a technique for imaging pulsating arterial specimens using the laboratory dynamic CT scanner. Another application of the scanner is the visualization and measurement of velocity in excised vessels, using gated injections of iodinated contrast agent. The method I propose for quantifying the flow profile in a vascular phantom or an excised vessel involves the principles of both digital angiography and computed tomography. The vessel is to be mounted on the rotating stage, as described in chapter three. Fluid, of the appropriate viscosity, can be pumped through the vessel using the flow simulator described in chapter five. The flow can be steady or pulsatile, provided that when pulsatile flow is used, the image acquisition is gated to the flow cycle. A short bolus of iodinated contrast agent is injected, at least one inlet length above the observation site, using a power injector. An injection manifold, like the one shown in Fig. 7.2 should be used to distribute the

radio-opaque dye uniformly around the circumference of the vessel. The manifold allows the dye to enter the phantom through a series of 1-mm holes drilled through the wall of the connecting tubing, thus ensuring uniform tagging of the fluid. To be able to reconstruct the bolus in three dimensions (two spatial and one temporal dimension) time-evolved projections must be obtained at view angles around 180°. Since a separate bolus injection must be made for each view, the bolus injections must be highly reproducible. Also, the injector should be able to deliver a sharp bolus, to optimize the tagging of the fluid.[2] Preliminary studies of the flow profiles produced using a commercial injector indicate that a very short bolus cannot be injected. Figure 7.3 shows flowmeter results obtained using a commercial power injector set at the minimum injection time (0.2 s). We have developed a pulsed injector in our laboratory[3] which produces highly reproducible, sharp bolus injections. A sample flow waveform from this injector is also shown in Fig. 7.3. These sharp bolus injections would be ideal for flow tagging in this application.

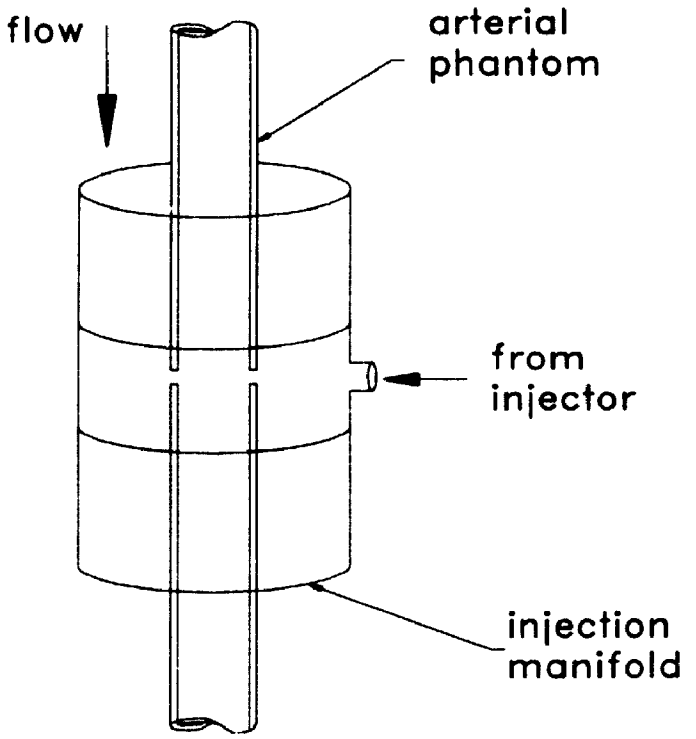

Figure 7.2: Schematic diagram of the injection manifold. Contrast agent from the injector is distributed around the inlet tube and enters the tube through 1-mm holes.

A preliminary experiment was performed, using a straight-tube phantom, to demonstrate the feasibility of this technique.[4] The transition of the radio-opaque bolus (injected using a commercial power injector) was recorded as it passed the

observation site. Time-evolved projection radiographs, like the one presented in Fig. 7.4, show a transmission profile through the bolus in the plane of interest as a function of time. The vertical axis corresponds to time, increasing in the downward direction, and the horizontal axis is parallel to the cross-section of the phantom. For this preliminary study, only 24 time-evolved projections were collected as the phantom was rotated through 180°. These were processed, as described in chapter three, to produce 'temporal cross-sections' through the bolus. The term temporal cross-section refers to the cross-section through the bolus which was in the plane of interest at a given time. A set of temporal cross-sections is shown in Fig. 7.5.

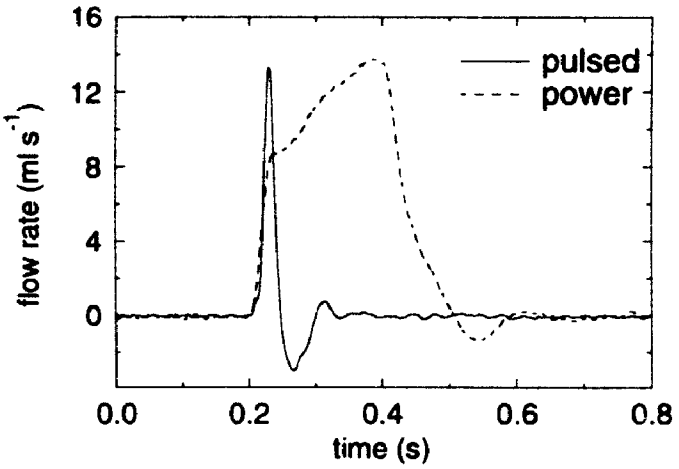

Figure 7.3: Sample flow waveforms produced by a commercial power injector and the pulsed injector developed in our laboratory.

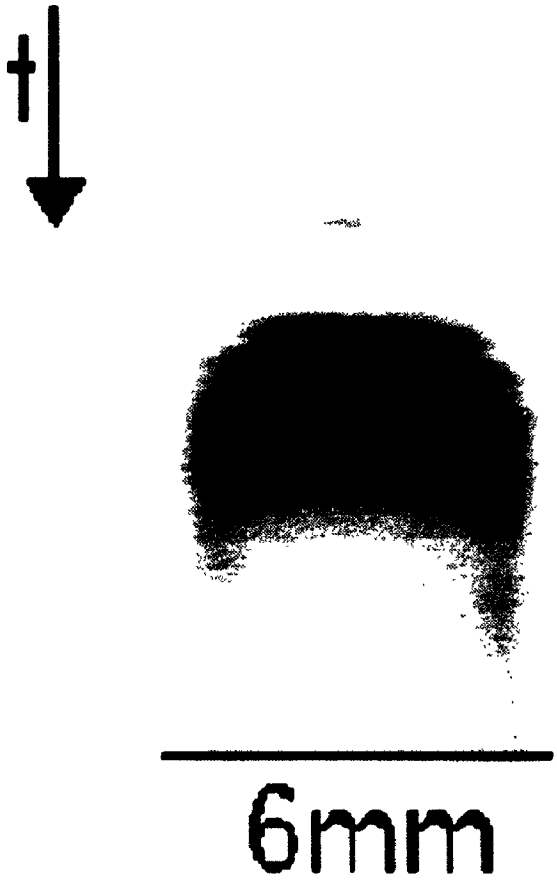

Figure 7.4: Time-evolved projection of a radio-opaque bolus flowing past the observation plane.

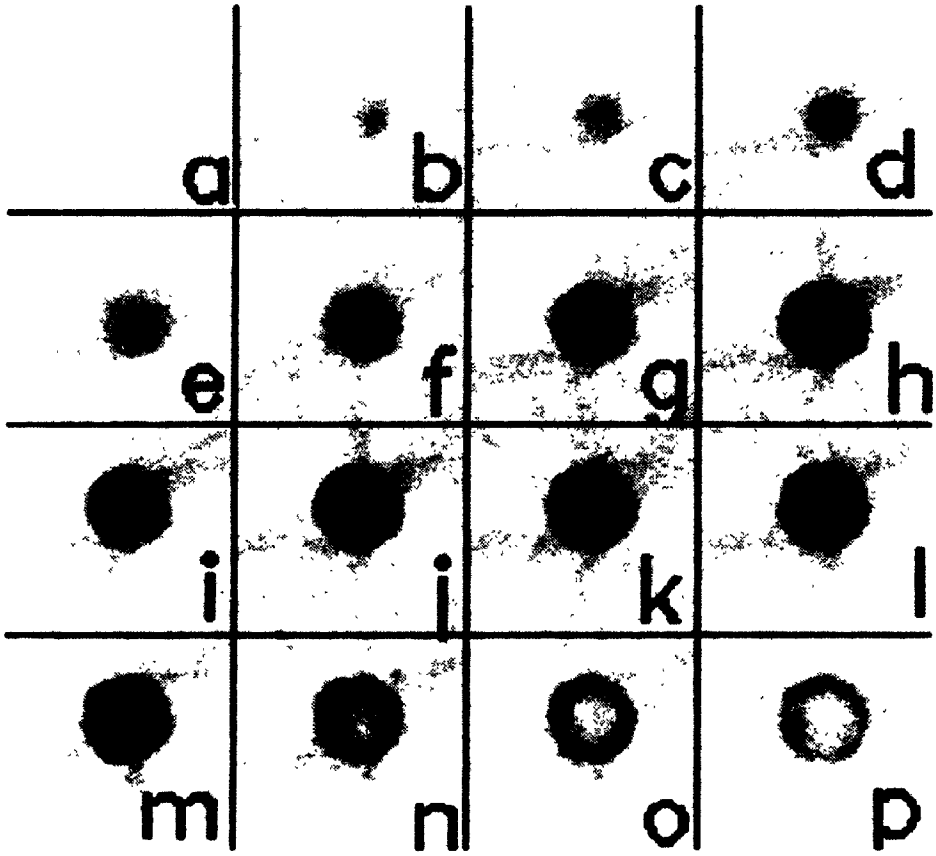

Figure 7.5: Temporal cross-sections obtained through a radio-opaque bolus which tagged water flowing at an average velocity of 30 cm s^{-1} in a 6 mm diameter tube. The temporal separation between images is 68 ms.

In order to obtain a quantitative measurement of the velocity, the bolus must be imaged at no fewer than two positions, so that the velocity can be calculated from the measured time of flight and the known distance between the two tomographic sections. This can be achieved by using the two mirrors described in section 7.2.1. Since this technique is based on the assumption that fluid flows in streamlines parallel to the long axis of the vessel, and that the velocity remains constant between the two observation sites, there is a tradeoff between the accuracy in the velocity measurement and the positional accuracy of the measurement. For high velocities, the collimators need to be far apart, so that the motion can be detected by the

scanner. If the velocity is slow, the collimators can be close to each other and, thus, the error due to the assumption that the flow is in the direction parallel to the vessel axis can be minimized. It is, thus, impractical to use this system in an attempt to measure the full velocity profile through a given section. However, the scanner can be optimized for measuring low velocities, such as those found near the wall.

The ability to measure the velocity near the vessel wall is important for the measurement of the shear stresses at the wall, since the shear stress depends on the rate of change of velocity with respect to radial distance at the inner boundary of the wall. The effects of shear stress on the initiation or progression of atherosclerosis are not fully understood, though it is generally believed that haemodynamic factors affect the endothelium, and may be linked to plaque formation. Many studies have been performed in the past in an attempt to link shear rate to arterial disease. Milnor[5] and Lou *et al.*[6] provide brief summaries of some of the work done in this area. The general problem with measuring the shear rate is that the velocity must be measured at the wall, and thus very high resolution is required. The dynamic CT scanner described here could be used to measure velocity near the wall with a resolution of 3.2 mm^{-1}. The technique could, therefore, supply *in vitro* measurements of the shear rate in diseased and disease-free vessels, adding further insight into the effects of shear stress on plaque formation.

7.2.4 Application of principles to dynamic clinical imaging

Although the dynamic CT scanner described in this thesis was designed for laboratory use, the principles introduced in chapter three could also be applied clinically for dynamic applications, such as cardiac imaging. Third or fourth generation scanners could be adapted to pause at each view angle and acquire a gated time-evolved projection of the slice of interest. However, this would be

cumbersome, since modifications to the scanner gantry would be necessary, and the time required to obtain a sufficient number of views could be prohibitively long.

An alternative option is to use a "helical CT scanner" to acquire the data. Helical scanning systems were introduced in the late 1980's for the rapid acquisition of 3-D CT images *in vivo*.[7] They use a continuously rotating gantry and slide the patient table past the x-ray fan beam as projection data are continuously acquired. Interpolation algorithms are then used to "rebin" the projection data into a set of sinograms corresponding to contiguous slices. From these, a volume image is reconstructed. The high quality images obtained with these new scanners have demonstrated that interpolation, even between slices, can be used to provide clinically useful images.[8]

I propose that a helical CT scanner could also be used to acquire dynamic images. Since the gantries of these scanners rotate continuously, they can be used to acquire projection data of a single slice over many cardiac cycles. If the ECG trace of the patient is monitored during the projection data acquisition, the data can be post-processed to yield a set of sinograms corresponding to different phases of the cardiac cycle. The post-processing would involve reformatting of the data so that at each view angle, a time-evolved projection is obtained. This technique would not provide a projection at each view angle for each phase of the cycle and, thus, interpolation between time-points would be necessary. This interpolation procedure would lead to a temporal blurring in the images, similar to that observed in retrospectively-gated magnetic resonance images of moving objects.[9]

This technique would not require any mechanical modification to a helical CT scanner. Provision must only be made to monitor the ECG and not move the patient couch during projection data acquisition. Finally, optimization of this technique, as well as assessing its the feasibility to patient imaging, can easily be performed using

the laboratory CT scanner described in this thesis. Phantoms like copper wire mounted on a reciprocating stage (section 3.5.2) can be used to optimize the technique, while a preliminary feasibility assessment could be performed using the pulsatile-flow simulator along with anthropomorphic phantoms of the human vasculature.[10,11]

REFERENCES

1. K.C. Chu and B.K. Rutt, "An *in vitro* method of measuring local arterial elasticity under pulsatile motion," Proc. Soc. Mag. Res. Med. 829 (1992).[abs]

2. W.P.J. Holland, "Indicator dilution theory for convective dispersion in laminar flow through straight tubes," Phys. Med. Biol. **27** 639-664 (1982).

3. D.W. Holdsworth, M. Drangova, and A. Fenster, "Quantitative angiographic volume blood-flow measurements using high-frequency pulsed injection," Med. Phys. **19**, 787 (1992).

4. M. Drangova, D.W. Holdsworth, and A. Fenster, "Table-top CT system for 3-D *in vitro* analysis of arterial flow and distensibility," Proc. SPIE **1231**, 255-260 (1990).

5. W.R. Milnor, *Hemodynamics* Williams and Wilkins, Baltimore (1989).

6. Z. Lou, W.J. Yang, and P.D. Stein, "Errors in the estimation of arterial wall shear rates that result from curve fitting of velocity profiles," J. Biomechanics **26**, 383-390 (1993).

7. C.R. Crawford and K.F. King, "Computed tomography scanning with simultaneous patient translation," Med. Phys. **17**, 967-982 (1990).

8. M.P. Marks, S. Napel, J.E. Jordan, and D.R. Enzmann, "Diagnosis of carotid artery disease: preliminary experience with maximum-intensity-projection spiral CT angiography," AJR **160**, 1267-1272 (1993).

9. R. Frayne and B.K. Rutt, "Frequency response of retrospectively-gated phase contrast MR imaging: effect of interpolation," JMRI (1993). [in press]

10. R.F. Frayne, L.M. Gowman, D.W. Rickey, D.W. Holdsworth, P.A. Picot, M. Drangova, K.C. Chu, C.B. Caldwell, A. Fenster, and B.K. Rutt, "A geometrically accurate vascular phantom for comparative studies of x-ray, ultrasound and magnetic resonance vascular imaging: construction and geometrical verification," Med. Phys. **20**, 415-425 (1993).

11. D.W. Holdsworth, B.K. Rutt, and R.N. Rankin, "Quantitative geometrical analysis of stenosed carotid bifurcations," Radiology **185**, 160 (1992).[abs]